Eidgenössische Technische Hochschule Zürich
Swiss Federal Institute of Technology Zurich

Master's Thesis

Towards cavity QED experiments with Rydberg atoms coupled to a 3D microwave cavity

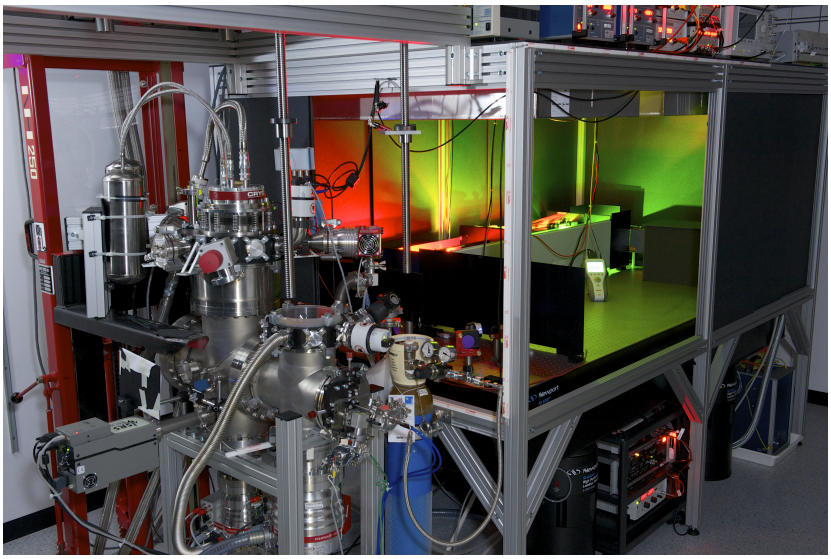

Silvia Ruffieux

Supervisor: Mathias Stammeier
Principal Investigator: Prof. Dr. Andreas Wallraff

Department of Physics
Laboratory of Solid State Physics
Quantum Device Lab

Zürich, October 2014

Abstract

The objective of cavity quantum electrodynamics (cavity QED) is to study the interaction between a spin-$\frac{1}{2}$ particle and a quantum harmonic oscillator. In this thesis such a system is implemented with Rydberg atoms passing through a 3D microwave cavity. The thesis is part of the Rydberg project that aims to combine Rydberg atoms with superconducting circuits in a hybrid system. The interaction between the atoms and the superconducting qubits will be mediated by photons at microwave frequencies. Ultimately, this would allow to store quantum information processed with superconducting qubits in long-lived atomic Rydberg states.
In a first set of experiments we study the interaction of Rydberg atoms with the electric fields inside the cavity. We develop a method to characterize the spatial distribution of the electric field in a particular mode by observing Rydberg atoms undergoing Rabi oscillations. By applying a potential difference between two electrodes inside the cavity, we can shift the transition frequency of the Rydberg atoms via the quadratic Stark effect with the created DC electric field. From the measurements we can then reconstruct the electric field profile of the electrodes along the beam axis for any given potential.
Up to this point we have studied the electric field inside the cavity by observing the population of the Rydberg states. We then aim at doing the reverse: measuring the state of the Rydberg atoms with the cavity - for example in a dispersive shift experiment. To this end we design a new cavity with a constant electric field over a long plateau and low inhomogeneity.
Furthermore, we need to characterize the amplification system necessary to observe a dispersive shift. We measure the gain and the noise temperature of the amplifiers at room temperature and in a dip stick measurement at liquid helium temperature.

Contents

1. Introduction

The development of quantum mechanics in the last century revolutionized physics and strongly affected how we perceive the world around us. Quantum mechanics defines a set of rules for the construction of physical theories [1]. These rules are simple, but some of the predictions made using quantum mechanics (e.g. entanglement, EPR paradox) are counter-intuitive - which is why even leading scientists like Albert Einstein rejected the theory. Nonetheless, no experiment has so far been found that strictly violates quantum mechanics and no other consistent theory has been developed that manages to predict comparably accurate results. Quantum mechanics correctly describes the physics on the microscopic, the mesoscopic and the macroscopic length scales: it can explain the structure of the atom, the DNA, superconductors and nuclear fusion in stars. The successful application of quantum mechanics to many different fields made it indispensable to many branches of physics [1].

Quantum mechanics did not only change our view of the world, it also led to the invention of many new devices like the laser [2], the electron microscope and the atomic clock [3]. One of the most important inventions in the last century was the transistor. Its application in integrated circuits made it possible to store and process information efficiently. Computers are nowadays ubiquitous in our daily life and our demand for computational power remains unbroken. In 1965 Gordon Moore predicted the growth in computer power in what has come to be known as *Moore's Law* [4]: computer power will double for constant cost roughly once every two years. His prediction has been valid since more than 40 years. But as the electronic circuits are made smaller and smaller (soon reaching the size of atoms), quantum effects begin to interfere in the functioning of the devices and disturb further improvement.
More important, for some problems no efficient[1] algorithm running on a classical computer has been found, meaning that even with a fast computer the problem could not be solved in a sensible amount of time. In 1982, for example, Richard. P. Feynman realized that it is not possible to efficiently simulate arbitrary quantum mechanical systems using classical computers [5]. How can these limitations be overcome?

Quantum Computation

One approach is to move to a new computing paradigm as the theory of quantum computation suggests. The key idea is to build a computer based on quantum phenomena (i.e.

[1] The notion *efficient* in the field of computational complexity refers to algorithms running in time polynomial in the size of the problem solved, whereas *inefficient* algorithms require superpolynomial (typically exponential) time.

a quantum computer). This computer can for example be used to perform simulations of quantum mechanical systems, which would revolutionize atomic physics, material physics and biochemistry.
In 1985 David Deutsch presented the concept of an Universal Quantum Computer [6]. He searched for a device that could efficiently simulate an arbitrary physical system and constructed a first algorithm that was more efficient than the associated classical one. The algorithm determines whether a given boolean function with 1 input bit (f: $\{0,1\} \rightarrow \{0,1\}$) is constant. In his example he exploited the superposition principle: in contrast to a classical bit, a quantum bit (qubit) can not only be in the zero or the one state but in both simultaneously. Together with Richard Jozsa he later made a multidimensional version of his algorithm, which got known as the Deutsch-Jozsa algorithm [7].
Further evidence that quantum computers are more powerful than classical ones was given in 1994 by Peter Shor and in 1995 by Lov Grover, who both found an algorithm solving an important problem. Grover's algorithm leads to a quadratic speed up (compared to the classical algorithm) for the problem of searching an element in an unstructured database [8]. Peter Shor found an algorithm on a quantum computer that was able to calculate prime factors of an integer efficiently [9]. The algorithm has attracted widespread interest until today, because the security protocols of public key cryptography like RSA are based on the difficulty of factorizing larger numbers [10], meaning that a quantum computer could successfully attack an RSA system. Fortunately, there are also quantum cryptography protocols that allow secure communication over public quantum channels [11].

Building a quantum computer

So how do we build quantum computers? For the successful physical implementation David P. DiVincenzo defined 7 criteria [12]:

1. Qubits: A scalable physical system with well characterized qubits
2. Initialization: The ability to initialize the state of the qubits
3. Coherence: Long relevant decoherence times, much longer than the gate operation time
4. Gates: A universal set of quantum gates
5. Read-out: A qubit-specific measurement capability
6. Conversion: The ability to interconvert stationary and flying qubits
7. Transmission: The ability to faithfully transmit flying qubits between specified locations

Several promising candidates that could serve as qubits have been suggested and investigated during the last decades: photons [13], trapped ions and cold atoms [14], superconducting circuits [15], quantum dots [16], nuclear magnetic resonance (NMR) [17] and nitrogen-vacancy (NV) centers [18]. Scientists succeeded in implementing Shor's algorithm factoring the number

15 on an NMR system [19] as well as the Deutsch-Josza algorithm on a trapped ion system [20].

Two main challenges arise when trying to build a quantum computer. The first is the trade-off between coherence and intractability. A system must be coherent, meaning that the qubit does not decay or dephase before the measurement is done. As decoherence occurs due to uncontrolled interactions with the environment (e.g. noise), the system must be isolated from the environment. On the other hand, the application of gates and the read-out require an interaction of parts of the environment with the system.
The second challenge is to scale the system up to more than just a few qubits. For the factorization of a 200 digit number, a machine capable of storing 3300 qubits would be needed [21]. The record so far is to entangle 14 qubits in a trapped ion system [22]. The main problem is to distribute the entanglement over a large distance and number of qubits before decoherence occurs.

Hybrid Systems

The systems mentioned above all have their weaknesses and advantages. The idea of *Hybrid Systems* is to combine two different kinds of quantum systems in one experimental setup and use the advantages of each system. Certain states and transitions in ions and atoms, for example, can have long coherence times due to efficient isolation from the environment. On the other hand, they only weakly interact with control fields, meaning that the effective time scales over which they can be manipulated is limited. The reversed situation is achieved in most solid state systems (e.g. superconducting qubits). There the quantum system interacts strongly with its environment and thus its control field, which allows a fast manipulation of the qubits, but the coherence times are reduced. These properties make it interesting to merge the two systems. The computation can be done in the solid state system, while the ions or atoms act as quantum memories. Several proposals how to combine these two systems have been made [23, 24].

The goal of the *Rydberg Project* in the Quantum Device Lab at ETH Zürich is to develop such a hybrid system. Rydberg atoms are used due to their large dipole moment and long lifetimes of up to several tens of milliseconds [25]. Superconducting qubits have short gate times in the order of tens of nanoseconds and lifetimes up to 100 μs [26]. Both superconducting artificial atoms and Rydberg atoms interact with radiation fields and the interaction between the two systems will therefore be mediated by microwave photons stored in resonators.
The first focus of the project is to investigate the interaction and manipulation of Rydberg atoms with a classical microwave field. So far Rydberg-Rydberg transitions, Rabi oscillations and stray fields in the vicinity of a solid-state coplanar waveguide were observed [27]. A method was developed to measure, minimize and compensate the stray fields, which makes the preservation of the coherence for several microseconds possible [28].
Two types of resonators are basically used. The first is a two dimensional resonator on a chip. This geometry exhibits strong electric fields, which however decay exponentially with distance

from the chip, meaning that the distance between the atom beam and the chip has to be smaller than 500 μm [28] to reach the strong coupling regime. In the vicinity of the chip, stray electric fields detune the Rydberg atoms, which is a problem. The second type of resonator is a three dimensional rectangular cavity, in which the the AC electric field magnitude is generally smaller due to the reduced mode volume. On the other hand, the field is homogeneous over the size of the atomic beam, meaning that the atoms can interact with the electric field without approaching the cavity walls by more than a few millimeters and stray fields are thus less a problem.

This thesis

In my thesis I work on the project with the 3 dimensional cavity. At the starting point of my thesis, the cavity is well understood and characterized, but no experiments involving Rydberg atoms have yet been conducted. The aim is to realize typical cavity QED experiments. We start with experiments studying Rabi oscillations, which result from the interaction between a classically driven field inside the microwave cavity and the Rydberg atoms. The first measurements show that the alignment is essential - else wise the atomic beam does not properly go through the holes inside the cavity and we observe strong stray fields. From the observance of Rabi oscillations we draw conclusions on the strength of the oscillating electric field inside the cavity and measure cavity properties such as the modefunction. The stray fields can be estimated by measuring the Stark shift of the atomic transition frequency. In a second experiment we introduce two round electrodes parallel to the atomic beam inside the cavity. By applying voltages to the electrodes, we can manipulate the detuning thanks to the Stark shift.
In the first part of the thesis we study the electric fields inside the cavity by observing the MCP signal from the Rydberg atoms. In the second part we aim at measuring a dispersive shift in the cavity resonance frequency, which allows to extract the state of the Rydberg atoms. In order to be able to measure a dispersive shift, we need a new cavity and a measurement system with a high signal to noise ratio. We therefore perform FEM simulations to find an optimal cavity geometry and characterize the amplification system. The signal to noise ratio mostly depends on the gain and the noise temperature of the first amplifiers, which we measure with a network analyzer and the Y-Method, respectively.

The structure of this thesis is the following: in chapter 2 the most important theoretical aspects concerning Rydberg atoms, 3D microwave cavities, cavity quantum electrodynamics and noise in amplifiers will be summarized. Chapter 3 describes the experimental setup and measurement procedure for the Rydberg atom measurements. In chapter 4 these measurements are detailed and the results presented. After the measurements a new cavity is designed for which the static electric field distribution is optimized (chapter 5). We then switch to the amplification system in chapter 6 and describe our down conversion board, the gain and the noise temperature measurements. The thesis ends with a conclusion and an outlook (chapter 7).

2. Theory

2.1. Rydberg atoms

Rydberg atoms have one or multiple electrons in highly excited states (principle quantum number n), which gives them exaggerated properties such as big radii, long lifetimes, a high number of adjacent energy levels and an exaggerated response to electric and magnetic fields. The simplest Rydberg atom is the hydrogen atom, which can be described analytically. Since the core electrons shield the highly excited outer electron from the electric field of the nucleus, non-hydrogen Rydberg atoms show hydrogen-like behavior and can thus be described in a similar way.

In this chapter we will give a short introduction to the physics of Rydberg atoms. We will follow the outline in Gallagher's book on Rydberg atoms [29] and start with the discovery of Rydberg atoms in section 2.1.1. We will then continue with the theoretical description (section 2.1.2) by reviewing Bohr's model, which gives the correct n-scaling of most properties like the radius, the energy level spacing and the dipole moment. A more thorough description is then given by quantum defect theory. In section 2.1.3 we move on to an important property, the lifetime. In the last section (2.1.4) we will summarize the interaction of the Rydberg atoms with an electric field. Perturbation theory leads us to the linear and the quadratic DC-Stark effect depending on the degeneracy of the energy levels.

2.1.1. Historical background

In the early 19th century several scientists like Frauenhofer, Kirchhoff and Bunsen studied emission and absorption spectra. They found that each chemical element had its own unique spectral pattern - like an optical fingerprint. The Balmer series, for instance, is a sequence of spectral lines in the emission spectrum of the hydrogen atom. In this series Rydberg atoms appeared for the first time and have since then played a role in atomic physics and spectroscopy. The hydrogen atom was the first atom to be understood quantitatively. In 1885, Johann Balmer described the wavelength λ of the visible series of atomic H with the formula [29]

$$\lambda = \frac{bn^2}{n^2 - 4}, \tag{2.1}$$

where b = 3645.6 Å and n is a natural number greater than 2. One crucial step towards understanding the formula was made by Harley, who was the first to realize the significance of the frequency f (or the wavenumber ν, with $f = c \cdot \nu$, where c is the speed of light) in

contrast to the wavelength. Using the wavenumber, we can rewrite Balmer's formula and later recognize it as describing transitions from a higher energy level n to the second level

$$\nu = \frac{1}{\lambda} = \frac{4}{b}\left(\frac{1}{2^2} - \frac{1}{n^2}\right) \tag{2.2}$$

The hydrogen atom was not the only atom leading to new insights. Liveing and Dewar observed the spectral lines of Na and found out that they could be grouped into different series. They were looking at the transitions between the levels ns and 3p or nd and 3p emitted from an arc. The ns-3p doublets gave sharp lines, while the nd-3p doublets were diffuse. Hence also the names s for *sharp*, d for *diffuse* and p for *principle*. Nowadays we know that the d states are almost degenerate with higher angular momentum states for the same n state and can therefore understand that the lines are diffuse. At that time the most important observation was that the sharp and diffuse doublets were members of two related series.
Johannes Rydberg continued the work of Liveing and Dewar and classified the spectra of other atoms into sharp, principal and diffuse series with one common lower level. He found an expression for the wavenumbers ν of each series l = s, p or d

$$\nu = \nu_{\infty,l} - \frac{R_\infty}{(n-\delta_l)^2}, \tag{2.3}$$

where $\nu_{\infty,l}$ is the series limit and δ_l the quantum defect, which is 0 for the hydrogen atom. The constant $R_\infty = 10.97\mu m^{-1}$ is known as the Rydberg constant. It is an universal constant describing the wavenumbers of the transitions independent of the series or the atom type.
By studying the series limits, Rydberg made a major accomplishment: he could find a general expression for the wavenumbers of lines connecting different series. For the hydrogen atom, the wavenumber of the transition from the initial state n to the final state n' can be calculated with

$$\nu = R_\infty \cdot \left(\frac{1}{n'^2} - \frac{1}{n^2}\right). \tag{2.4}$$

Balmer's formula (2.2) can be retrieved by choosing n'=2 and noticing that $R_\infty = \frac{4}{b}$. Rydberg's formula (2.4) gave excellent predictions and was confirmed in different series for the hydrogen atom: Lyman (n=1), Balmer (n=2), Paschen (n=3) Brackett (n=4) and Pfund (n=5). Using the quantum defects δ_l, other atoms could also be described. At that time n was just a natural number.

2.1.2. Theoretical description

The physical significance of n became clear when Niels Bohr proposed his model of the hydrogen atom in 1913. The Bohr model is important for Rydberg atoms as it manages to describe many properties of Rydberg atoms by giving the correct scaling laws. We will therefore first look at Bohr's model and derive the scaling laws for the radius, the energy levels and the difference between the energy levels. As the Bohr model oversimplifies the problem, especially

for non-hydrogen atoms, we will continue with a more thorough approach: quantum defect theory, which takes the finite extents of the core into account.

Bohr model

The Bohr model describes an electron moving around a proton in a circular orbit of radius r. The electron has a mass m and a charge -e, while the proton has a positive charge e. Other Rydberg atoms can also be represented by replacing the proton with an ionic core of charge Ze. The excited Rydberg atom sees the ionic core and the electron cloud as having a net charge e like for the proton.
Bohr added two new notions to the classical description. First, the electron does not radiate continuously in a classical manner but only emits radiation in transitions between different orbits. Second, the angular momentum of the electron is quantized: $l = mrv = n \cdot \hbar$. Using these two assumptions, the radius r , the energy E of an orbital and the transition frequencies f can be calculated. The radius of the atom in state n is obtained by setting the centripetal force equal to the Coulomb force, which leads to

$$r = \frac{4\pi\epsilon_0\hbar^2}{e^2 m} n^2 = a_0 \cdot n^2, \tag{2.5}$$

meaning that the radius scales quadratically with the principle quantum number n. The ground state hydrogen atom has a radius a_0 of 0.53 Å, while a Rydberg atom with n = 10 is already 100 times bigger.
The energy E of a hydrogen atom in state n can be found by adding the kinetic and the potential energy and inserting the expression obtained for the radius:

$$E = \frac{mv^2}{2} - \frac{1}{4\pi\epsilon_0}\frac{e^2}{r} = \frac{-1}{(4\pi\epsilon_0)^2}\frac{e^4 m}{2n^2\hbar^2} \propto n^{-2}. \tag{2.6}$$

The energies are negative, meaning that the electron is bound to the proton. The binding energy decreases as $1/n^2$. The differences between the energy levels represent the allowed transition frequencies:

$$hf = E_2 - E_1 = \underbrace{\frac{1}{(4\pi\epsilon_0)^2}\frac{e^4 m}{2\hbar^2}}_{R_y}\left(\frac{1}{n_1^2} - \frac{1}{n_2^2}\right), \tag{2.7}$$

where $R_y = hcR_\infty = 13.6$ eV is the Rydberg energy. Using Bohr's model we can relate the Rydberg constant to the properties of the atom.
For non-hydrogen atoms the quantum number n has to be replaced by the effective quantum number n^*, which will be discussed in more detail in quantum defect theory. The scaling laws are the same for hydrogen and hydrogen-like atoms. The most important scaling laws for Rydberg atoms are summarized in Table 2.1.
Two assumptions were made that oversimplify the problem. First, the electron moves around

the core in a circular orbit. Second, the core has infinite mass. Nonetheless the model manages to predict the correct scaling laws. In order to obtain further properties of Rydberg atoms, especially for non-hydrogen atoms, we will apply quantum defect theory and derive the wave function of a Rydberg atom using Schrödinger's equation. In this way we are not restricted to circular motion and can take the extend of the core into account.

Property	n^* dependance
Binding energy	$(n^*)^{-2}$
Energy between adjacent n states	$(n^*)^{-3}$
Orbital radius	$(n^*)^2$
Cross section	$(n^*)^4$
Dipole moment	$(n^*)^2$
Radiative lifetime	$(n^*)^3$ to $(n^*)^5$

Table 2.1.: *Scaling laws for Rydberg atoms [29]*

Quantum defect theory

Quantum defect theory allows us to accurately calculate many properties of single valence electron Rydberg atoms. One special case is the H atom, as its wave functions are well known and give analytic solution to a large number of problems. Quantum defect theory can be easily understood by starting with the hydrogen atom and then modifying the result to obtain a description for non-hydrogen Rydberg atoms with one valence electron. In the step from the hydrogen atom to the hydrogen-like atom, the extend of the core is taken into account defining the quantum defect. How this is done in detail will be explained when the necessary terms are introduced for the hydrogen atom.

Hydrogen atom

We will start with the time independent Schrödinger equation in atomic units, which are chosen such that all relevant parameters are in units corresponding to the hydrogen ground state. The unit of length is for example given by Bohr's radius a_0. The Schrödinger equation for the wave function $\Psi(r, \theta, \phi)$ of the electron in a hydrogen atom is given by [29]

$$\left(-\frac{\nabla^2}{2} - \frac{1}{r}\right) \Psi(r, \theta, \phi) = E\Psi(r, \theta, \phi), \tag{2.8}$$

where E is the energy and r the distance between the electron and the proton. Due to the symmetry of the problem, spherical coordinates are chosen, where θ is the polar and ϕ the azimuthal angle of the electron's position. Equation (2.8) can be separated into a product of radial and angular functions:

$$\Psi(r, \theta, \phi) = |nlm\rangle = R(r)\, Y_{lm}(\theta, \phi), \tag{2.9}$$

where $Y_{lm}(\theta, \phi)$ is the normalized spherical harmonic for the orbital angular momentum quantum number l and the magnetic quantum number m. A more detailed derivation and a description of the spherical harmonics can be found in Gallagher's book on Rydberg atoms [29] or in the textbook "Quantum mechanics of one- and two- electron atoms" [30]. Here we will focus on the most important steps and results.
The radial function $R(r)$ solves the radial equation and has the two physically interesting solutions

$$R_1(r) = \frac{f(l, E, r)}{r} \quad \text{and} \quad R_2(r) = \frac{g(l, E, r)}{r}. \tag{2.10}$$

The functions f and g are the regular and irregular Coulomb function. For E $>$ 0 and large radius r, they are simply sine and cosine waves. For E $<$ 0 we get bound solutions. Since the wave function has to be square integrable, we have to take a closer look at the limits $r \to 0$ and $r \to \infty$. For radii r close to 0, the functions have the forms

$$f(l, E, r) \propto r^{l+1} \tag{2.11a}$$

$$g(l, E, r) \propto r^{-l}, \tag{2.11b}$$

meaning that only the regular Coulomb function f is allowed. From the $r \to \infty$ boundary condition and further knowledge about the behavior of the regular Coulomb function at large radius, we can retrieve the formula for the energies of the hydrogen atom (2.6) in atomic units:

$$E = \frac{1}{2n^2}. \tag{2.12}$$

The wave function still has to be normalized. This results in a normalization constant that decreases as $1/n^{3/2}$ [29]. For small r, the wave function only depends on energy through the normalization constant. The wavefunction can now be used to calculate expectation values and find scaling properties of Rydberg atoms. The most important scaling properties are summarized in Table 2.1.

Hydrogen-like atoms

The treatment of the hydrogen atom with Coulomb waves (instead of the more common Hermite polynomial solution for the radial function) enables us to easily extend the solution from the hydrogen atom to other single valence electron atoms. This is done in quantum defect theory and allows to generate wave functions that are accurate in the case that the Rydberg electron is outside the ionic core.
The main difference between the hydrogen atom and non-hydrogen Rydberg atoms is the extent of the core the Rydberg atom orbits. For the proton we usually assume a point charge, whereas for the ionic core we have to take it's finite size into account. Far from the core, the potential experienced by the Rydberg atom is the same as the one due to a proton and it only sees a net charge of e. However, when the Rydberg atom gets close to the ionic core, the precise (and unknown) charge distribution of the other electrons starts to play a role. The

Rydberg electron penetrates the electron cloud and is exposed to the unshielded charge of the nucleus, which increases it's binding energy due to Coulomb interaction. This in turn decreases the total energy, which is additionally lowered due to core polarization. We will assume that the potential of the core is spherically symmetric and frozen in place. The resulting effective potential with the contribution from the core (V_{Core}) is deeper than the Coulomb potential $-1/r$ alone (see Figure 2.1).

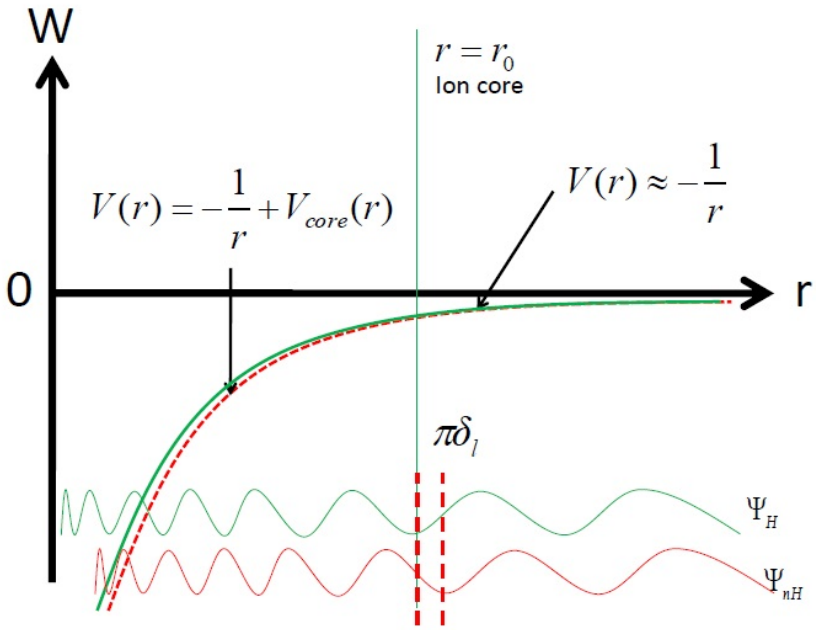

Figure 2.1.: *Illustration of the quantum defect. Figure by Tobias Thiele.*

This change only affects the radial part $R(r)$ of the wave function for the Rydberg electron, the angular function stays the same. In a lower potential, the kinetic energy of the Rydberg electron is increased, which leads to a smaller wavelength of the radial oscillations relative to those obtained for the hydrogen atom. For r bigger than the radius of the ionic core r_0, the potentials for the hydrogen and the non-hydrogen atom are identical. Therefore the wave function is merely shifted by the radial phase shift τ. This phase shift leads to a different boundary condition as for the hydrogen atom: the wave function no longer needs to be finite at the origin but has to be shifted by τ compared to the hydrogenic wave function for radii larger than r_0. The pure regular Coulomb function f is replaced by

$$f(l, E, r) \longrightarrow f(l, E, r)\cos(\tau) - g(l, E, r)\sin(\tau). \tag{2.13}$$

The $r \to \infty$ boundary condition is also changed and $\pi n + \tau$ has to be an integer multiple of π. The effective quantum number $n^* = n - \tau/\pi$ differs from the integer n by the amount τ/π known as the quantum defect δ_l. The binding energies are given by

$$E = \frac{-1}{2(n - \delta_l)^2}. \tag{2.14}$$

The quantum defect δ_l is constant for a series of l states because τ is independent of the energy. For higher l states the Rydberg electron circles the ionic core and behaves more or less like the electron of the hydrogen atom resulting in very small quantum defects. For low l states the orbits are more elliptical and the electron comes close to the core. This leads to high quantum defects, which depresses the low l states in energy as can be seen in Figure 2.2 for sodium and hydrogen as a comparison. For the helium atom the quantum defects are 1.1397, 0.9879, 0.0021 and 0.0004 for s, p, d and f [27].

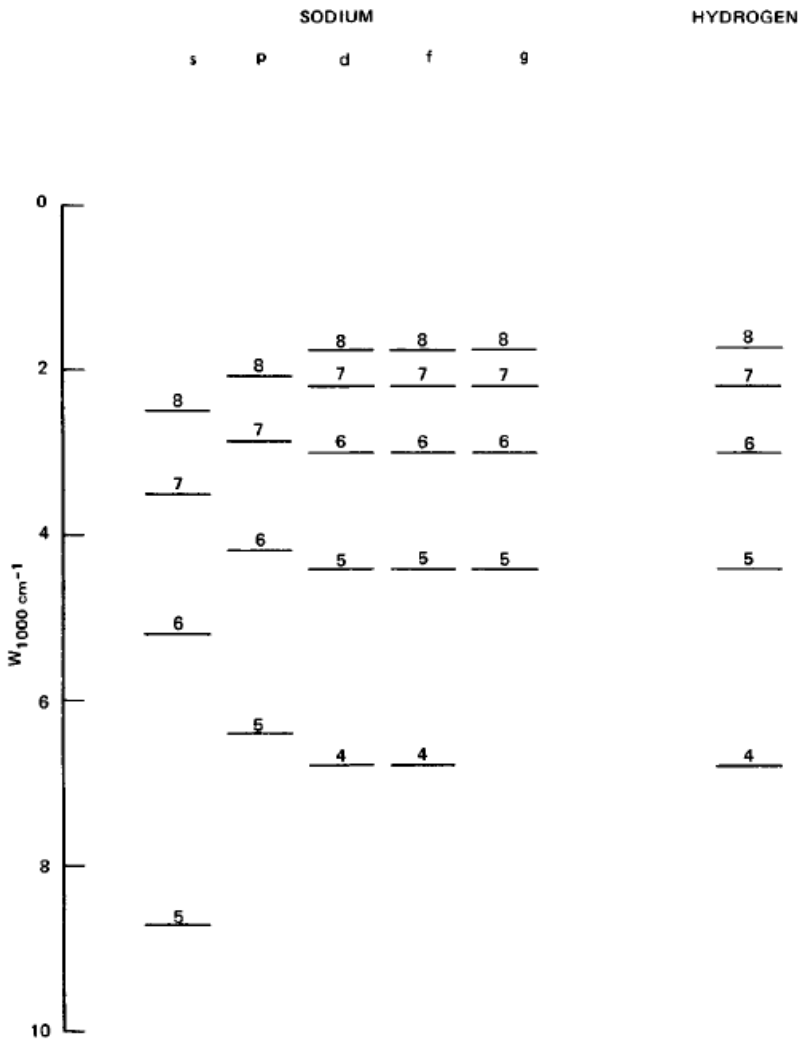

Figure 2.2.: *Comparision energy levels of Na and H. Figure from [29]*

2.1.3. Lifetime

In experiments it is essential that the lifetime of the relevant Rydberg atom states exceeds the duration of the experiment cycle. For atoms in free space, the decay to lower levels is due to spontaneous decay and black body radiation induced transitions. The two decay rates can simply be added. Since the lifetimes are given by the inverse of the decay rates, the resulting

lifetime τ_T at a temperature T is given by

$$\frac{1}{\tau_T} = \frac{1}{\tau} + \frac{1}{\tau_{bb}}, \tag{2.15}$$

where τ is the 0 K lifetime of a state (limited by spontaneous decay) and $\frac{1}{\tau_{bb}}$ the decay rate due to black body radiation. The two contributions will be calculated separately in the following subsections.

Spontaneous decay

Fermi's golden rule gives a general expression for the transition rate from one energy state nl to another state n'l'. The Einstein A coefficient describes the spontaneous transition rate and is given by [30]

$$A_{nl,n'l'} = \frac{4}{3}\mu^2_{nl,n'l'}\omega^3_{nl,n'l'}\frac{\alpha^3 g_>}{2g_n + 1}, \tag{2.16}$$

where α is the fine-structure constant, $\mu_{nl,n'l'}$ the electric dipole matrix element and $\omega_{nl,n'l'}$ the frequency of the nl $\rightarrow$ n'l' transition, g_n and g'_n are the degeneracies of the nl and the n'l' state, and $g_>$ is the greater of g_n and g'_n. The lifetime τ_{nl} of the nl state can now be obtained by summing the decay rates to all possible lower n'l' states:

$$\frac{1}{\tau_{nl}} = \sum_{n'l'} A_{nl,n'l'}. \tag{2.17}$$

The scaling of the decay rate in (2.16) with ω^3 implies that the decay into the lowest allowed state contributes most heavily to the total decay rate. For low-l Rydberg states with reasonably high n, the frequency of the decay is nearly independent of n as the lowest l' states are bound orders of magnitudes stronger than the Rydberg states. The only n dependence comes from the squared electric dipole moment $\mu^2_{nl,n'l'}$ that goes as n^{-3}, because of the normalization of the Rydberg wave function. Therefore the lifetime of the low-l states scales as

$$\tau_{nl} \propto A^{-1} \propto \mu^{-2} \propto n^3. \tag{2.18}$$

For high-l Rydberg states the n dependence is completely different. Due to selection rules the l = n-1 state for example can only decay to the n' = n-1 state with l = n-2 (the photon carries away one quantum of angular momentum). The frequency of a n $\rightarrow$ n-1 transition scales as n^{-3}. The overlap of the wave functions scales as n^2 like the orbital radius. This leads to a lifetime for the l = n-1 states that scales as

$$\tau_{n,n-1} \propto A^{-1} \propto \mu^{-2}\omega^{-3} \propto n^{-4} \cdot n^9 \propto n^5. \tag{2.19}$$

The average decay rate of all l and m states of the same n scales as $n^{4.5}$ [30]. In our case we have helium Rydberg atoms in the s or p state (l = 0 or 1). For these two states it is important to take the effective quantum number n^* instead of n and the scaling law for low l

states. The lifetime τ_n^p of the np series can be estimated with [28]

$$\tau_n^p = \tau_n^1 \cdot n^{*3} = \tau_n^p \cdot (n - \delta_p)^3 \,, \tag{2.20}$$

with $\tau_n^1 \cong 3.8 \cdot 10^{-11}$ s determined from the measured lifetime of 1.4 μs of the 34p state and the quantum defect $\tau_n^p = 0.9879$. The s state lives a lot longer: about 100 μs for the 34s state [28]. In the experiments done for this master's thesis, the n = 37 state is used. Calculations using the numbers above give a life time of about 1.8 μs for the 37p state and 130 μs for the 37s state.

Black body radiation

Up to now we have looked at the spontaneous decays driven by the vacuum. At room temperature (300 K) there are many thermal photons driving the n $\rightarrow$ n$\pm$1 transitions of Rydberg states with n$\geq$10. We will therefore have a closer look at transitions induced by black body radiation photons.
The transmission rate $K_{nl,n'l'}$ of a transition from the nl state to the n'l' state due to stimulated emission or absorption is only boosted by the number of thermal photons $\bar{n}$ compared to the spontaneous emission rate (2.16) and given by [31]

$$K_{nl,n'l'} = \frac{4}{3}\mu^2_{nl,n'l'}\omega^3_{nl,n'l'}\frac{\alpha^3 \bar{n} g_>}{2g_n + 1}. \tag{2.21}$$

The photon occupation number $\bar{n}$ is described by Bose-Einstein statistics:

$$\bar{n} = \frac{1}{\exp^{\hbar\omega/k_B T} - 1} \approx \frac{k_B T}{\hbar\omega} \propto n^3. \tag{2.22}$$

The photon occupation number of the black body radiation field is high at low frequencies and negligible at higher frequencies. Due to the small gap energy, black body induced transitions take place preferably between neighboring energy levels with high n. The total black body decay rate is also calculated by summing the decay rates over n' and l':

$$\frac{1}{\tau_{bb}} = \sum_{n'l'} K_{nl,n'l'}. \tag{2.23}$$

The decay rate due to black body radiation $\frac{1}{\tau_{bb}}$ differs from the spontaneous decay rate proportional to n^{-5} by the factor n^3 due to the photon occupation number and thus scales as n^{-2}. For high n the lifetime τ_T is hence dominated by the decay due to black body radiation, which is one reason why measurements at 4 K are done.

2.1.4. Interaction with electric fields

An external electric field alters the energy levels of an atom and splits its spectral lines. This effect is called the (DC) Stark effect and it is the electric analogon to the (magnetic) Zeeman

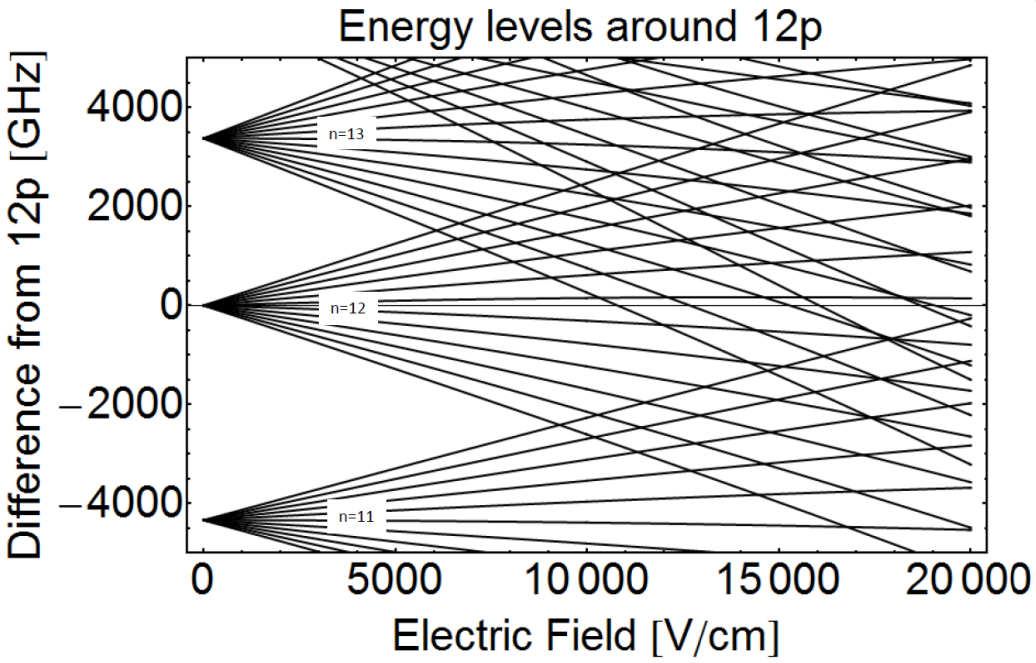

(a) *Stark map hydrogen.*

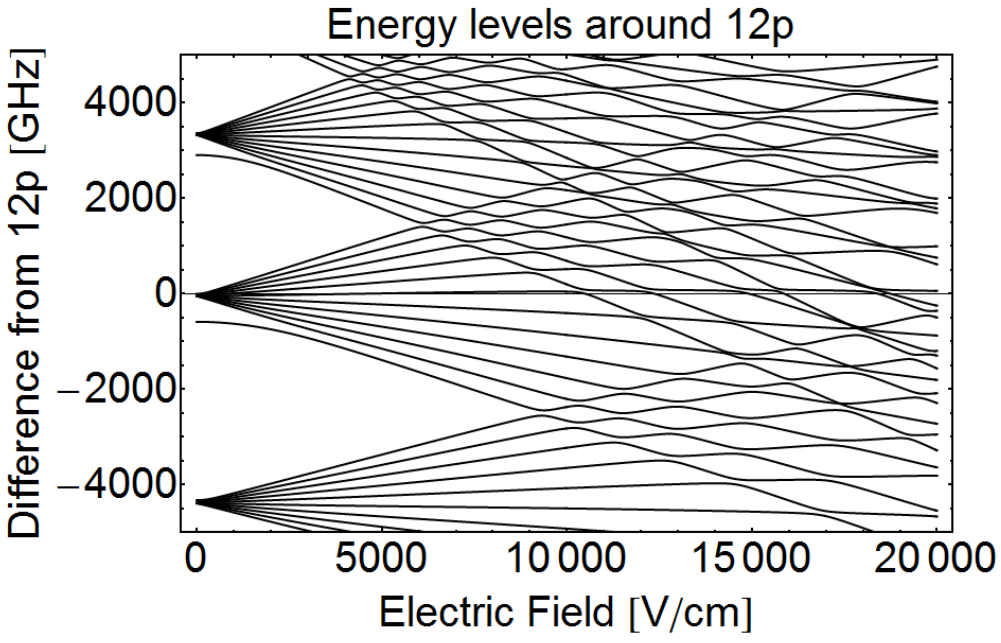

(b) *Stark map helium.*

Figure 2.3.: *Stark maps for hydrogen and helium around the 12p state. Figures by Tobias Thiele.*

effect. One distinguishes between first- and second-order Stark effects depending on the degeneracy of the energy levels. For hydrogen atoms and hydrogen-like atoms (such as He^+ and Li^+) with degenerate energy levels, the linear Stark effect leads to a shift of the energy levels proportional to the applied electric field [32]. The quadratic Stark effect is observed for all atoms with non-degenerate energy levels and denotes the quadratic dependence of the shift in the energy levels on the applied electric field. Both Stark effects can be obtained with perturbation theory.

Linear Stark effect for the hydrogen atom and Inglis-Teller limit

We will now examine the effect of a static electric field F in the z-direction on the energy levels of the hydrogen atom and later describe the effect on non-hydrogen atoms. The field is assumed to be small enough to be treated as a perturbation. We can describe this new system with the Hamiltonian

$$H = H_0 + Fz = H_0 + Fr\cos(\theta), \tag{2.24}$$

where H_0 is the zero field Hamiltonian of the hydrogen atom as introduced in equation (2.8). By using the zero field $|nlm\rangle$ states in spherical coordinates, we can calculate the matrix elements $\langle nlm| Fr\cos(\theta) |n'l'm'\rangle$ of the Stark perturbation, which couples states with the same energy. From the symmetry properties of the spherical harmonics the selection rules for the electric dipole coupling can be derived: the matrix elements are non-vanishing if m'=m and l'= l±1. The electric field therefore couples l and l±1 states with the same m and n and we get off diagonal perturbation matrix elements $F\langle nlm| r\cos(\theta) |n(l\pm1)m\rangle$ that are all linear in the electric field F. The eigenvalues are thus all proportional to F, while the eigenvectors are independent of F. The energies of the Stark states can be calculated using parabolic coordinates to diagonalize the perturbation matrix. The energies of the Stark states are in first order given by [29]

$$E = -\frac{1}{n^2} + \frac{3}{2}(n_1 - n_2)nF \tag{2.25}$$

where n_1 and n_2 are the parabolic quantum numbers satisfying

$$n_1 + n_2 + |m| + 1 = n. \tag{2.26}$$

The states with different $k = n_1 - n_2$ have different energies, which leads to a field dependent splitting of the spectral lines as displayed in Figure 2.3 (a) for the hydrogen states around 12p. For positive k the state is shifted up in energy, while it is shifted down for negative k. For m = 0 we get the most extreme cases. The state $n_1 - n_2 = n - 1$ for example is shifted up in energy by $\frac{3}{2}(n-1)nF$ and is called the extreme blue Stark state. The state has a large permanent dipole moment and the Rydberg electron spends most of its time on the high field side of the proton. For the $n_2 - n_1 = n - 1$ state we get the opposite: the state is shifted down in energy and is called the extreme red state, for which the electron spends most of the

time on the low field side of the proton.
For a specific electric field $E_{\mathrm{IT}} \propto n^5$ the red n+1 and the blue n levels cross. This field is associated with the Inglis-Teller limit, where Stark broadening makes adjacent n levels unresolvable. For the hydrogen atom the two states cross perfectly at the crossing. This is the case because the conserved Runge-Lenz vector commutes with the Hamiltonian, leading to an extra degeneracy and no interaction.

Quadratic Stark effect

The quadratic Stark effect is obtained for non-degenerate energy levels with second order perturbation theory, where the shift in the energy levels is given by [32]

$$\Delta E = F \langle nlm\,|z|\,nlm\rangle + F^2 \sum_{n'l'm' \neq nlm} \frac{|\langle nlm\,|z|\,n'l'm'\rangle|^2}{E_{nlm} - E_{n'l'm'}}. \tag{2.27}$$

With the same selection rules $m' = m$ and $l' = l \pm 1$ as before, the linear term in the Stark shift vanishes and the sum is reduced to

$$\Delta E = F^2 \sum_{n',l'=l\pm1} \frac{|\langle nlm\,|z|\,n'l'm\rangle|^2}{E_{nlm} - E_{n'l'm'}} = -\frac{1}{2}\alpha_{nlm} F^2, \tag{2.28}$$

where α_{nlm} is known as the electrical polarizability of the atom in state $|nlm\rangle$. Qualitatively, the quadratic Stark effect can be explained as following: the applied electric field F induces an electric dipole moment $\vec{p} = \alpha_{nlm}\vec{F}$, which leads to an additional term in the energy of the atom proportional to F^2.
We will look at the shifts in the transition frequency $\Delta\nu_{Stark}$ induced by the quadratic Stark effect. For electric field strength F of less than 1 V/cm the Stark shift is [28]

$$\Delta\nu_{Stark} = \frac{1}{2}\Delta\alpha F^2. \tag{2.29}$$

For the $34p \leftrightarrow 34s$ transition in Helium, $\Delta\alpha$ is 1078 MHz $(V/cm)^{-2}$ [28]. Using the scaling law $\Delta\alpha \propto n^7$, we get $\Delta\alpha = 1948$ MHz $(V/cm)^{-2}$ for the $37p \leftrightarrow 37s$ transition, which we use in our experiment.

Non-hydrogen atoms

For non-hydrogen atoms the Stark effect is similar and can be calculated using a Numerov method, but there are two important differences due to the other electrons and finite sized cores of non-hydrogen atoms (see Figure 2.3 for a comparison of hydrogen and helium). First, the levels from the s and p states with nonzero quantum defects join the the manifold of the Stark states at a nonzero field. Theses states exhibit a quadratic Stark effect followed by a linear one for higher fields. Second, there are avoided crossings where the red n+1 and the blue n levels would meet. In contrast to the case of the hydrogen atom, the Coulomb potential

is modified and the Runge-Lenz vector is not conserved, meaning that the crossing becomes avoided [33].

Field ionization

Field ionization is of great importance for the detection of Rydberg atoms. It enables to determine the position [34] and the state of the Rydberg atom [33]. The simplest picture is given by looking at the potential of an atom in the electric F in z-direction as we had before. The combined Coulomb-Stark potential is given by

$$V = -\frac{1}{r} + Fz \tag{2.30}$$

and depicted in Figure 2.4. Classically, an atom with an energy E relative to the zero field can ionize if the energy E lies above the saddle point of the potential. The saddle point on the z axis is at $z = -1/\sqrt{F}$ and has a value of $V = -2\sqrt{F}$ there. The required field to ionize the atom is thus $F = E^2/4$. Without taking the Stark shift into account, we get with the energy relation $E = 1/n^2$ that the required field depends on the principle quantum number n as

$$F = \frac{1}{16n^4} \propto n^{-4}. \tag{2.31}$$

This was the classical approach. Some electrons also escape from the core potential by quantum mechanical tunneling at lower fields. Further on, the blue and the red states ionize at different fields due to their changed energy levels and different positions in the potential. The red state lies closer to the saddle point of the potential and ionizes at lower energies. This changes equation (2.31) to

$$F = \frac{1}{9n^4} \propto n^{-4} \tag{2.32}$$

for the most extreme red state. The blue states on the contrary lie on the up field side of the potential and are held there by an effective potential similar to a centrifugal potential [35]. For the extreme blue state the required field is about double as high as for the extreme red state. This means that the red states ionizes at lower fields then the blue states, which can be used for state selective detection.

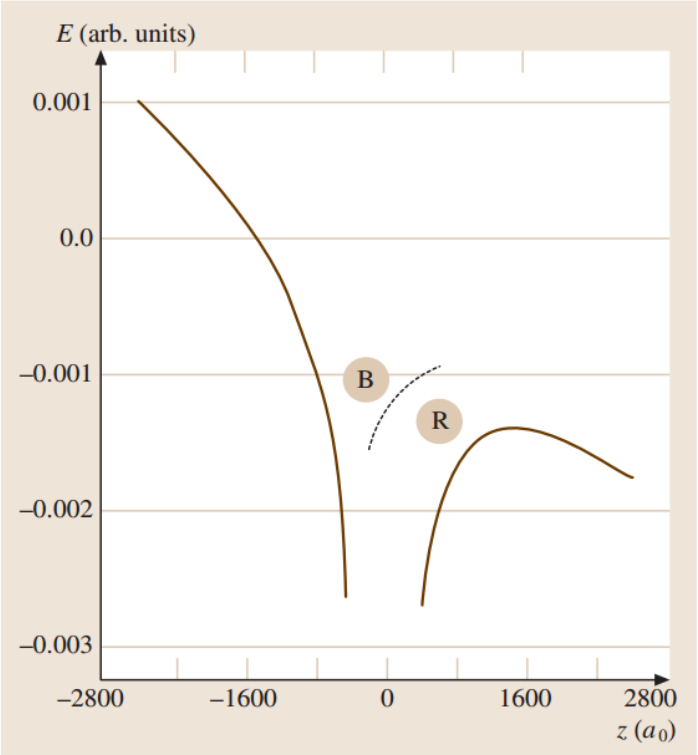

Figure 2.4.: *Combined Coulomb-Stark potential along the z axis for an applied field of 2700 V/cm in z-direction (solid line). The extreme red state R is near the saddle point, while the extreme blue state B is on the high field side of the atom. It is held there by an effective potential (dashed). Figure from [35]*

2.2. 3D microwave cavities

A 3D microwave cavity is a resonator that consists of a metal structure confining electromagnetic fields. The most common closed cavity geometries are rectangular and cylindrical. Some experiments also use open cavity geometries consisting of 2 parallel flat (Fabry-Pérot cavity) or parabolic mirrors [25]. In our case the cavity is rectangular with 4 slightly rounded edges (see section 3.4 for details on our cavity). The analytic formulae for the rectangular cavity can be used to estimate the properties of our cavity.

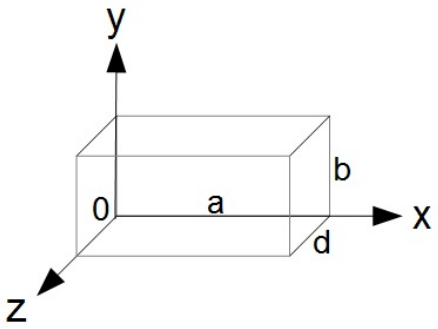

Figure 2.5.: *Schematic of a rectangular 3D cavity with length a, height b and depth d.*

A rectangular 3D cavity is defined by its width a, its height b and its depth d as shown in Figure 2.5. For the following formulae we will assume that a is the longest side, followed by d and then b. The cavity can in principle be filled with a dielectric material with permeability $\mu = \mu_r \mu_0$ and permittivity $\epsilon = \epsilon_r \epsilon_0$ (μ_r is the relative permeability of the material compared to the vacuum permeability μ_0 and analogously for the permittivity). In our case the cavity is either filled with air or with vacuum, which have nearly the same permittivity and permeability. Still a change in the resonance frequencies is visible due to the higher permittivity of air compared to vacuum ($\epsilon_{air} = 1.0006 \cdot \epsilon_0$), and the formula is thus given for different filling materials.
The most important property of a cavity is that only certain modes can be excited. We will first look at the mode spectrum of a rectangular cavity and then review another essential quantity, the quality factor.

2.2.1. Modes

The electromagnetic field inside the cavity has to fulfill Maxwell's equations and the boundary conditions, meaning that

1. the divergence of the electric field has to be zero as there is no electric field source inside the cavity,

2. the electric field close to the conductor has to be zero or orthogonal to the conductor surface,

3. the magnetic field close to the conductor has to be zero or parallel to the conductor surface.

These boundary conditions lead to the quantization of the cavity field into modes and can only be fulfilled by the TE (transverse electric) and the TM (transverse magnetic) modes, but not the TEM (transverse electromagnetic) modes. TE and TM modes also occur in rectangular waveguides, where the TE mode has the electric field orthogonal to the propagation direction of the wave, while for the TM mode the magnetic field is orthogonal to the propagation direction. A cavity can be obtained from a waveguide by short circuiting both ends (longest side a), thus forming a closed box. The propagating wave of the waveguide turns into a standing wave in the cavity that has zero electric field at the cavity boundaries. This means that the cavity only supports waves with integer multiples of the half wavelength corresponding to all three cavity dimension. We can define a resonance wave number k_{mnl} for the rectangular cavity as [36]

$$k_{mnl} = \sqrt{\left(\frac{m\pi}{a}\right)^2 + \left(\frac{n\pi}{b}\right)^2 + \left(\frac{l\pi}{d}\right)^2}. \tag{2.33}$$

The modes are labeled with the indices m, n and l by counting the number of antinodes in the standing wave pattern in the x, y and z directions, respectively. The resonant frequency of

the TE_{mnl} and the TM_{mnl} mode is given by [36]

$$f_{res} = \frac{ck_{mnl}}{2\pi\sqrt{\mu_r\epsilon_r}} = \frac{c}{2\pi\sqrt{\mu_r\epsilon_r}}\sqrt{\left(\frac{m\pi}{a}\right)^2 + \left(\frac{n\pi}{b}\right)^2 + \left(\frac{n\pi}{d}\right)^2}. \tag{2.34}$$

Using the property b<d<a, the lowest frequency mode occurs for TE_{101}. In our cavities we use the TE_{301} mode, which has 3 maxima in the electric field magnitude along the x-direction and one along the z-direction. In y-direction the field is constant. The TE_{301} mode is the third lowest mode.

2.2.2. Quality factor, coupling and insertion loss

An important quantity for a resonator is the quality factor Q measuring the rate of energy loss compared to the stored energy. The oscillations of a resonator with a high Q decay slower and the resonators damping is lower. We distinguish between 3 different quality factors: the internal quality factor of the resonator Q_{int}, the external quality factor of the measurement system Q_{ext} and the combined quality factor Q. The internal quality factor Q_{int} of a cavity results from the power dissipated in the finite resistance of the metallic walls and in the dielectric filling. For the TE_{l01} mode of a rectangular waveguide, the internal quality factor due to the sheet resistance R_s of the metallic walls can be calculated analytically with [36]

$$Q_{TEl01} = \frac{k^3\eta}{2\pi^2 R_s} \cdot \frac{(ad)^3\, b}{2l^2d^3b + 2ba^3 + l^2d^3a + da^3}, \tag{2.35}$$

where $\eta = \sqrt{\mu/\epsilon}$ is the intrinsic impedance of the dielectric. The internal quality factor due to the dielectric filling can be calculated with the inverse of the loss tangent of the dielectric material. External losses due to radiation and the coupling of the cavity to the measurement system are accounted for with the external quality factor Q_{ext}. The three quality factors are related by the equation

$$\frac{1}{Q} = \frac{1}{Q_{int}} + \frac{1}{Q_{ext}}. \tag{2.36}$$

How well the resonator is coupled to the outside (e.g. the measurement system) can be described by the coupling coefficient g, which is defined by

$$g = \frac{Q_{int}}{Q_{ext}}. \tag{2.37}$$

The coupling can be increased by sticking the coupling pins exciting the cavity mode further into the cavity. The resonator is called [37]

- overcoupled if $g \gg 1 \Rightarrow Q \approx Q_{ext}$,
- critically coupled if $g = 1$ and
- undercoupled if $g \ll 1 \Rightarrow Q \approx Q_{int}$.

The quality factors can be found in two-port measurements using a network analyzer [36]. When measuring the power transmission coefficient $|S_{21}|^2$ as a function of frequency, a Lorentzian lineshape (compare with Figure 2.38) is obtained for each resonance. Three quantities define the Lorentzian function: the amplitude A, the resonance frequency f_0 and the bandwidth δf at full width half maximum. The Lorentzian function is given by

$$F_{Lor} = \frac{A}{\left(\frac{f-f_0}{(\delta f/2)}\right)^2 + 1}. \tag{2.38}$$

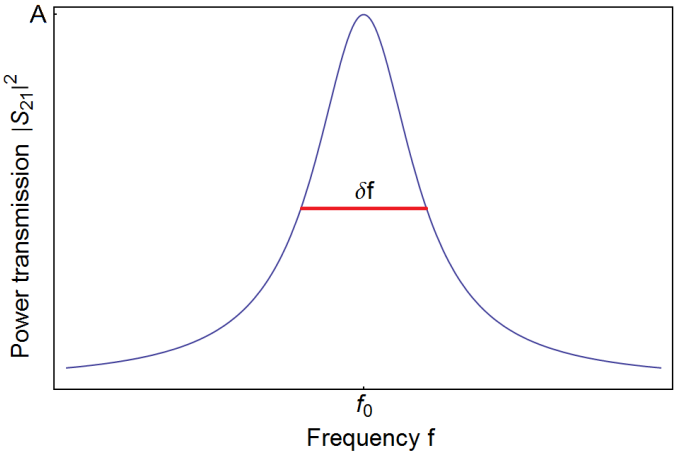

Figure 2.6.: *Lorentzian for the definition of the quality factors. From [38]*

With these quantities the quality factor Q is defined as

$$Q = \frac{f_0}{\delta f}. \tag{2.39}$$

The internal and external quality factor can also be obtained from the fit by describing the microwave cavity as a series RLC circuit. In this case the coupling g is given by [36]

$$g = \frac{\sqrt{A}}{1-\sqrt{A}}, \tag{2.40}$$

where $\sqrt{A}$ already replaces $S_{21}(f_0)$. Using equations (2.37), (2.36) and (2.40), the internal and external quality factor can be obtained:

$$Q_{int} = \frac{Q}{1-\sqrt{A}} \tag{2.41a}$$

$$Q_{ext} = \frac{Q}{\sqrt{A}}. \tag{2.41b}$$

In order to measure the internal quality factor directly with the network analyzer, the cavity has to be undercoupled.

The insertion loss of a resonator expresses the deviation of peak transmission from unity and depends on the coupling coefficient g [37]:

$$L_0 = -20\log\left(\frac{g}{g+1}\right)dB \overset{(2.40)}{=} -10\log\left(A\right)dB. \tag{2.42}$$

From the 3 quality factors the coupling coefficients $\frac{\kappa}{2\pi}$, $\frac{\kappa_{int}}{2\pi}$ and $\frac{\kappa_{ext}}{2\pi}$ can be calculated:

$$\frac{\kappa}{2\pi} = \frac{f_0}{Q} \tag{2.43}$$

and analogous for $\frac{\kappa_{int}}{2\pi}$ and $\frac{\kappa_{ext}}{2\pi}$. The coupling coefficient $\frac{\kappa}{2\pi}$ corresponds to the width δf of the resonance and κ describes the decay rate of the field energy stored inside the resonator. This decay rate is composed of the photon decay rate due to dissipation described by κ_{int} and the photon escape rate to the ports described by κ_{ext}. By changing the coupling, the photon escape rate into the measurement system can be adjusted.

2.3. Cavity QED

The field of cavity quantum electrodynamics (cavity QED) studies the interaction between a spin-$\frac{1}{2}$ particle and a quantum harmonic oscillator [25]. In our experiment the Rydberg atom represents the spin and the 3D microwave cavity the harmonic oscillator. The interaction strength between an atom and a mode of the free space vacuum field is weak, while the quantized modes inside a cavity can have a high electric field strength due to the reduced mode volume and multiple reflections resulting in resonances. This leads to an enhanced dipole coupling between the atom and the cavity. Usually cavities with a high quality factor are chosen, which gives the photons within the cavity the possibility to interact many times with the atoms before escaping. This setup provides us with the opportunity to study and control single quantum systems and can be exploited for quantum information processing [1].

2.3.1. Jaynes-Cummings Hamiltonian

The combined system of the atom and the cavity can be described with the Jaynes-Cummings model, which was originally proposed by Edwin Jaynes and Fred Cummings in 1963 to describe the phenomenon of spontaneous emission [39]. The Jaynes-Cummings model is not limited to atoms, but can also be applied to artificial atoms, like superconducting qubits, coupled to a resonator [40].
The Jaynes-Cummings Hamiltonian consists of the atomic Hamiltonian H_a, the cavity Hamiltonian H_c and the coupling Hamiltonian H_{ac} as well as the damping terms H_γ and H_κ [41]:

$$H = H_a + H_c + H_{ac} + H_\gamma + H_\kappa. \tag{2.44}$$

We will now go through all components separately and start with the atom. As a simplification it is described as a two-level system with a transition frequency ω_a between the ground state

$|g\rangle$ and the excited state $|e\rangle$ and can be modeled as a spin-$\frac{1}{2}$ particle with the Hamiltonian

$$H_a = \frac{1}{2}\hbar\omega_a\sigma_Z, \tag{2.45}$$

where σ_Z is the Pauli z matrix. The cavity can be described with the well known Hamiltonian of a harmonic oscillator:

$$H_c = \hbar\omega_c\left(a^\dagger a + \frac{1}{2}\right), \tag{2.46}$$

using the creation ($a^\dagger$) and annihilation (a) operators. The coupling Hamiltonian H_{ac} in the dipole approximation is given by [25]

$$H_{ac} = -\vec{D}\cdot\vec{E_c}, \tag{2.47}$$

where $\vec{D}$ is the atomic dipole operator and $\vec{E_c}$ the cavity electric field operator at the atomic location. The atomic dipole operator is [42]

$$\vec{D} = \vec{d}\cdot\sigma_x = \vec{d}\cdot(\sigma_+ + \sigma_-), \tag{2.48}$$

where $\vec{d}$ is the transition dipole moment, σ_x is the Pauli x matrix and $\sigma_\pm$ are the atomic raising and lowering operators fulfilling the conditions $\sigma_+|g\rangle = |e\rangle$ and $\sigma_-|e\rangle = |g\rangle$. The electric field operator,

$$\vec{E_c} = \vec{\mathcal{E}}_{rms} f(r)\left(a + a^\dagger\right), \tag{2.49}$$

can be derived by quantizing the electric field. It depends on the cavity spatial mode $f(r)$, which for example varies sinusoidally inside a rectangular cavity, and the rms zero-point electric field $\mathcal{E}_{rms}$, which can be calculated with

$$\mathcal{E}_{rms} = \sqrt{\frac{\hbar\omega_c}{2\epsilon_0 V}}, \tag{2.50}$$

where ϵ_0 the vacuum permittivity. The mode volume V of the excited mode can be obtained by integrating the mode function squared over the cavity volume. From equation (2.50) it becomes clear that a smaller mode volume leads to a higher zero-point electric field inside the cavity and thus a stronger coupling.

We can now insert equations (2.48) and (2.49) into equation (2.47). The expansion of the operator scalar product involves four terms. One of them is proportional to $\sigma_+ a$, which stands for the excitation of the atom by photon absorption. Another is proportional to $\sigma_- a^\dagger$ and corresponds to the inverse process in which the excited state decays and a photon is emitted. When the cavity resonance ω_c and the atomic transition frequency ω_a are close, the two terms conserve the energy. Under this condition the two other cases proportional to $\sigma_+ a^\dagger$ and $\sigma_- a$ correspond to two highly non-resonant processes: for $\sigma_+ a^\dagger$ the atom is excited and a photon emitted, while for $\sigma_- a$ the atom decays from the excited to ground state and a photon is annihilated. Neglecting these two anti-resonant terms is equal to performing the rotating wave

approximation [25]. The resulting coupling Hamiltonian is [41]

$$H_{ac} = \hbar g \left(a^\dagger \sigma_- + a \sigma_+ \right), \tag{2.51}$$

where g is called the coupling constant, which can be calculated with [41]

$$g = \frac{\vec{\mathcal{E}}_{rms} \vec{d}}{\hbar}. \tag{2.52}$$

The two damping terms include that in reality the atom and the chosen cavity mode are not the only terms coupling to each other. The damping term H_γ describes the coupling of the atom to other cavity modes causing the excited state to decay at the rate γ. The coupling of the cavity to the continuum produces the cavity decay rate $\kappa = \omega_c / Q$ and is described by H_κ. The case in which the coupling constant g is a lot larger than the decay rates κ and γ is called the strong coupling limit. This is the interesting regime for cavity QED as the coherent exchange of energy between the quantized electromagnetic field and the quantum two-level system can be observed [40]. The total Jaynes-Cummings Hamiltonian can now be written as

$$H = \frac{1}{2} \hbar \omega_a \sigma_Z + \hbar \omega_c \left(a^\dagger a + \frac{1}{2} \right) + \hbar g \left(a^\dagger \sigma_- + a \sigma_+ \right) + H_\gamma + H_\kappa. \tag{2.53}$$

2.3.2. Dressed states

In the absence of damping, the eigenstates can be found by diagonalization of the Jaynes-Cummings Hamiltonian. Let us first examine the uncoupled eigenstates of $H_a + H_c$ given by the tensor products $|e, n\rangle$ and $|g, n\rangle$ of the atomic and cavity energy states. The states have energies $\pm \frac{\hbar \omega_a}{2} + \hbar \omega_c \left(n + \frac{1}{2} \right)$, where the higher energy belongs to the atom being in the excited state. For small detunings $\Delta = \omega_a - \omega_c$ the states $|e, n\rangle$ and $|g, n+1\rangle$ are nearly degenerate. The energy states are then organized as a ladder of doublets separated by $\hbar \omega_c$. The only unpaired state is the ground state $|g, 0\rangle$ at the bottom of the ladder, representing the unexcited atom in the cavity vacuum. Each doublet $|g, n+1\rangle$ and $|e, n\rangle$ stores $n+1$ elementary excitations, either as $n+1$ photons or as n photons plus one atomic excitation. The operator $M = a^\dagger a + \sigma_+ \sigma_-$ represents the total number of atomic and field excitations.

Due to the commutation relation $[M, H] = 0$, the atom field coupling H_{ac} only connects states inside each doublet, leaving the excitation number conserved [25]. It is therefore sufficient to diagonalize the Hamiltonian in the basis $|e, n\rangle$ and $|g, n+1\rangle$ of one doublet. In this basis the Hamiltonian is given by

$$H^{(n)} = \begin{pmatrix} \hbar \omega_c \left(n + \frac{1}{2} \right) + \frac{\hbar \omega_a}{2} & \hbar g \sqrt{n+1} \\ \hbar g \sqrt{n+1} & \hbar \omega_c \left((n+1) + \frac{1}{2} \right) - \frac{\hbar \omega_a}{2} \end{pmatrix}. \tag{2.54}$$

The eigenvalues of $H^{(n)}$ represent the energies of the excited eigenstates of the undamped

Jaynes-Cummings Hamiltonian:

$$E_{\pm,n} = \hbar\omega_c (n+1) \pm \frac{\hbar}{2}\sqrt{\Delta^2 + 4g^2 (n+1)}, \tag{2.55}$$

with the corresponding eigenstates, called the *dressed states*:

$$\begin{aligned} |+,n\rangle &= \cos(\Theta_n)\,|e,n\rangle + \sin(\Theta_n)\,|g,n+1\rangle \\ |-,n\rangle &= \sin(\Theta_n)\,|e,n\rangle - \cos(\Theta_n)\,|g,n+1\rangle\,. \end{aligned} \tag{2.56}$$

The mixing angle Θ_n is given by

$$\tan(2\Theta_n) = \frac{2g\sqrt{n+1}}{\Delta}. \tag{2.57}$$

The energy of the ground state $|g,0\rangle$ does not change due to the coupling, but remains at $E_{-,0} = -\frac{\hbar\Delta}{2}$.

Two limiting cases are interesting: the resonant case with $\Delta \approx 0$ and the large detuning case $\Delta \ll g$, which is also called the dispersive limit. For zero detuning the uncoupled states $|e,n\rangle$ and $|g,n+1\rangle$ cross. Due to the coupling between the atom and the cavity, this crossing is avoided as can be seen in Figure 2.7. For very large detunings, the dressed states almost coincide with the uncoupled states. We will now have a closer look at these two limiting cases.

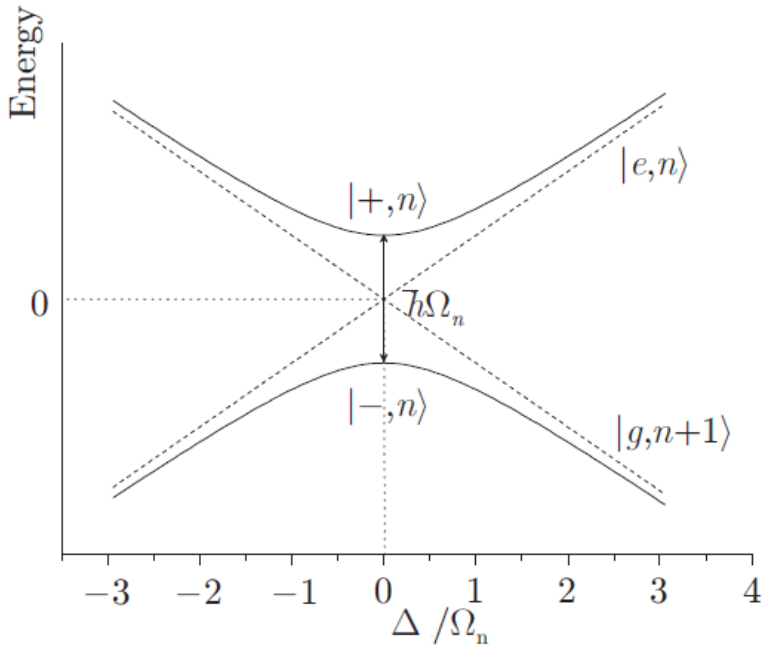

Figure 2.7.: *Dressed states in the Jaynes-Cummings model for different detunings* Δ*. The uncoupled state energies are represented as dotted lines. From [25]*

2.3.3. Resonant case: Rabi oscillations

For zero detuning, the mixing angle is $\Theta_n = \pi/4$ for all n values. This simplifies the dressed states from equation (2.56) to

$$\begin{aligned} |+,n\rangle &= \frac{1}{\sqrt{2}}\left(|e,n\rangle + |g,n+1\rangle\right) \\ |-,n\rangle &= \frac{1}{\sqrt{2}}\left(|e,n\rangle - |g,n+1\rangle\right). \end{aligned} \tag{2.58}$$

These two states are called the polariton states and are separated by an energy $2\hbar g\sqrt{n+1}$, which can be obtained from equation 2.55 by inserting $\Delta = 0$. The polariton states are analogous to the normal modes of two coupled degenerate oscillators, which are also given by the symmetric and anti-symmetric superpositions of the independent free modes [25]. They can be observed in spectroscopy measurements of the cavity frequency. The phenomena is called vacuum Rabi mode splitting and has been witnessed for atoms in an optical cavity [43] and superconducting qubits coupled to a resonator [44].

Another interesting consequence based on the fact that the states $|e,n\rangle$ and $|g,n\rangle$ are not the eigenstates of the Jaynes-Cummings Hamiltonian are Rabi oscillations. The atom-field coupling leads to a reversible exchange of an energy quantum between the $|e,n\rangle$ and the $|g,n\rangle$ state. A system prepared in the initial state $|e,n\rangle$ evolves to the state $|g,n\rangle$ by the emission of a photon and back by reabsorption of the photon. These oscillations occur at the so called n *photon Rabi frequency* Ω_n depending on the doublet they occur between. The Rabi frequency can be calculated from the energy difference between the two polariton eigenstates of the oscillation:

$$\Omega_n = 2g\sqrt{n+1}. \tag{2.59}$$

For the initial states $|e,0\rangle$ or $|g,1\rangle$ this oscillation takes place with a frequency $\Omega_0 = 2g$ called the vacuum Rabi frequency. It can be seen as an oscillatory spontaneous emission [25].

When the transition is driven with a strong coherent drive tone with an amplitude $\alpha \ll 1$ as it is, for example, the case in our experiment, the tone can be approximated by a Fock state $|n\rangle$ with $n = |\alpha|^2$. In this limit the n photon Rabi frequency Ω_n converges to the Rabi frequency $\Omega = 2g\,|\alpha|$.

Rabi oscillations also exist in the case that the detuning is not exactly zero. The Rabi frequency Ω for zero detuning is then increased and given by the generalized Rabi frequency Ω' [45]:

$$\Omega' = \sqrt{\Omega^2 + \Delta^2}. \tag{2.60}$$

In the experiment we drive Rabi oscillations with a classical microwave pulse inside the 3D cavity for a certain duration δt. For a population of atoms that is initially in the s state, the excitation probability to the p state is given by [28]

$$P_{s\to p}\left(\Delta,\Omega,\delta t\right) = \frac{\Omega^2}{\Delta^2+\Omega^2}\sin^2\left(\frac{\delta t}{2}\sqrt{\Delta^2+\Omega^2}\right) = \left(\frac{\Omega}{\Omega'}\right)^2 \cdot \sin^2\left(\frac{\delta t}{2}\Omega'\right). \tag{2.61}$$

If the we apply the pulse exactly on resonance, we can drive the whole population from the s to the p state by implementing a pulse with the duration $\delta t = \pi/\Omega$, which is known as a π-pulse. In the case of non-zero detuning, we can just drive a fraction of maximally $(\Omega/\Omega')^2$ of the population to the p state. From Rabi frequency measurements we can draw conclusions on the detuning and the fields inside the cavity that the atoms interact with.

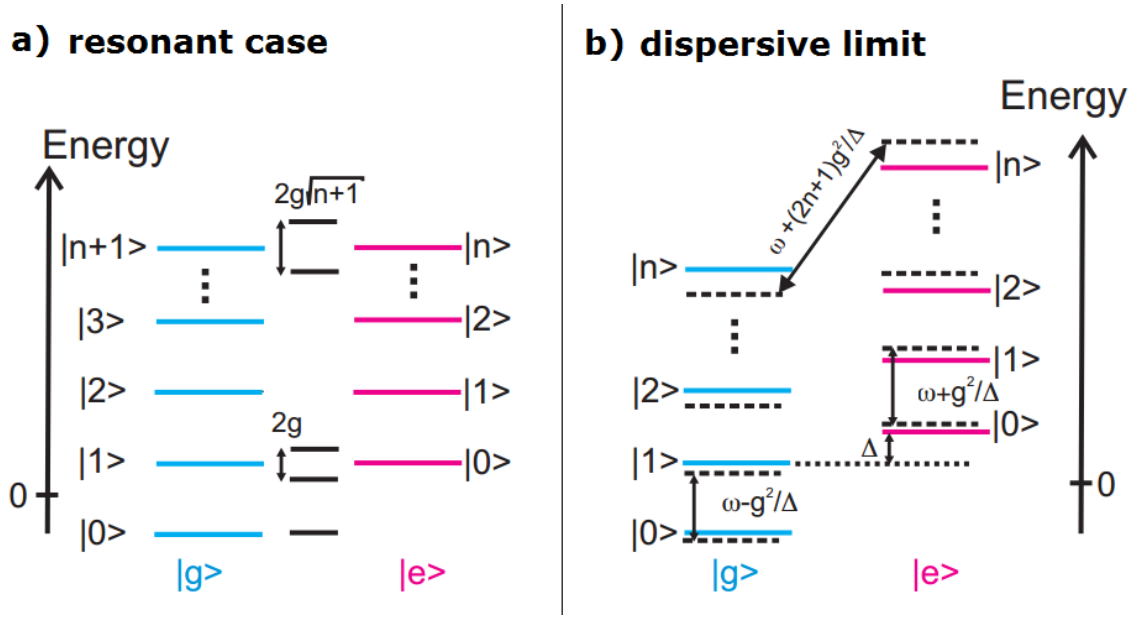

Figure 2.8.: *States in the Jaynes-Cummings model. The blue and the pink levels are the uncoupled states of the Hamiltonian $H_a + H_c$. The blue states $|g, n\rangle$ correspond to the ground state of the atom with n excitation as given to the left of the respective state, while the pink states $|e, n\rangle$ correspond to the excited atom states with n photons as noted on the right of the state. The resonant case is displayed in a) and shows the coupled eigenstates (polariton states) in the middle. The coupled states in the dispersive limit with a detuning $\Delta > 0$ are shown in b). Here each uncoupled state is subject to a slight shift in energy. The transition frequencies between the coupled states are shown above the arrows. In b) ω stands for the frequency of the transition between the uncoupled states. Figure from [41] and edited.*

2.3.4. Dispersive limit

For large detunings $\Delta \gg g$, we are in the dispersive limit, where the dressed states tend towards the uncoupled states, $|e, n\rangle$ and $|g, n+1\rangle$, as we have seen in Figure 2.7. In this case $\left(\frac{\Omega}{\Omega'}\right)^2$ is negligibly small, meaning that we do not observe Rabi oscillations and no excitations are exchanged between the atom and the cavity. There is however a renormalization of the energy due to the coupling. This leads to shifts in the energy levels, which can be calculated by expanding the energy level equation (2.55) under the condition $g/\Delta \ll 1$. More insightful is however applying a unitary transformation to the Jaynes-Cummings Hamiltonian. The

relevant transformation is [41]

$$U = \exp\left[\frac{g}{\Delta}\left(a\sigma_+ - a^\dagger\sigma_-\right)\right], \tag{2.62}$$

which leads us to the Hamiltonian in the dispersive limit [41]:

$$H_{disp} = UHU^\dagger = \hbar\left(\omega_c + \frac{g^2}{\Delta}\right)a^\dagger a + \frac{\hbar}{2}\left(\omega_a + \frac{g^2}{\Delta}\right)\sigma_z \tag{2.63}$$

From this expression we can conclude that the atomic transition is shifted by $\frac{g^2}{\Delta}n + \frac{1}{2}\frac{g^2}{\Delta}$, where the first term is called the *AC-Stark shift* and the second the *Lamb shift*. The AC-Stark shift is also known as *light shift* and depends on the number of photons n in the resonator. Light shifts were first predicted and observed by Claude Cohen-Tannoudji in 1966 [45]. They have recently been observed for Rydberg atoms [46] and for superconducting qubits [47]. The Lamb shift is named after one of its discoverers, Willis Lamb, and was first measured by him and Robert Retherford in 1947 [48]. The Lamb shift was also observed in Rydberg systems [49] and for superconducting qubits [50].
On the other hand, the shifts can also be viewed as an atomic state dependent shift of the cavity frequency. The cavity experiences a so called *dispersive shift* χ, which in the case of positive detuning increases the cavity resonance frequency ω_c if the atom is in the excited state, and decreases the frequency if the atom is in the ground state. The dispersive shift is

$$\chi = \frac{g^2}{\Delta}. \tag{2.64}$$

This effect allows to perform quantum non-demolition measurements on the atomic/qubit state, meaning that the qubit state can be read out without disturbing it. These dispersive readouts are regularly used with superconducting circuits [40] and Rydberg atoms [25]. One of the main tasks in this master's thesis is to prepare and characterize the amplification system necessary for detecting a dispersive shift. The shift can be seen in amplitude and phase measurements of the transmission through the cavity for different frequencies.

2.4. Noise in amplifiers

An important parameter describing an amplifier is the gain G. Assuming that the amplifier is linear and deterministic, the output power P_{out} can be calculated from the input power P_{in} with $P_{out} = G \cdot P_{in}$. In reality, the amplifier only performs in this ideal way in the so called *dynamic range* [36]. For powers above this range, the output power no longer increases linearly with the input power, but begins to saturate. The one-dB compression point describes the input power for which the output power varies by 1 dB from the ideal linearly extrapolated gain curve of the amplifier. Excessive input powers cause the amplifier to fail. At the other extreme, very low input power levels will result in an output dominated by the noise generated by the amplifier. Even at zero input power, the amplifier delivers nonzero noise power, because

the amplifier generates noise by itself. This level is called the *noise floor* of the amplifier. The noise level sets a lower limit on the strength of a signal that can be detected [36]. It is hence desirable to minimize the noise level of the system.

Sources of noise

Internal noise of a device is usually generated by the random motion of charge carriers inside the device. Depending on the the mechanism causing the motion, we distinguish between different types of noise [36]. The most basic type is *thermal noise* (also known as Johnson or Nyquist noise), which arises due to the thermal vibration of bound charges. *Shot noise* occurs in solid-state devices due to random fluctuation of charge carriers. The quantum nature of charge carriers and photons leads to *quantum noise*, which is however often insignificant compared to other noise sources. In solid-state components *Flicker noise* can be found, whose power varies inversely with frequency.
Regardless of the source, we talk about *white noise* when the power spectral density is nearly constant throughout the frequency spectrum of the component. In this case we can characterize the noise effects of a component in terms of noise temperature and noise figure.

2.4.1. Noise temperature

In 1928, John B. Johnson studied and described the statistical fluctuations of electric charge in conductors [51]. He reported his discoveries to Harry Nyquist, who was able to explain his results and formulated a first version of the fluctuation-dissipation theorem [52]. This theorem was proven by Herbert Callen and Theodore A. Welton in 1951 [53]. It is valid for both classical and quantum mechanical systems and can for example be applied to Brownian motion and thermal noise. The fluctuation-dissipation theorem describes the relation between dissipation (described by the resistance) and certain fluctuations. In the case of thermal noise, the relevant fluctuations are in the voltage.
Let us consider a resistor R at a physical temperature T. The electrons in the resistor have a kinetic energy proportional to the temperature and move randomly. This produces random voltage fluctuations between the two ends of the resistor. The average voltage is 0, but the root mean square (rms) value is given by Planck's blackbody radiation law [36]

$$V_{rms} = \sqrt{\frac{4h \cdot f \cdot B \cdot R}{e^{hf/k_B T} - 1}}, \tag{2.65}$$

where B is the bandwidth of the system, f the center frequency of the bandwidth, k_B Boltzmann's constant and h Planck's constant. At microwave frequencies, where $hf \ll kT$, we can use Taylor expansion to approximate the exponential term:

$$e^{hf/k_B T} - 1 \approx \frac{hf}{k_B T}. \tag{2.66}$$

In our noise temperature measurements f is 21 GHz and the lowest temperature around 10

K. In this case $hf = 1.39 \cdot 10^{-23}$ J is ten times smaller than $k_B T = 1.38 \cdot 10^{-22}$ J and the approximation gives valid results.

The root mean square voltage in this approximation is simply

$$V_{rms} = \sqrt{4 k_B T B R}. \tag{2.67}$$

The noisy resistor can be described with the Thevenin equivalent circuit consisting of a noiseless resistor and a voltage generator supplying the voltage V_{rms}. The maximum noise power transfer is achieved in the impedance matching case, in which the Thevenin equivalent circuit is connected to a load with resistance R. The maximum noise power from a noisy resistor is thus given by

$$N = I_{rms}^2 \cdot R = \left(\frac{V_{rms}}{2R} \right)^2 \cdot R = \frac{V_{rms}^2}{4R} = k_B B T, \tag{2.68}$$

which is independent of the the resistance R and the frequency (white noise). The noise power is directly proportional to the temperature T. It therefore makes sense to describe the noise power of a source by this temperature. For a source creating white noise (in some fixed bandwidth B) with a noise power N, we can define the *equivalent noise temperature* T_e by

$$T_e = \frac{N}{k_B B}. \tag{2.69}$$

In a similar way we can define the noise temperature of an amplifier with gain G. If we connect the amplifier to a source with a (hypothetical) temperature $T_S = 0$ K, then the input power of the amplifier will be $N_{in} = 0$ and the output power N_{out} the noise generated by the amplifier itself. Since we can not connect a noiseless source, we model the system with an equivalent system consisting of a noiseless amplifier connected to a source at temperature T_e. The input noise power N_{in} to the amplifier is then equal to $k_B B T_e$ and the output noise power given by $N_{out} = G \cdot N_i$. The system has the same output noise power, when the temperature is given by

$$T_e = \frac{N_{out}}{G k_B B}, \tag{2.70}$$

which is known as the equivalent noise temperature of the amplifier. The noise temperature can also be used to describe the noise level in systems with more than one component.

2.4.2. Noise figure, signal-to-noise ratio and cascaded systems

A noisy microwave component can be characterized by an equivalent noise temperature T_e or alternatively with the *noise figure* F, which measures the degradation in the signal-to-noise ratio (SNR) between input and output of the component. The signal-to-noise ratio compares the desired signal power S with the undesired noise power N. With this definition, the noise

figure is given by

$$F = \frac{S_{in}/N_{in}}{S_{out}/N_{out}} \geq 1, \tag{2.71}$$

where the subscript *in* stands for the input and *out* for the output. We can now use noise temperatures to calculate the noise powers. The input noise power from a source at temperature T_0 is given by $N_{in} = k_B T_0 B$. The output noise power is the sum of the amplified input noise and the noise generated by the amplifier: $N_{out} = k_B G B T_0 + k_B G B T_e$. The output signal power is simply obtained by multiplying the input signal power with the gain. Equation (2.71) can then be rewritten as

$$F = \frac{S_{in}/k_B T_0 B}{G S_{in}/k_B G B\,(T_0 + T_e)} = 1 + \frac{T_e}{T_0}. \tag{2.72}$$

In this way we have found a relation between the noise figure F and the noise temperature T_e. In appendix A.2 there is a table converting the noise figure in dB to the associated noise temperature in Kelvin for the range of our amplifiers.

Cascaded systems

A typical microwave system consists of a cascade of many different components. Each of these components degrades the signal-to-noise ratio. From the noise figure F_i or the noise temperature T_i of the individual components with gain G_i, we can calculate the noise figure or temperature of the whole system. The noise figure of the cascaded system is given by [36]

$$F_{cas} = F_1 + \frac{F_2 - 1}{G_1} + \frac{F_3 - 1}{G_1 G_2} + \ldots \tag{2.73}$$

and the noise temperature by

$$T_{cas} = T_1 + \frac{T_2}{G_1} + \frac{T_3}{G_1 G_2} + \ldots. \tag{2.74}$$

These equations lead to the important conclusion that the noise characteristics of a cascaded system are dominated by the first stage. The effect of the second stage is reduced by the gain of the first and the later stages have even less impact on the overall noise performance. Due to this reason, the first stage should have a very low noise figure and a high gain.

3. Experimental setup and measurement procedure

The experimental setup used in this Master's thesis to manipulate Rydberg atoms with a 3D microwave cavity is described in [27, 28]. The setup consists of 3 main vacuum chambers of different pressures: the source chamber in which the atomic beam is generated, the cryogenic chamber with a pulse-tube cooler and the experimental chamber where the microwave resonator is placed (see Figures 3.1 and 3.2). To get an overview, we will follow a helium atom's path through the setup with our description. All parts of the setup will be described in more detail in the following sections of this chapter.

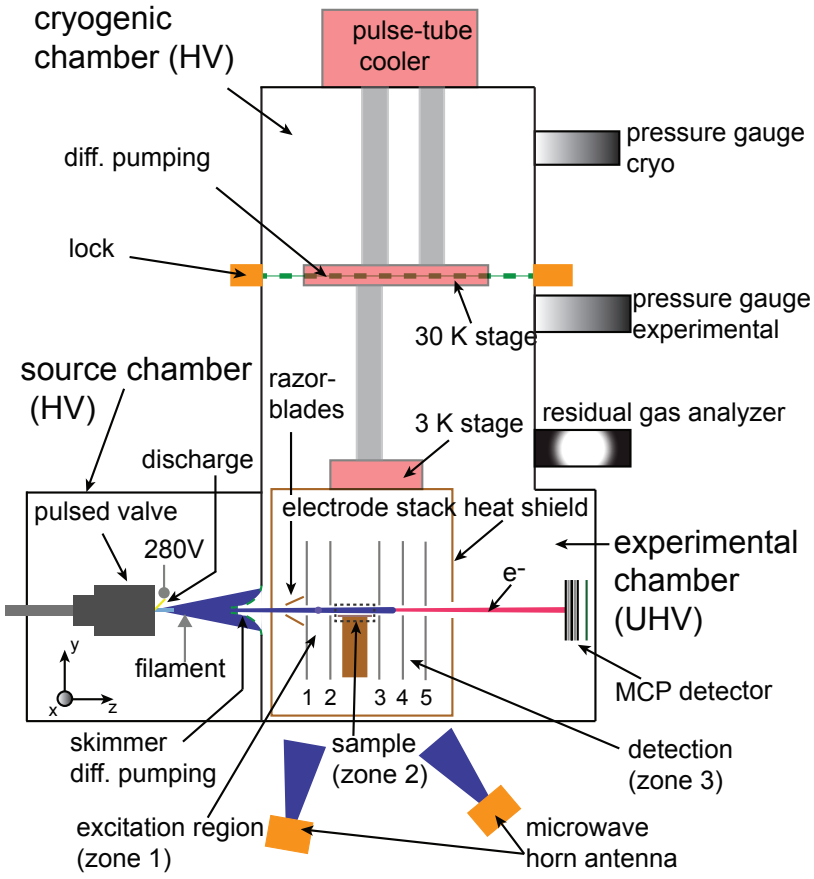

Figure 3.1.: *Schematic view of the experimental setup. Figure from [28].*

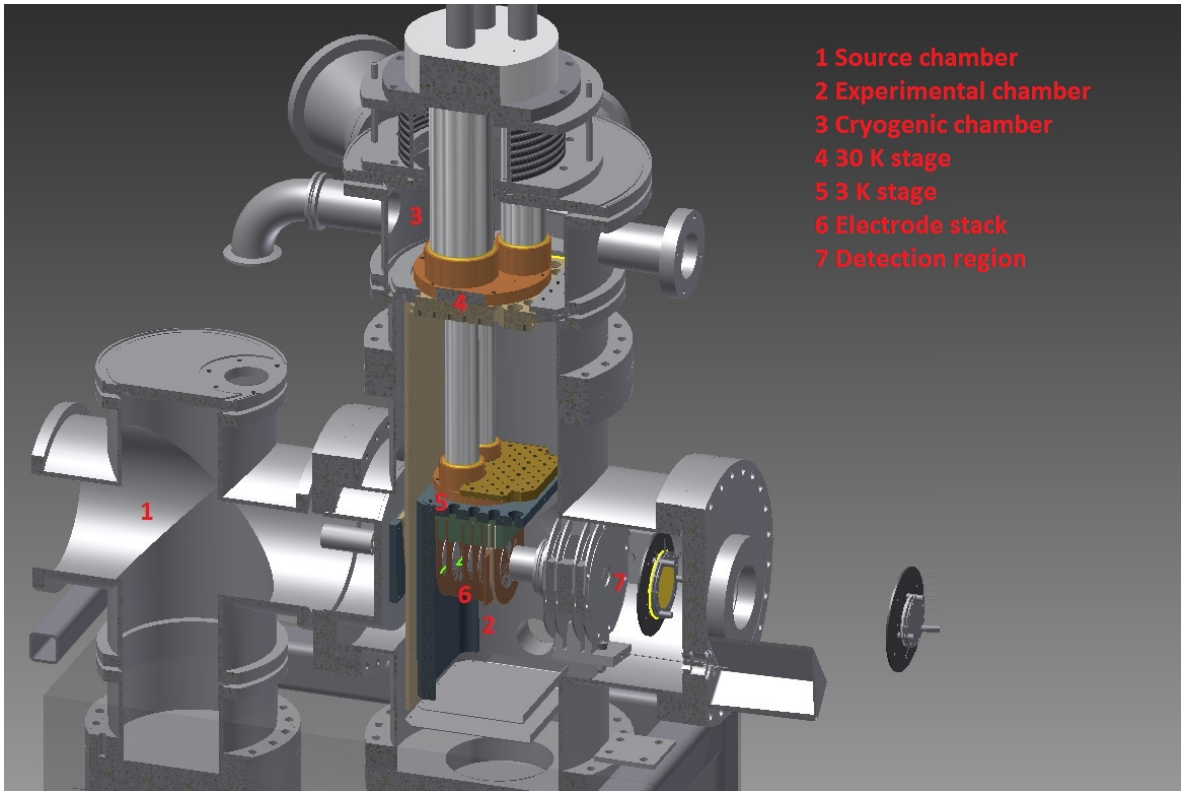

(a) *CAD picture of the setup.*

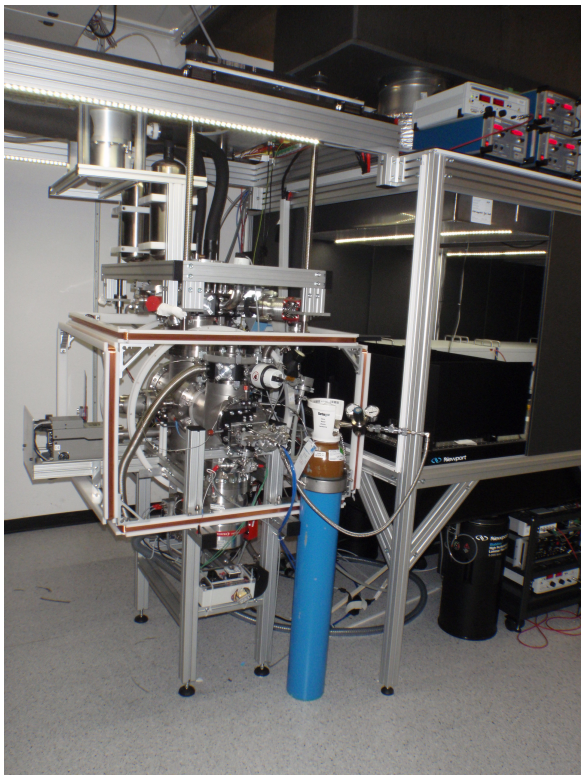

(b) *Photograph of the total setup: Vacuum chambers on the left, optical table that hosts the excitation laser on the right.*

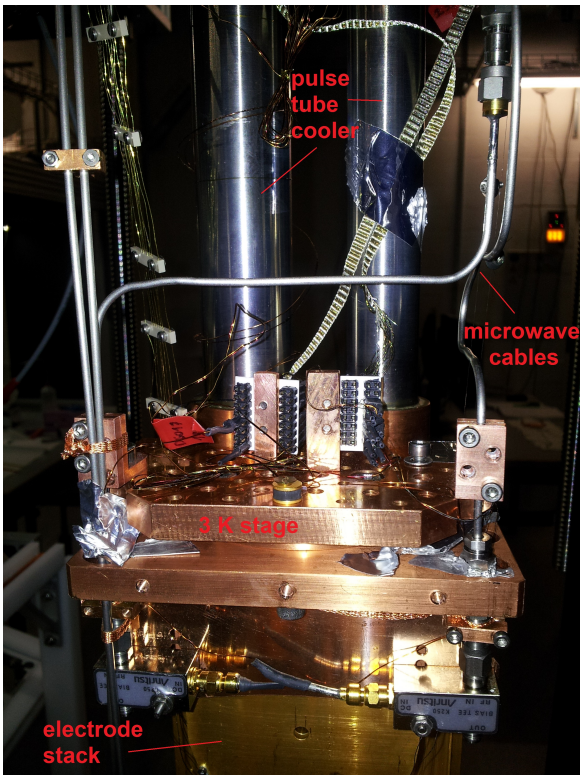

(c) *Photograph of the 3K stage with the tubes of the pulse tube cooler and the electrode stack below.*

Figure 3.2.: *CAD model and photographs showing parts of the setup.*

Overview

In the source chamber the helium atom beam is generated at the valve orifice and undergoes a supersonic expansion. A pulsed electric discharge created by electrons from a hot filament transfers the helium atoms to the metastable $(1s)^1\,(2s)^1\ {}^1S_0$ state. These metastable helium atoms He* then travel through a skimmer with a 1-mm-diameter hole from the source chamber into the experimental chamber. The beam can be further collimated in the horizontal plane by two parallel razor blades. In the experimental chamber there are 7 circular electrodes with 5-mm-diameter holes in the middle, through which the beam can pass (see Figure 3.3). The electrodes divide the experimental setup into 3 distinct zones.
The first is called the excitation region and lays between the first and the second electrode. Here a fraction of the metastable helium atoms is photoexcited to Rydberg np states with a tunable pulsed uv laser. The laser beam is applied at a right angle to the atomic beam. Using a microwave horn antenna pointing into the excitation region, Rydberg atoms can be transferred to longer living ns states.
The second zone is the sample zone and lays between electrodes 2 and 3. In our case the sample is a 3D microwave cavity. The Rydberg atoms pass through a hole into the cavity, interact with the electric fields inside the cavity and leave the cavity through another hole at the back.
The third zone is the detection zone and starts with electrode 3. By applying a pulsed potential difference between electrodes 3 and 4 or 4 and 5, the Rydberg atoms can be field ionized. The resulting electrons are accelerated towards a micro channel plate (MCP) detector, where their image on a phosphor screen is recorded by a CCD camera and the total signal is displayed on an oscilloscope. The signal from the oscilloscope can be accessed via a LabView program on the computer.

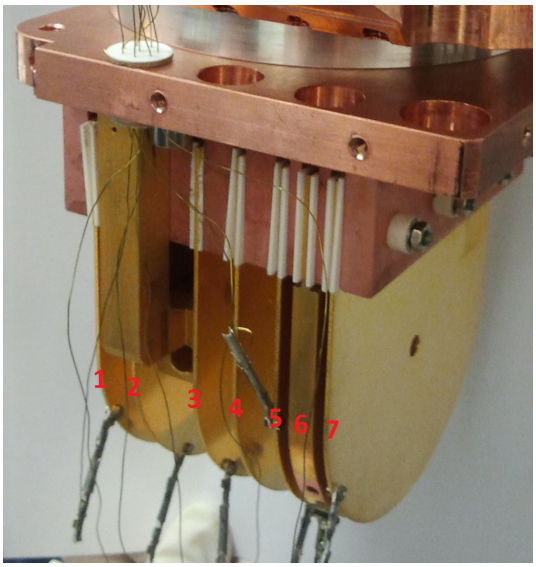

Figure 3.3.: *Photograph of the electrode stack while it was still outside the setup.The numbers name the electrodes. Photograph by Tobias Thiele.*

3.1. The vacuum and cryogenic system

Vacuum system

The whole experiment is conducted in vacuum to prevent collisions with background gas atoms. The cryogenic chamber and the source chamber contain high-vacuum, whereas the experimental region contains ultra-high-vacuum. This is achieved by a Adixen ACP15 fore-vacuum pump that reduces the pressure from atmospheric pressure (10^3 mbar) to about 10^{-1} mbar and three Pfeiffer Vacuum Turbopumps for the three vacuum chambers. The Pfeiffer vacuum pumps require a pressure of less than 5 mbar to work.

In order to achieve a better vacuum in the experimental chamber, differential pumping between the source chamber and the experimental chamber as well as between the cryogenic chamber and the experimental chamber is used. In this way a pressure of $3 \cdot 10^{-8}$ mbar at room temperature can be achieved in the experimental chamber. The steady-state pressure in the source chamber is $2 \cdot 10^{-7}$ mbar and rises to about 10^{-5} mbar when the pulsed valve is operated. The pressure in the experimental chamber rises slightly when the pulsed valve is turned on - to about $5 \cdot 10^{-8}$ mbar on average.

Cryogenic system

A pulse tube cooler Cryomech PT415RM is used to cool the sample down to about 3 K. It operates in a two stage configuration, where the first stage is held at about 30 K and the second stage at 3 K (see Figures 3.1 and 3.2). The pulse-tube cooler requires a helium compressor and works like a Stirling heat pump. Further information on pulse-tube refrigeration is available in Ref. [54].

One problem that arises during the cool down and at low temperatures is the adsorption of residual gas onto the surfaces and the resulting build-up of stray fields. Two measures were introduced to minimize this effect. First, helium-4 was chosen for the atomic beam because it is not easily polarized as a noble gas and therefore hardly interacts with the surfaces. Secondly, a procedure was developed to avoid the adsorption of residual gas onto the surfaces in the experimental chamber [28]. The main idea is to force the residual gas to predominantly adsorb at the first stage and not on the sample. The setup was therefore designed such that gas diffusing into the vacuum chambers first collides with a cold surface before it can reach the experimental chamber. Further on, the cool down process was optimized by monitoring the partial pressures of the relevant gaseous species H_2O, CO_2, N_2 and O_2. The partial pressures are measured with a residual gas analyzer (RGA). The temperature is held above the adsorption temperature of the different gaseous components as long as these have partial pressures above $5 \cdot 10^{-10}$ mbar. This is done with a heater mounted on top of the sample holder. With this technique the gases predominantly adsorb onto the first cooling stage.

3.2. The supersonic atom beam

The supersonic atom beam is generated by a pulsed valve that opens for 190 μs with a repetition rate of 25 Hz. Inside the reservoir the velocity v is given by the Maxwell-Boltzmann distribution

$$P(v) \propto v^2 \exp\left(\frac{-mv^2}{2K_B T}\right). \tag{3.1}$$

When the valve is opened, about 10^{18} ground-state helium atoms exit through the orifice [28], collide with each other and thus thermalize. The gas expands adiabatically and the velocity of the particles increases. In the region called the zone of silence, the dynamics can be described linearly, while the outer zone shows turbulent flow dynamics. As we want a beam with a low spread in the velocity distribution, two skimmers are placed in the beam path. The first skimmer with a diameter of 1 mm selects a small part from the zone of silence with a low forward velocity spread. The transverse velocity spread $\Delta v_\perp$ is limited by the geometrical placement of the skimmers, whose entrance holes are 60 mm apart. The second skimmer has a diameter of 1.5 mm, which gives a relative transverse velocity spread of 2.08 %:

$$\frac{\Delta v_\perp}{v} = \frac{(1+1.5)/2}{60} = 2.08\%. \tag{3.2}$$

The temperature of the atoms T and the spread in velocity are linked by equalizing the kinetic and the thermal energies

$$\frac{1}{2} m (\Delta v)^2 = k_B T. \tag{3.3}$$

In this way we can a achieve a beam with a low temperature. The velocity of the beam after the skimmer lays between 1700 m/s and 1800 m/s and will be measured in the experiments described later.

3.3. Excitation of atoms to Rydberg states

Metastable helium

The first step of the excitation of the ground state helium atoms to Rydberg atoms takes place 2 mm after the opening of the valve where a pulsed electric discharge excites the helium atoms to the metastable $(1s)^1 (2s)^1 \ {}^1S_0$ state. Like in a lightening, the discharge is ignited by a potential difference. The required potential difference for the discharge is lowered to 280 V by a hot tungsten filament and is applied for 30 μs. The discharge is necessary to overcome the very strong binding energy of the ground state helium atoms, which corresponds to light in the xuv range. For the metastable state a laser in the uv range suffices to transfer the electron to a Rydberg state.

Laser excitation

In the second step Rydberg states are produced by laser excitation of the metastable $(1s)^1\,(2s)^1\ {}^1S_0$ state to the singlet np Rydberg state. The singlet p state is chosen due to the restrictions given by optical selection rules. The n state depends on the frequency of the laser and ranges in our case from n = 30 to infinity; however, we can not resolve or excite pure n state for n above 60.

The laser system used to create the photo excitation of the Rydberg states consists of two lasers. The first is a pulsed green Nd:YAG laser from Innolas with 300 mJ pulses of 10 ns length. It is controlled by a computer solely running the control software of the laser. The first laser pumps the dye laser, which contains a red liquid solution (rhodamine) as the laser medium. The dye is excited by the first laser and fluoresces. The advantage of a dye laser is that it can be used over a wide range of wavelengths. For our spectroscopy measurements the wavelength of the dye laser is usually varied from 624.3 to 627 nm starting at the longer wavelength. This variation is achieved by changing the length of the Fabry-Pérot laser cavity. A small fraction is branched off in order to measure the wavelength with a wavelength meter. Next, the laser pulse is frequency doubled in a crystal to a wavelength of around 313 nm, focused with lenses and guided through a window in the setup to the excitation region between the first two electrodes. With the last two mirrors the position of the laser beam can be varied and the signal maximized. For this procedure the state n = 40 with a wavelength of 312.6815 nm is used, as it gives the signal with the highest magnitude. For the experiments with the cavity, the state n = 37 with a wavelength of 313.003 nm is relevant.

S-pulse

In the third step the Rydberg atoms are transferred from the short-lived np to the longer-living ns state (see section 2.1.3 for the lifetimes). For Rydberg spectrum measurements this step is left away, because a long lifetime is not necessary as the states are not further manipulated before they are field-ionized and recorded. The frequencies of the transitions between np and ns for n= 30 - 40 lie in the convenient range between 15 and 42 GHz. Using a microwave horn antenna mounted directly in front of the window where the laser beam enters, we can coherently transfer the Rydberg state population from the p to the s state. The microwave pulse is applied shortly after the laser pulse. The optimal starting point and duration are identified in the alignment measurements before every experiment set (see section 4.2). The atoms are now prepared in the ns state and can be manipulated with pulses applied to the 3D microwave cavity.

3.4. The 3D microwave cavity

In the experiments described in this Master's thesis we use a rectangular 3D cavity that consists of two almost symmetric halves. Each half is a OFHC copper block with the dimensions 52

mm x 26 mm x 5.5 mm (compare with Figure 3.4, 3.5 and 3.6). Inside each half a rectangular cavity is milled out. The cavity was produced with a length a = 42.8 mm, a height b = 6 mm and a depth d = 8 mm. Due to manufacturing constraints, the cavity is not fully rectangular, but round. The radius of curvature is 3 mm, which decreases the volume of the cavity and increases the resonance frequency of the modes slightly.

The two cavity halves can be screwed together using three screws. There are 2 small alignment holes through which two stainless steel rodes can be pushed to align the two cavity halves such that there is no kink at the interface.

The atomic beam passes through hole 1 in Figure 3.4. The hole has a diameter of 3 mm and a length of 1.5 mm and was altered twice, which will be described in more detail later.

The microwave field inside the cavity is inserted by one of two microwave couplers consisting of a UT-85 cable with a center conductor that is freed on a length of 3 mm. The position of this antenna determines the overlap with the modes and the amount of external coupling. The microwave couplers are usually positioned symmetrically while the cavity is open and fixed in place with the pin holders (see Figure 3.6 and 3.8 (a)). The resonance frequency, the quality factor and the coupling can only be measured when the cavity is closed. If adjustments have to be made, the cavity has to be opened again.

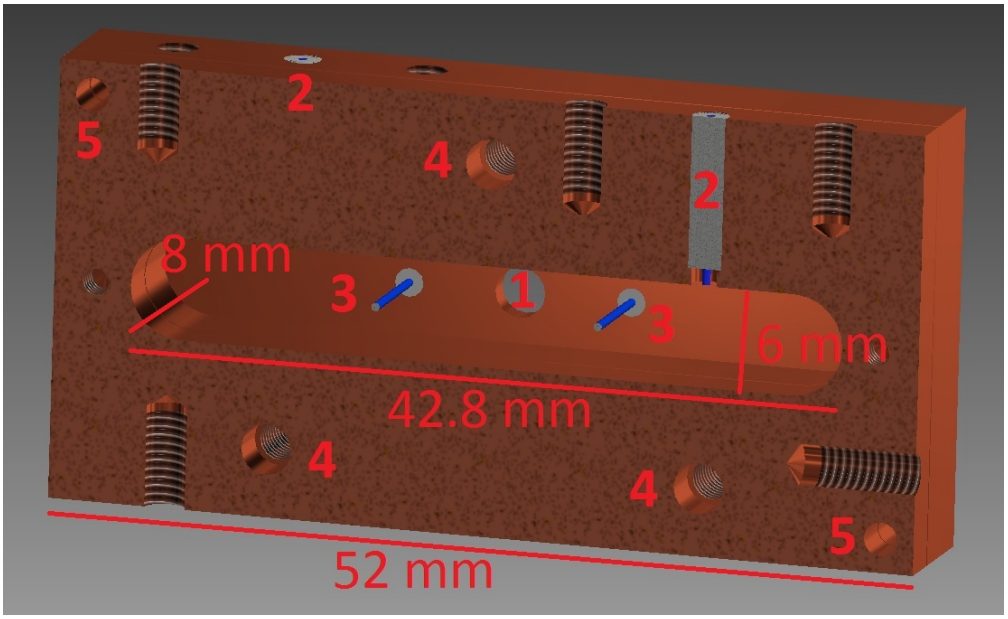

Figure 3.4.: *CAD design of cavity 4B. The outer dimensions of the two copper block are 52 mm × 26 mm × 5.5 mm. The dimensions of the cavity as first produced by the workshop are 42.8 mm × 6 mm × 8 mm. The atomic beam enters the cavity through hole (1). The modes inside the cavity are excited with the microwave couplers (2). An additional electric field can be applied with electrodes (3) that are 13.36 mm apart. The two cavity halves "front" and "back" can be screwed together using the holes (4). For this task the alignment holes (5) can be used.*

coupling pin

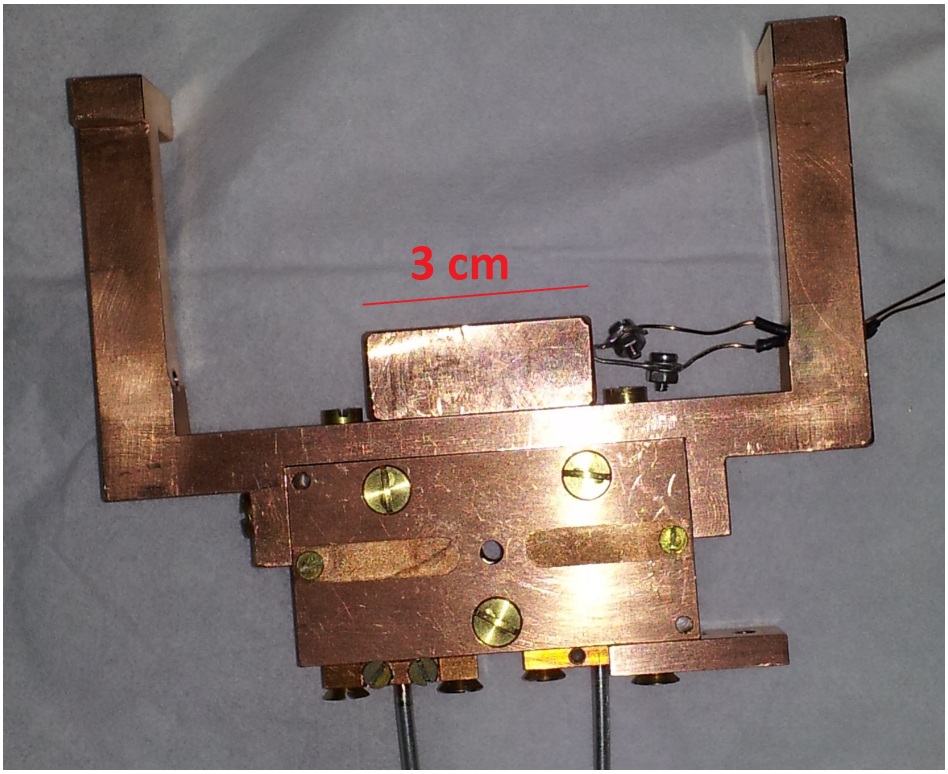

Figure 3.5.: *Photograph of the cavity front with the holder and the heater on top of the cavity. The shields for the electrodes can be seen to the left and the right of the atomic beam hole.*

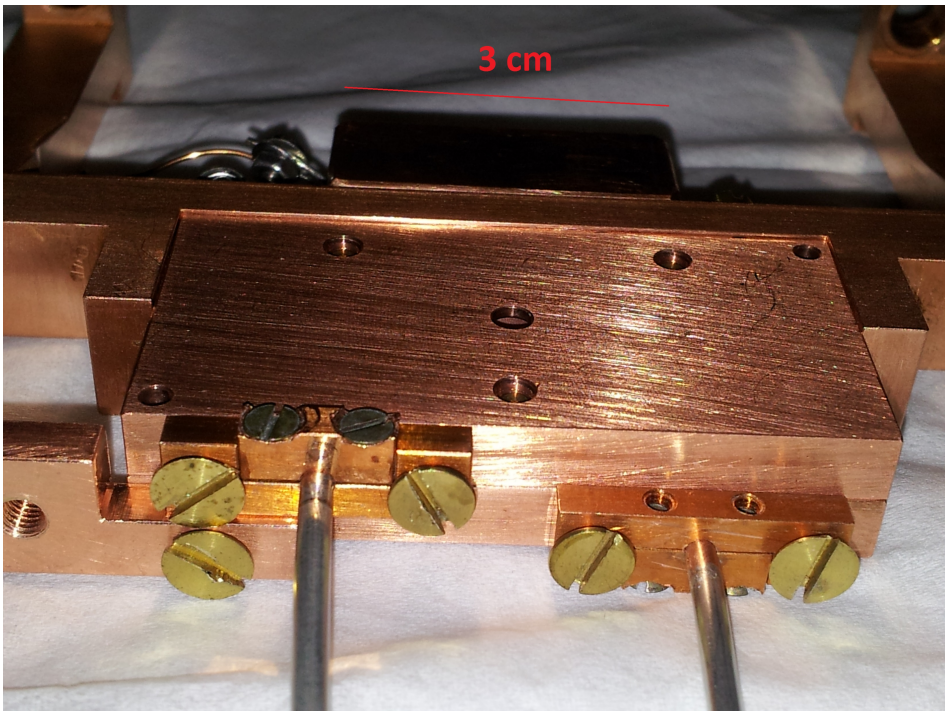

Figure 3.6.: *Photograph of the backside of the cavity with the microwave cables attached. Their position is fixed by the pin holders.*

With this cavity Rydberg atoms in the n = 37 state can be driven from the p to the s state and back by applying a microwave field inside the cavity. For this task the third mode (TE301) is used, which has 3 maxima in the electric field magnitude along the long side (see Figure 3.7). There is one maximum in the middle where the atom beam transits the cavity, meaning that the atoms can be manipulated with the field.

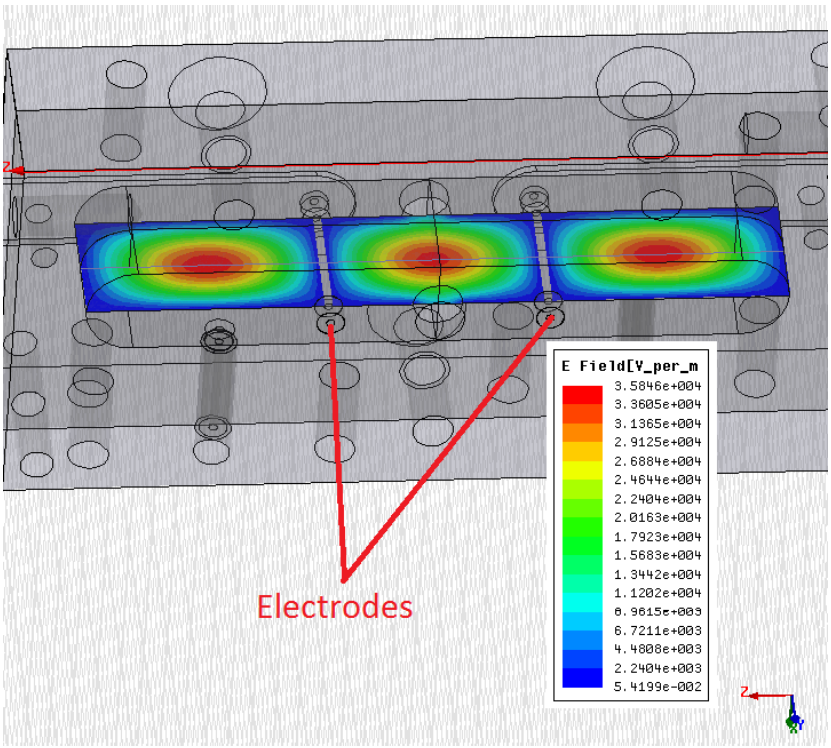

Figure 3.7.: *Simulation of the third mode with the electrodes in the minima. Red refers to high electric field magnitudes, blue to low ones. Simulation done by Mathias Stammeier.*

In the minima of the electric field, two electrodes are placed. They are separated by 13.36 mm. With these electrodes an additional electric field can be generated that influences the energy levels of the Rydberg atoms. Since the electrodes sit in the minima of the microwave field, the spectrum and the quality factor of the cavity are only slightly changed compared to leaving the electrodes away. This motivates the choice of the third mode.

The electrodes are made out of 0.6 mm thin steel wire as pictured in Figure 3.8 (b). One end is pressed into a PEEK cylinder for isolation and then inserted into an indentation in the cavity back (see Figure 3.8 (c). The other end is pressed into another cylinder and its tip soldered to a wire for connection to the voltage source. The opening in the cavity front is covered with a shield (see Figures 3.8 (d) and 3.5). The two cavity halves are almost identical except that the front has two indentations for the shield.

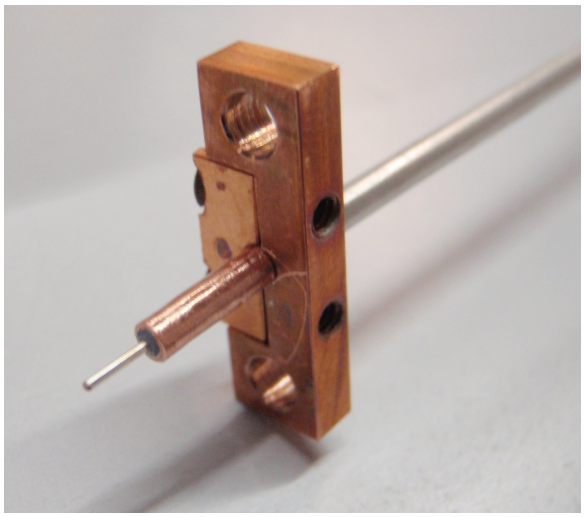

(a) *Photograph of the microwave coupler and its holder.*

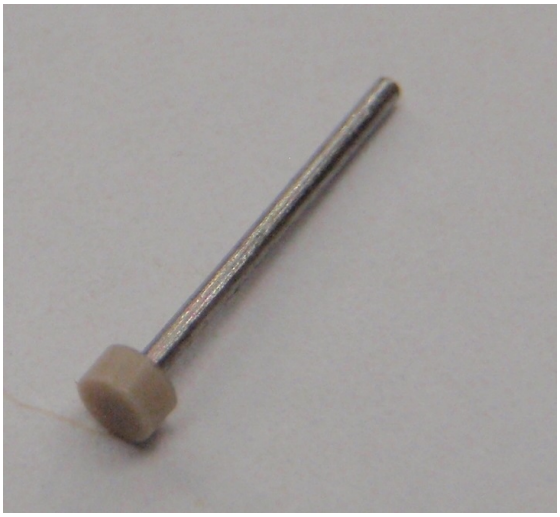

(b) *Photograph of the cavity-electrode with the PEEK isolation.*

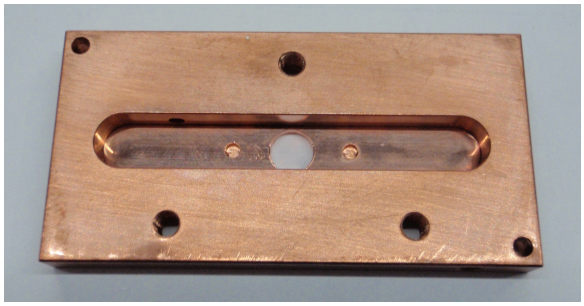

(c) *Photograph of the cavity back with the two indentations to the left and right of the atom beam hole for the PEEK tips of the electrodes (here cavity 4A, which has a bigger beam hole than 4B).*

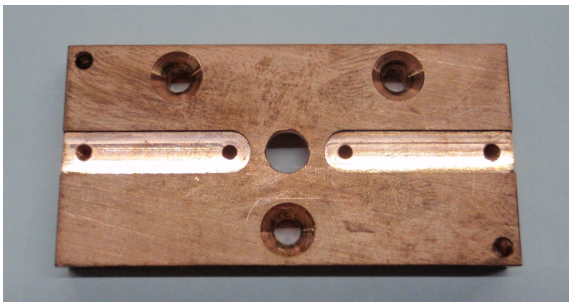

(d) *Photograph of the cavity front with the holes for the two electrodes and the indentations for the shields.*

Figure 3.8.: *Photographs of the microwave couplers, the electrode and the cavity halves with the holes for the electrodes.*

Changes to cavity 4B during the measurements

The cavity described above was used in the first experiments. Two kinds of changes were made to the cavity in the course of this master's thesis. First, the cavity was tuned to be resonant at a slightly different frequency. By grinding of the top layer of the copper block, the height d can be decreased, whereas it can be increased by grinding of a layer inside the cavity. In this way the resonance frequency and thus the detuning can be adjusted. This kind of tuning was done after the first and the second set of measurements and the resulting resonance frequencies and detunings are discussed in section 4.1.

The second kind of change concerned the shape of the holes through which the Rydberg atoms enter and leave the cavity. Sharp metallic edges lead to increased stray electric fields, which can influence the Rydberg atoms [55]. The cavity holes were therefore rounded on the inside of the cavity by a fillet of 0.7 mm radius. The next set of measurements however did not show

less stray fields and we then decided to replace the fillet with a chamfer of 0.8 mm vertical and horizontal length. The fillet was created in the workshop by cutting the rounding stepwise and increasing the radius with every step. This can mean that on the microscopic scale the edges did not disappear but were actually multiplied to many smaller edges. The chamfer on the contrary only has two edges. The advantage of a chamfer compared to the bare hole is that the atoms are further away from the metal on the inside of the cavity. The fillet was cut on the 8th of May and the following measurements were called 'fillet'. The chamfer was made on the 13th of June and is part of the final configuration of cavity 4B.

3.5. Detection of the Rydberg atoms with an MCP detector

The Rydberg atoms are field ionized by applying an electric field either between the electrodes 3 and 4 or 4 and 5 depending on how much of the p-state signal we want to record. The electric field is generated in a 10 ns pulsed potential difference of -1.2 kV between the two electrodes separated by 1 cm. Since the ionization field for a Rydberg atom depends on the quantum numbers, applying different ionization fields would also allow us to determine the states of the atoms.
After the ionization of the Rydberg atoms, the generated electrons hit the micro channel plate (MCP), which multiplies the low incoming signal to a detectable one and accelerates the emerging electrons towards a phosphor screen at the back of the MCP by a potential difference. The phosphor screen generates a fluorescence signal when a particle arrives. The signal is recorded by a CCD camera. With this setup we can get the spatial and the temporal distribution of the Rydberg atoms. The signal is then amplified and observed on an oscilloscope, which can be read out with our LabView software and stored in a data file for further manipulation.

MCP detector

The micro channel plate detector is a single particle detector that can detect Rydberg electrons and metastable atoms. In contrast to a normal electron multiplier, it can also give the spatial distribution. The device consists of three plates: the front and the back plate as well as the phosphor screen for the picture. The MCP contains a vast number of 10 μm diameter channels, which are tilted in an angle of 8 degrees for half the way and then tilted the other way for the rest of the path (see Figure 3.9 (A)). This insures that every incoming particle (B) hits the walls of the channel. The particle hitting the wall causes secondary emission of electrons (C). The electrons are accelerated down the tube and hit out more electrons causing an avalanche-like effect. Each initial particle knocks about 10^7 electrons out. The emerging electrons (D) are then accelerated towards the phosphor screen as described above.
The MCP only acts as an electron multiplier when a potential difference is applied between the front and the back plate. In our experiments we apply a voltage of 1.6 to 1.8 kV to the back plate. The gain of the MCP is higher for larger potential differences. To prolong the

lifespan of the MCP, a high voltage difference between the front and the back plate is usually only applied when the Rydberg signal arrives. For time traces, a voltage of 2.5 kV is applied to the phosphor screen, while for Rydberg and metastable helium pictures, the voltage at the phosphor screen is increased to 4 kV and the duration of the MCP pulse increased to 106 μs instead of 6 μs. The camera shutter opens for 20 μs for Rydberg pictures and 200 μs for He*. For the metastable helium the voltage at the back plate can be lower: about 1.6 kV.

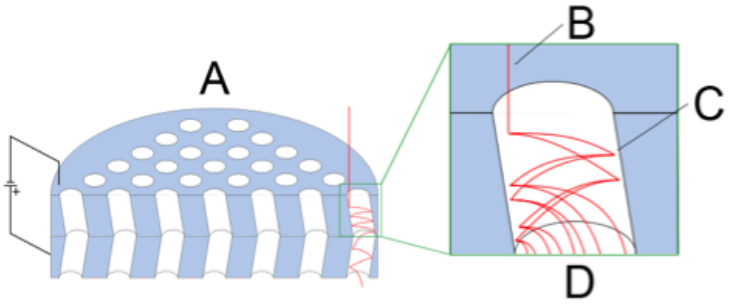

Figure 3.9.: *Schematic of the MCP (A). The incoming electron enters one of the micro channels (B) and hits the wall of the channel causing secondary emission of electrons (C). The electron cloud leaves the channel and is accelerated towards the phosphor screen (D). Figure from [56].*

4. Measurement results for cavity 4B

In this chapter the measurements with cavity 4B are described and the results presented and discussed. During this master's thesis 5 measurement sets were made and named after the cavity configurations described in section 3.4. An overview over the measurement sets is given in Table 4.1. We start with the measurement of the resonance spectrum of the cavity with a network analyzer (section 4.1) and continue with the initialization of the Rydberg measurements in section 4.2. We explain the alignment and optimization of the pulses and measure the velocity of the Rydberg atoms and the excitation spectrum. In section 4.3 one of the main experiments is described: we drive Rabi oscillations with the microwave cavity and determine the modefunction along the beam axis as well as the Stark shifts caused by stray fields. In section 4.4 we insert the electrodes and show that we can control the DC Stark shift. From the Stark shift measurements we can find the electric field caused by the electrodes along the beam axis and the stray field. In the last section (4.5), the measurement results from different measurement sets are compared.

Measurement sets

#	Name	Date	Folder	Temperature	Quality factor
1	"first"	24.04 - 04.05	20140504	300 K	84
2	"fillet"	03.06 - 17.06	20140617	300 K	1004
3	"chamfer 300 K"	18.06 - 23.06	20140623	300 K	180
4	"chamfer 4 K"	24.06 - 27.06	20140627	4 K	(warm: 180)
5	"electrodes"	29.06 - 01.07	20140701	300 K	143

Table 4.1.: *Overview of the measurements conducted during the thesis.*

4.1. Resonance spectrum of the cavity

In the beginning of each measurement set, the resonance spectrum of the cavity should be determined. In this way it becomes clear if the atoms with zero-field transition frequency $\nu_0 = 21.5299$ GHz for the 37p $\leftrightarrow$ 37s transition can be manipulated with the cavity. The resonance spectrum is obtained in a two port measurement with a calibrated network analyzer measuring the transmission curve S_{21}. Light is coupled into the cavity with the same microwave coupling cable as in the experiments. The attenuation of the coupling cable is subtracted from the measured S_{21} parameter as is the attenuation of other cables used.
For each of the four first modes we calculate the resonance frequency ν, the width $\delta\nu$ (FWHM), the quality factor Q, the internal quality factor Q_{int}, the external quality factor Q_{ext} and the

		Mode 3					
#	Name	ν [GHz]	Δ [MHz]	$\delta\nu$ [MHz]	Q	Q_{int}	Q_{ext}
1	"first"	21.237	293	253	84	211	139
2	"fillet"	21.515	15	21	1004	5940	1210
3	"chamfer 300 K"	21.383	147	119	180	682	245
5	"electrodes"	21.381	149	149	143	1373	160

Table 4.2.: *Resonance frequencies, cavity detunings, resonance width and quality factors of the third mode for the different measurement sets.*

insertion loss IL by fitting a Lorentzian line shape to the measured resonance as described in section 2.2.2. The result for the "electrodes" measurement set can be seen in Figure 4.1. The calculated values vary a lot depending on which mode is observed. As discussed in section 3.4, we are mostly interested in the third mode, with which we drive the transitions between the s and the p state. For this mode the results are summarized in Table 4.2. The cavity detuning Δ from the zero-field transition frequency ν_0 given by $\Delta = \nu_0 - \nu$ is also listed.

Resonance frequency and cavity detuning

The resonance frequency of the cavity shifts by around 10 MHz when it is measured in vacuum instead of air. This shift to higher frequencies in vacuum is due to the slightly higher permittivity of air compared to vacuum and can be calculated using formula (2.34). Since the experiment is conducted in vacuum, the cavity resonance spectrum should be measured in vacuum in order to get the relevant frequencies.

The cavity detuning describes how close to the cavity resonance the transition between the s and the p state is. In the first measurement set, we were quite far away from the transition with 293 MHz cavity detuning. We then tuned the cavity closer to the transition frequency ($\Delta = 15$ MHz) by decreasing the depth d of the cavity through abrasion. The measurement results with that cavity detuning showed large stray fields and we therefore decided to get rid of the fillet. The resulting cavity has a detuning around 150 MHz.

Width and quality factor

The width $\delta\nu$ of the resonance and thus the quality factor Q can be adjusted by changing the length the coupling pins stick into the cavity as described in section 3.4. For all the measurement sets except the "fillet" measurement, a large width of 140 MHz to 300 MHz for the third mode was chosen. This resulted in a low quality factor Q, which was below 200. For the "fillet" measurement it was about 1000 - more than 5 times as high. The two resonance curves can be compared in Figure 4.2. The shape is the same, but the "fillet" curve spans a smaller frequency range. A cavity with a high quality factor Q has a narrower resonance and the frequency of the mode has to match more accurately with the atomic transition frequency than for a low Q cavity. We can drive the atomic transition with all the chosen

cavity configurations as the cavity detuning Δ is never much higher than the width $\delta\nu$ of the resonance peak.

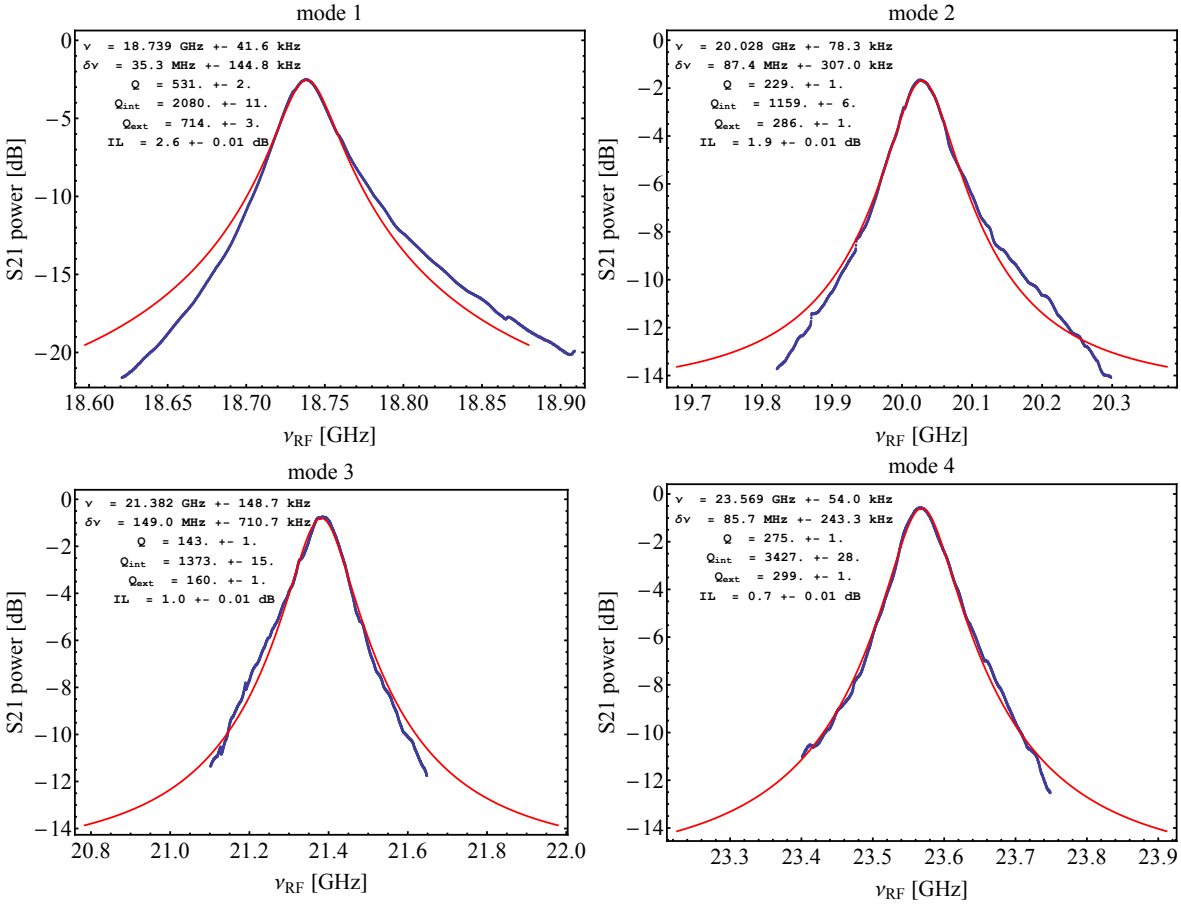

Figure 4.1.: *Resonance curves of the 4 lowest cavity modes for the measurement set "electrodes". The blue points were measured, the red line is the Lorentzian fit done by Mathematica. The resonance frequency ν, the width $\delta\nu$ (FWHM), the quality factor Q, the internal quality factor Q_{int}, the external quality factor Q_{ext} and the insertion loss IL are given in the figure for each mode.*

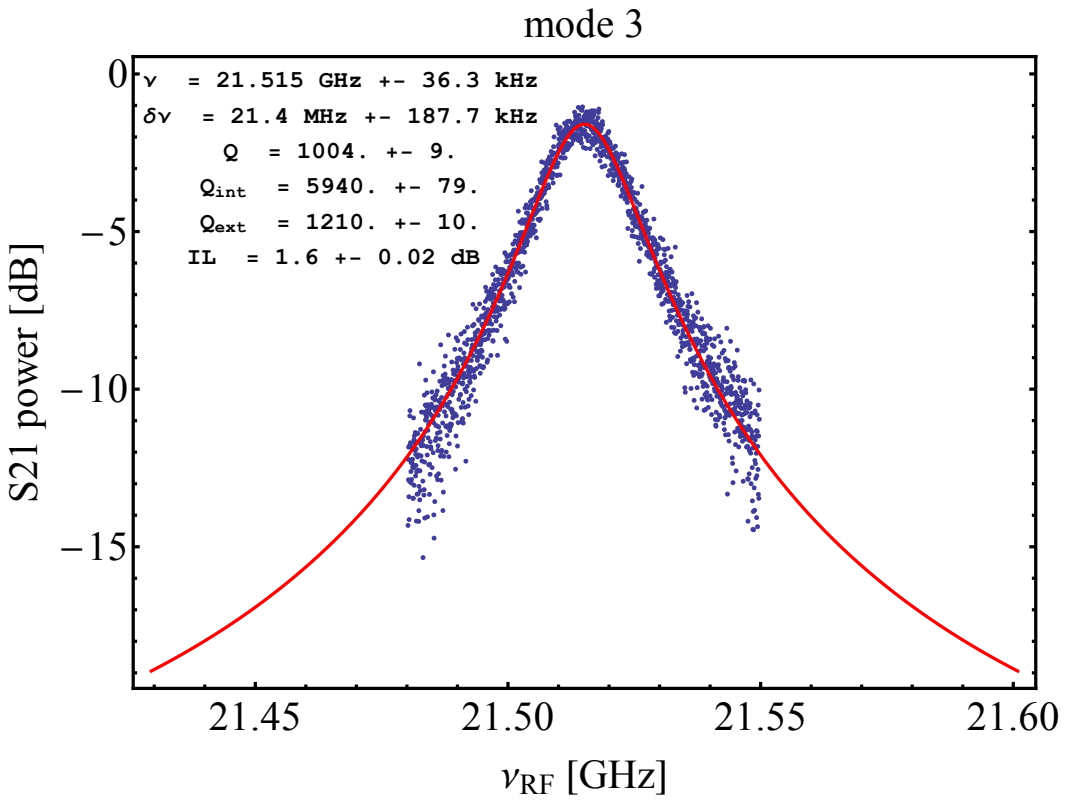

(a) *Measurement set: "Fillet"*

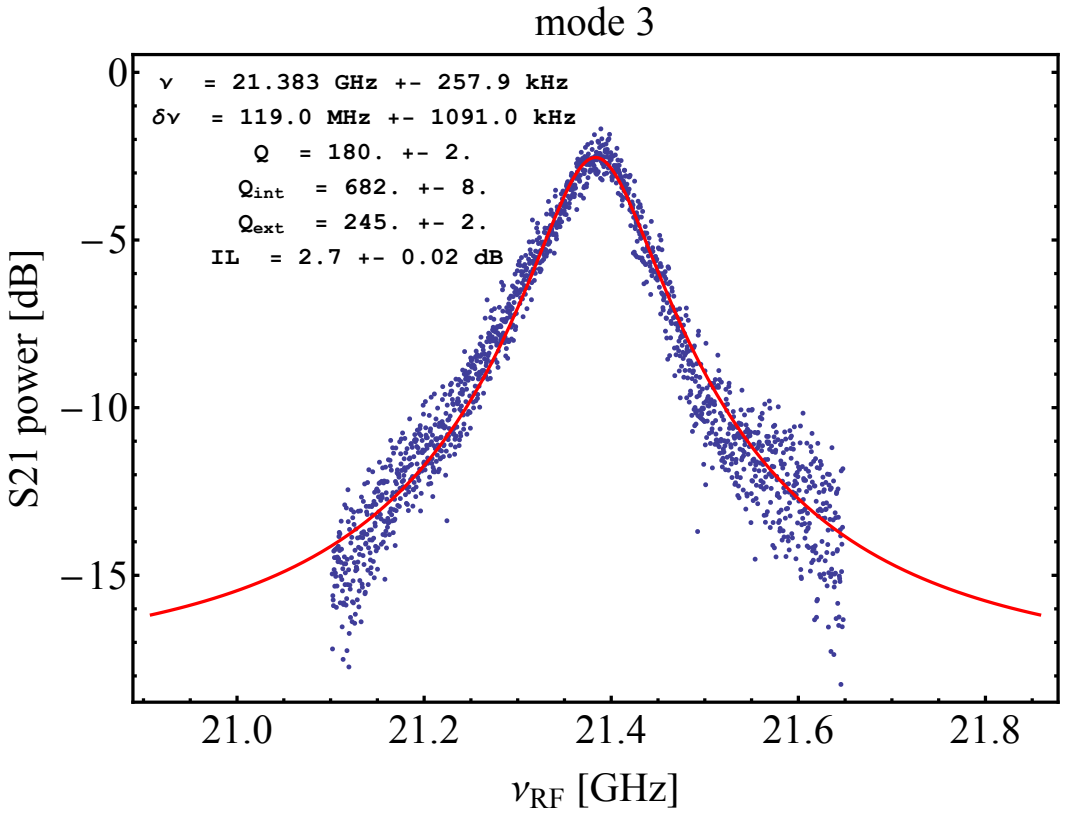

(b) *Measurement set: "Chamfer 300 K"*

Figure 4.2.: *Comparision of the resonance spectrum of the third mode for two different measurement sets.*

4.2. Initialization: alignment and optimization of the pulses

After building in the microwave cavity into the opened setup, the holes for the atom beam have to be aligned and the setup closed and fixed in place with screws. The setup is then evacuated and if desired cooled down. The Rydberg atom measurements are initialized by switching on the required measurement equipment. The procedure is the following:

1. The Dye-laser with its pump and water cooling cycle is switched on.
2. The Nd-YAG laser with its pump source and shutter is started on the computer.
3. The helium gas bottle is opened and vented.
4. The discharge is initiated by applying a voltage of 280 V and a current of 5.3 A, creating metastable helium atoms.
5. We wait for the pressure in the source chamber to stabilize around $\approx 3.8 \cdot 10^{-5}$ mBar.

Pulses and their triggers

The sources triggering the pulses are never turned off, but some settings have to be adjusted to get a good signal. The most important pulse triggers and their settings are (see also the schematic in Figure 4.3 as a guide):

1. The pulsed valve, which opens at $t = 0$ for 190 μs.
2. The HV-discharge triggered between 400 and 550 μs after the opening of the valve for 30 μs. The delay of the discharge is optimized in the velocity measurement.
3. The laser, which excites Rydberg atoms with a delay of 80 to 110 μs after the beginning of the discharge. This pulse is also optimized in the velocity measurement.
4. The first microwave pulse, called the s-pulse as it transfers Rydberg atoms from the p to the s state, is optimized in the s-pulse optimization procedure. The optimal starting point is usually at the same time as the laser pulse and the optimal length around 200 to 300 ns.
5. The second microwave pulse, which is applied inside the cavity and thus called the cavity pulse, is applied after a specific delay that defines the position of the Rydberg atoms inside the cavity at that instant. The atoms are inside the cavity for delays of around 4 to 9 μs. The length of the pulse depends on the measurement and is chosen between 20 ns to 400 ns.
6. The extraction trigger delay depends on which two electrodes are used. If the voltage difference is applied between the third and the forth electrode, the delay is around 13 μs. If the forth and the fifth electrode are used, the delay is 6 μs longer.

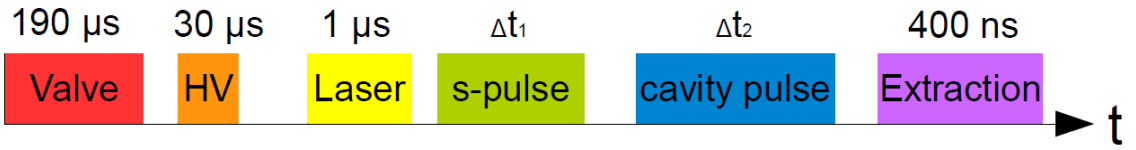

Figure 4.3.: *Pulse scheme for the experiment. The time above the colored box gives the length of the pulse. The length Δt_1 of the s-pulse lays between 200 and 300 ns. The length Δt_2 of the cavity pulse is usually chosen between 20 and 400 ns.*

4.2.1. Metastable Helium and Rydberg picture

Metastable helium picture

After starting up the experimental setup, we first check if we get a good signal from the metastable helium atom beam. The laser beam is blocked in the meantime, meaning that no Rydberg atoms are excited. The photograph is taken with the CCD camera imaging the phosphor screen as described in section 3.5. The picture is then exported to Mathematica and the height and the width of the beam can be analyzed.

The alignment of the setup is judged by the shape of the metastable helium signal on the picture. The atomic beam passes through the holes (skimmer, electrodes) nicely when the signal is round and symmetric like in Figure 4.4 from the 4th of May. If the holes are not aligned, the beam is deformed. This was for example the case after the cool down; the setup got distorted (see Figure 4.5). The alignment of the setup can be adjusted with screws that fix the position of the pulse tube refrigerator's cold head on top of the setup. The inner part of the setup, however, can also be turned with respect to the outer part. Its alignment can only be changed while the setup is open. In the course of the measurements a good position was found by turning the setup and investigating the result. This position has been marked with two red lines and now we can position the setup the same way every time.

The extent of the beam can also be obtained from the pictures. If the beam is well aligned and not confined with the razor blades, the height is around 1.2 mm. With the razor blades the lower and the upper part of the beam can be limited to a certain size. The atoms in the outer region of the beam have a higher velocity dispersion compared to the inner atoms and interact more with the surfaces as they are closer. In the cavity measurements the razor blades were usually not closed as there is some natural confinement due to the cavity beam holes.

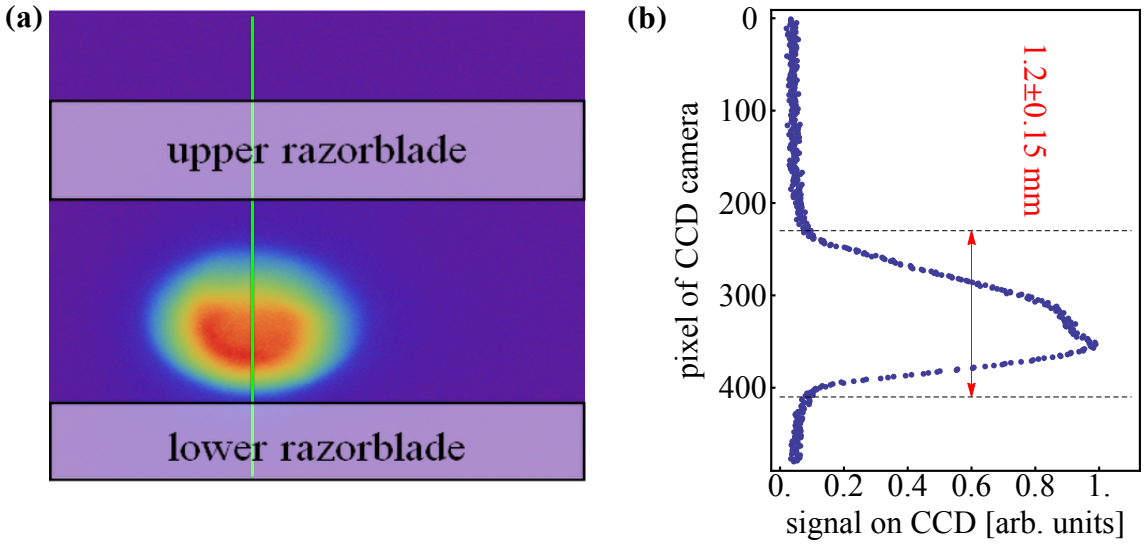

Figure 4.4.: *Metastable helium picture from the 4. May 2014. In (a) the symmetric beam shape can be seen. The two razorblades are open and do not confine the beam. In (b) the signal on the CCD along the green line in (a) can be seen. The green line is placed at the maximal signal intensity. The beam is 1.2 mm high.*

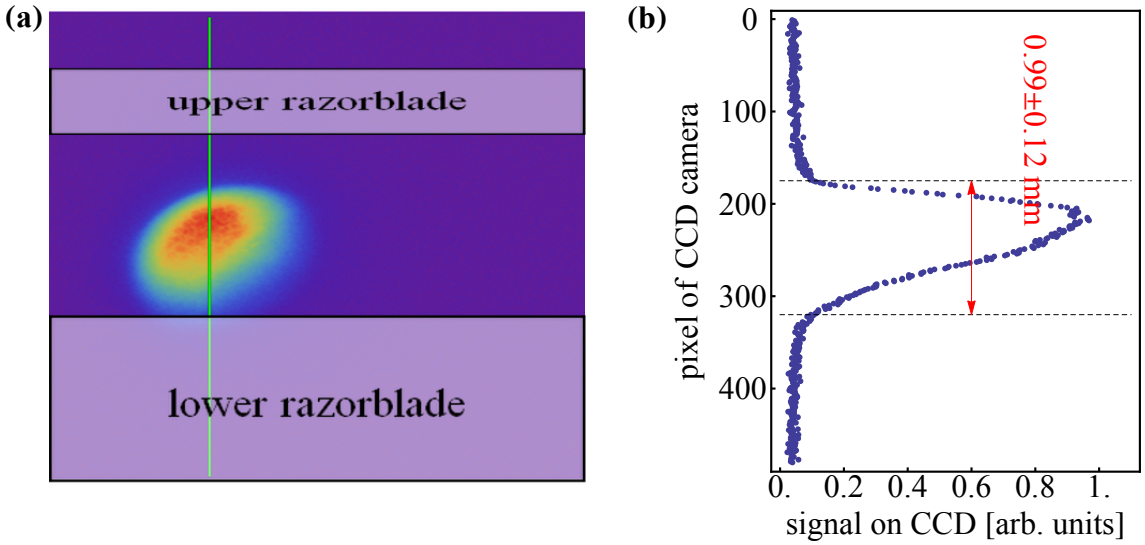

Figure 4.5.: *Metastable helium picture from the 24. June 2014. In (a) the deformed beam can be seen. The two razorblades are open and do not confine the beam. In (b) the signal on the CCD along the green line in (a) can be seen. The beam is about 1 mm high.*

Rydberg picture

It makes sense to check that the Rydberg atom beam hits the MCP right after taking a helium picture. This is done by unblocking the laser, optimizing the signal on the oscilloscope and taking a picture with adjusted camera settings (see section 3.5). For the optimization we examine the strength of the Rydberg signal on the oscilloscope when exciting the atoms with a wavelength of 312.6815 nm (dye-laser: 625.363 nm - before frequency-doubling), where the signal is usually strongest. The signal can be altered by changing the laser delay or the position of the laser entering the window. In Figure 4.6 Rydberg pictures for 3 different wavelengths of the laser excitation are shown (along with the metastable helium picture for comparison). For us it is essential that the Rydberg beam hits the MCP at a wavelength of 313.003 nm. As another check point we take 312.25 nm, for which we excite more then one high n state. The deflection of the atoms by a magnetic field is state dependent. Higher n state Rydberg atoms get deflected more than lower ones. With the magnetic field compensation turned on, high n state Rydberg atoms hit the MCP at the same position as the low n state atoms, meaning that the magnetic field experienced by the atoms is zero.

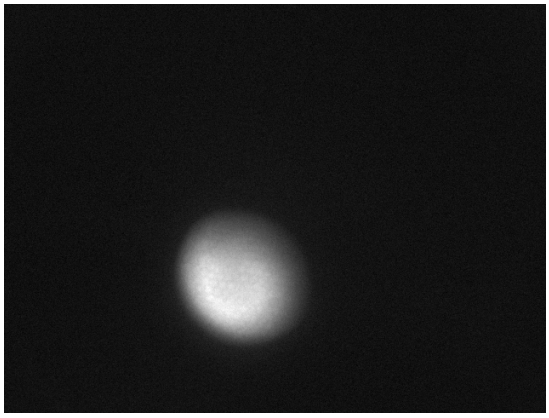

(a) *Metastable helium picture*

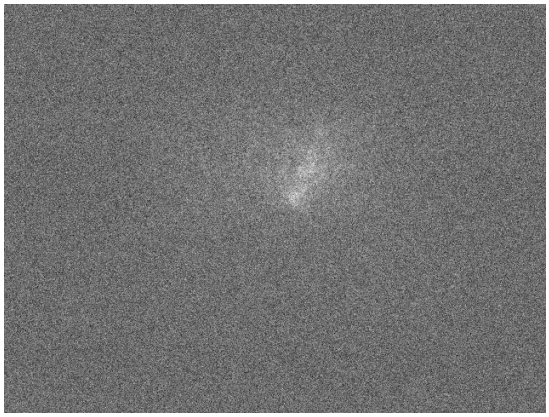

(b) *Rydberg picture for λ = 313.003 nm*

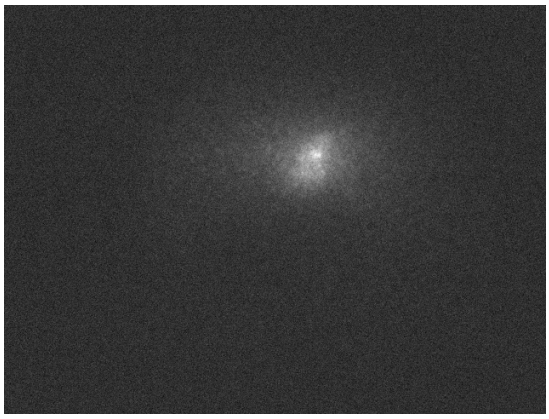

(c) *Rydberg picture for λ = 312.6815 nm*

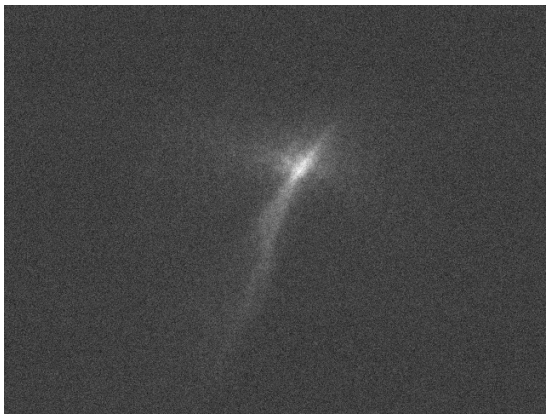

(d) *Rydberg picture for λ = 312.25 nm*

Figure 4.6.: *Photographs of the metastable helium and Rydberg atom signal. The metastable helium picture is given for comparison. The Rydberg signal stays at the same position for different wavelengths and the corresponding states.*

4.2.2. Velocity measurement

The velocity measurement allows us to determine the velocity of the Rydberg atoms and width of the atom packet along the beam direction. In the measurement we vary two parameters: the delay of the HV discharge (with respect to the opening of the valve) and the delay of the laser with respect to the beginning of the discharge. The discharge delay is varied between 350 and 620 μs, the laser delay between 50 and 135 μs. For each combination the integrated signal strength is measured and then plotted in a two dimensional graph as in Figure 4.7 at the top. A cut through the plot with constant discharge delay shows the distribution of the times the atoms need to travel from the discharge to the place where they get excited by the laser. This distance has a length l of 165 mm. The distribution is fitted with a Gaussian in Mathematica and the center t_1 as well as the width Δt_1 of the distribution is determined. We can now calculate the velocity of the center atoms:

$$v_{center} = \frac{l}{t_1}. \tag{4.1}$$

This can be done for all discharge delays. The width of the distributions and the velocities of the centers are plotted in Figure 4.7. The signal for discharge delays below 430 μs is very weak. Most of the atoms arrive at the discharge after a delay of 460 μs and this value is thus chosen for the measurements. The atoms in the front of the beam have a lower velocity and are less spread in velocity. For the measurement from the 20th of June displayed in the figure, the center of the metastable helium distribution for a discharge delay of 460 μs is at $t_1 = 93$ μs and this value was thus chosen for the laser delay. The velocity of the atoms there is 1783 m/s. The velocity measurements have been made for the last three measurement sets and the values summarized in Table 4.3 were obtained or chosen.

Velocity measurements

Date	Measurement set	HV delay [μs]	Laser delay [μs]	Velocity [m/s]
20.06.2014	"chamfer 300 K"	460	93	1783
26.06.2014	"chamfer 4 K"	460	97	1722
01.07.2014	"electrodes"	460	97	1727

Table 4.3.: *Velocity measurement: HV delay, laser delay and velocity for the 3 last measurement sets.*

Temperature of the atoms

The velocity dispersion Δv in beam direction and thus the temperature T of the atoms can be obtained by measuring a second time distribution of the atoms, for example at the extraction. In that case the delay of the extraction is varied instead of the delay of the laser excitation and we can get the width Δt_2 of the Gaussian fit to the time signal at the extraction. We can determine the velocity Δv with which the atoms move apart from the two widths Δt_1 and Δt_2 together with the times t_1 and t_2 when the pulse is applied to the the centers.

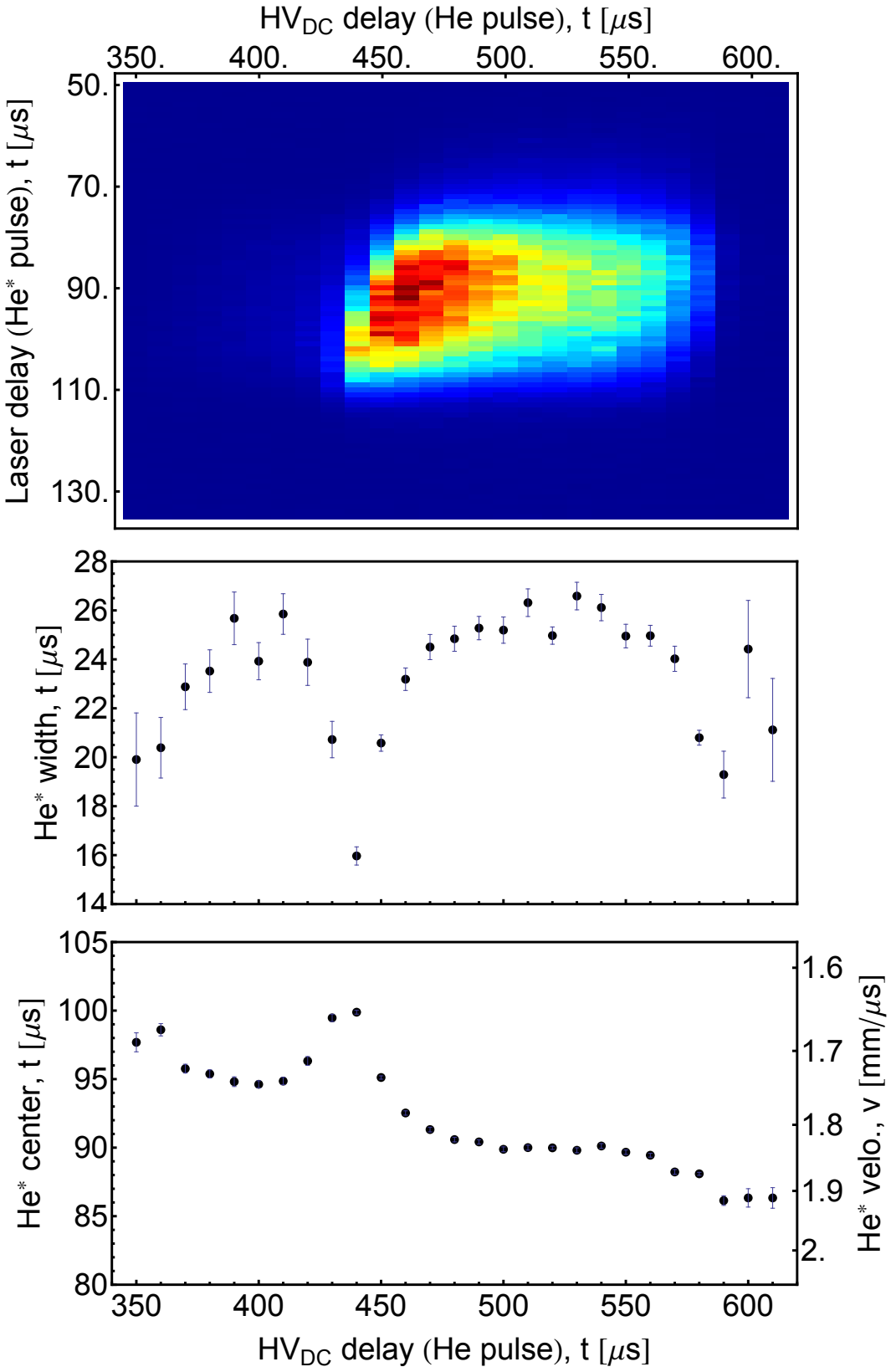

Figure 4.7.: *Velocity measurement.*

For the deviation we first move from distributions in time to distributions in space. At time $t_0 = 0$, when the atoms leave the valve, the atom packet has an unknown width σ_0. Since the atoms do not all move at the same speed, the atom packet gets wider. At the place where the atoms are excited with the laser, the distribution has a width σ_{s_1} and at the place where the atoms are extracted a width σ_{s_2}. These two widths can be estimated by multiplying the widths Δt_i of the time distributions with the mean velocity of the centers v. We assume that the mean velocity of the centers is constant in the measurement, the atoms simply move apart from each other by a constant value Δv, which is a lot smaller than v. The width of the Gaussian distribution at the laser excitation (i = 1) and the extraction (i = 2) can be calculated with the formula:

$$\sigma_{s_i}^2 = \sigma_0^2 + (\Delta v)^2 t_i^2 \approx (v \cdot (\Delta t_i))^2 \tag{4.2}$$

We can get rid of the unknown width σ_0 of the distribution at the valve by subtracting the equation for i = 1 in 4.2 from the one for i = 2:

$$\sigma_{s_2}^2 - \sigma_{s_1}^2 = (\Delta v)^2 \left(t_2^2 - t_1^2\right) \approx v^2 \left[(\Delta t_2)^2 - (\Delta t_1)^2\right] \tag{4.3}$$

and then rearrange the equation for the velocities:

$$\frac{\Delta v}{v} \approx \sqrt{\frac{(\Delta t_2)^2 - (\Delta t_1)^2}{t_2^2 - t_1^2}}. \tag{4.4}$$

With this formula we can calculate the velocity the particles move apart with. The temperature of the atoms can then be calculated with formula 3.3 and lays in between 7 and 11 K for our measurements.

4.2.3. Rydberg spectrum

We now have all the settings to create a strong Rydberg atom signal and can take a Rydberg spectrum. The wavelength of the dye-laser is swept from 624.3 nm to 627 nm, meaning that we start with the higher n states and decrease the frequency until we reach n ≈ 23. In order to capture the integrated signal for all wavelengths correctly, the markers defining the area over which the signal is integrated should be set such that the Rydberg peak is covered for both low and high n states. The Rydberg atoms are ionized at the third electrode as most excited p-state Rydberg atoms would otherwise decay before they get ionized. If the laser power is too high, the peaks get power broadened making it harder to distinguish between the different peaks. A pulse energy of about 350 μJ has proven to be suitable.

A spectrum as displayed in the LabView program can be seen in Figure 4.8. The yellow, orange and blue lines corresponds to different marker sets. The yellow curve shows the highest signal and contrast and has the least background contributions and is therefore used for further

analysis.
The peaks for low n states on the right can be easily distinguished. The lowest n state in the figure corresponds to $n = 30$. The peak of the 37p $\leftrightarrow$ 37s transition lies at a dye-laser wavelength of 626.006 nm corresponding to a transition wavelength of 313.003 nm. Two effects determine the height of the peak. First, the lifetime τ is proportional to n^3 and thus the peaks with higher n to the left are taller. States with small n have already decayed when the atom arrives at the extraction electrode. Second, the cross section $\sigma \propto \langle r \rangle^2$ scales with n^{-3}, meaning that higher n states are less likely excited. For high enough frequencies the ionization threshold is reached and the signal drops to zero. The spectrum is a useful tool to determine the size of stray fields by monitoring the field-induced shift of the ionization threshold [28].

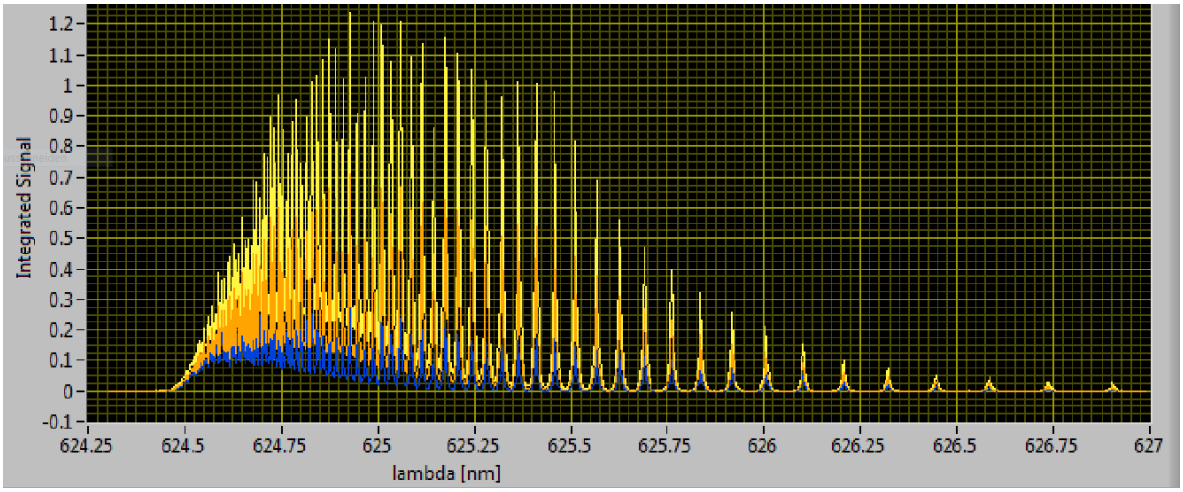

Figure 4.8.: *Rydberg spectrum from the 24. April 2014 as displayed in LabView. The dye-laser (before frequency doubling) emits the wavelength given on the x-axis. The different colors refer to different marker sets for the integrated signal.*

4.2.4. Optimization of the s-pulse

The last step before the cavity measurements is optimizing the microwave pulse that drives the Rydberg atoms from the short-lived p state to the long-lived s state. Four parameters can be adjusted: the delay with respect to the zero point of the second trigger, the length, the frequency and the power of the pulse. For the power a value of 22 dBm is chosen. The optimal values for the delay, duration and frequency are found iteratively. As a starting point the values from the last measurement are taken. In the first step the delay of the pulse is swept between 300 ns and 1.2 ns while the other two parameters kept constant. The curve (see Figure 4.9 (a)) shows a first Rabi peak at about 1 μs, which means that the s-pulse is applied almost simultaneously with the laser excitation. This maximum for the delay is then used in the second step in which the length of the pulse is varied. The peak in the signal is found for lengths between 150 ns and 300 ns (see Figure 4.9 (b)). In the third step the frequency of the s-pulse is optimized. The frequency is varied around the zero-field transition frequency ν_0. The resonance frequency is found with a fit (Gaussian or with function (2.61) in

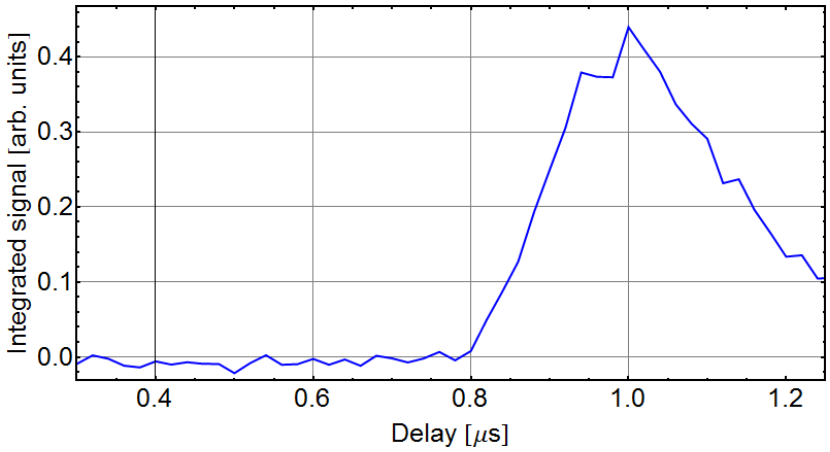

(a) *Optimization of the s-pulse delay. The maximum at 1 μs is chosen.*

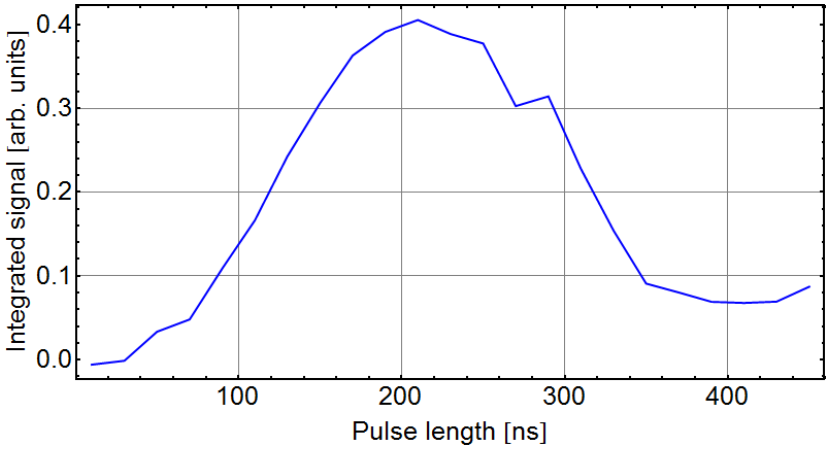

(b) *Optimization of the s-pulse length. The maximum of the Rabi oscillation at 210 ns is chosen.*

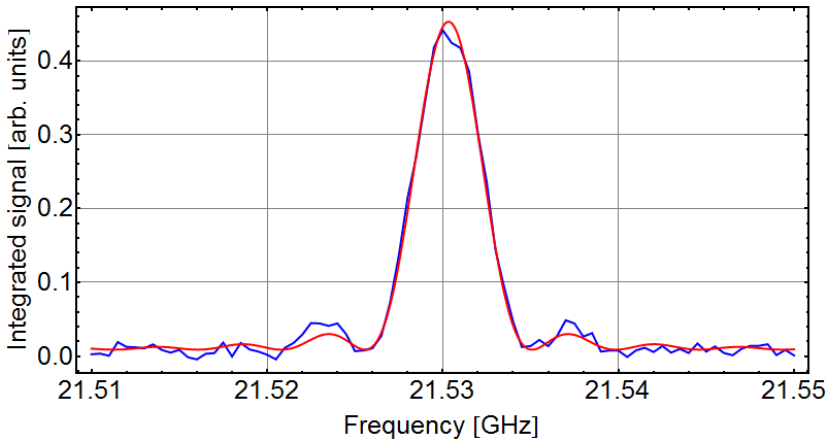

(c) *Optimization of the s-pulse frequency. The resonance frequency is found with a fit (red) of the data (blue) in Mathematica: 21.5303 GHz. The secondary maxima of the Rabi oscillation can be seen.*

Figure 4.9.: *The three different steps in the optimization of the s-pulse: delay, length and frequency.*

Mathematica. The secondary maxima to the right and left of the peak can be nicely seen in Figure 4.9 (c). Since the three parameters (delay, length and width) depend on each other, the three steps are repeated until the values converge.

4.3. Rabi oscillation measurements

After the alignment and optimization measurements, the first measurement characterizing the cavity can be done: we drive Rabi oscillations with the cavity field. The positions of the minima depend on the applied amplitude, the frequency, the duration and the delay of the pulse. In our measurements, the pulses have a constant duration. The delay of the cavity pulse defines at what position inside the cavity the atoms are exposed to the field. It is usually possible to drive Rabi oscillations at delays between 4.5 and 9 μs. The cavity is characterized by choosing a specific delay and studying the amplitude and frequency dependance of the Rabi oscillations for that delay. Then we move on to the next delay and repeat the procedure. The amplitude and frequency dependance of the Rabi oscillations can best be seen in a two dimensional map. On the x-axis we vary the amplitude of the microwave pulse. On the y-axis the frequency is swept. We can display the frequency ν as a shift from the field free transitions frequency ν_0. An example of such a two dimensional Rabi oscillation map is given in Figure 4.10. The color refers to the strength of the s state signal. In the red parts of the picture, the atoms are in the s state. In the blue parts, the atoms are driven to the p state.

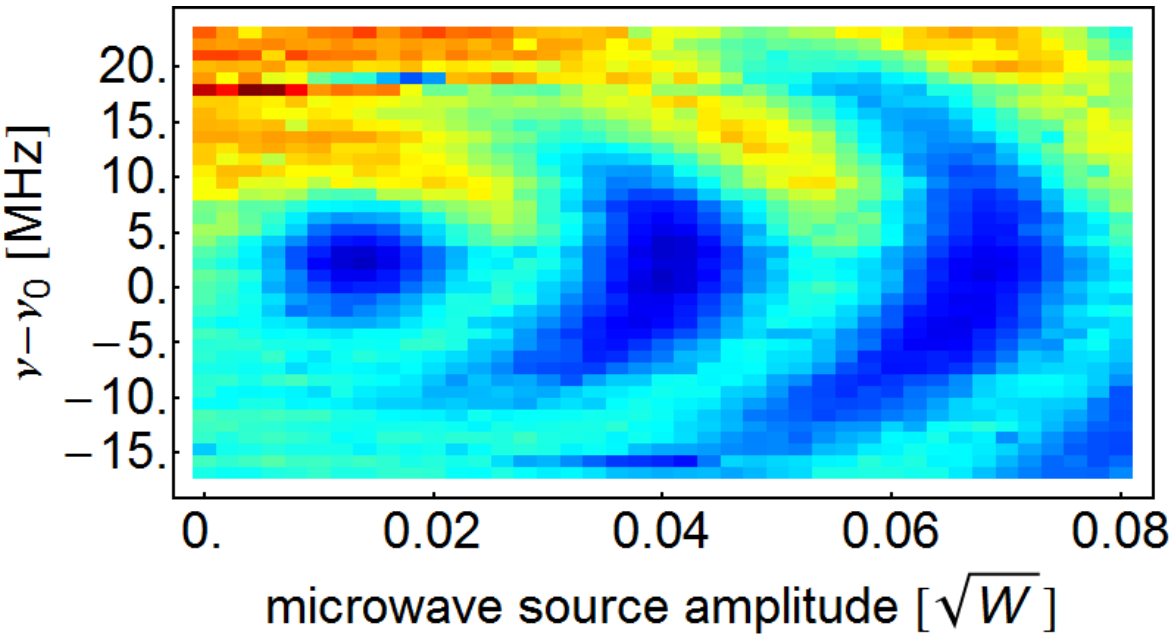

Figure 4.10.: *Two dimensional map of Rabi oscillations. The color code describes the fraction of atoms in the s state: for red the atoms are in the s state, for blue in the p state.*

One point catches the eye: for frequencies ν close to the zero field transition frequency ν_0, there is a certain amplitude for which the atoms are driven to the p state. This is the first Rabi minimum and a pulse driving the atoms to this state is called a π-pulse. For higher amplitudes the atoms are again in the s state and for even higher amplitudes they can be driven to the p state a second time - which corresponds to the second Rabi minimum. For higher and negative shifts $\nu - \nu_0$, the amplitude needed to drive the atoms to the p state becomes smaller.
Our goal is to find the position of the minimum. The corresponding amplitude describes the strength of the electric field mode at the chosen position of the atomic packet in the cavity. The frequency ν_{min} at which the Rabi oscillations are driven to the first Rabi minimum is not necessary the zero field transition frequency ν_0 between the 37p and the 37s state as we can see in Figure 4.10, where ν_{min} is around 3 MHz. We can draw conclusions on the stray fields inside the cavity from the detuning of the frequency ν_{min} from ν_0.

4.3.1. Measurement procedure

As it takes too long to measure a two dimensional map for every delay, we developed an iterative method with one dimensional traces for which we either vary the frequency or the amplitude. This can be best explained by looking at an example. In the measurement from the 20th of June we applied 20 ns long cavity pulses. We started with a delay corresponding to a position in the middle of the cavity, as Rabi oscillations can be driven more easily there. Closer to the edges of the cavity the contrast gets worse. For each delay of the cavity pulse we first guess an appropriate amplitude. This guess is based on neighboring points and old measurements. We then sweep the frequency over a range at least double as wide as the width of the dip. The result is a resonance as plotted in Figure 4.11, which we import to Mathematica and fit with a Gaussian curve to extract the minimum frequency ν_{min} corresponding to a Stark shift δ. We then use frequency ν_{min} for the trace in which the amplitude A is varied. The resulting Rabi oscillations are also imported to Mathematica and can be seen in Figure 4.11. The Rabi oscillations are fitted with a version of formula (2.61) with 0 detuning, pulse length $\delta t = 20$ ns and a Rabi frequency in Hz given by $\Omega = T \cdot A$, where T is the proportionality constant. The fit is hence given by the formula

$$P_{s\to p}(A) = \cos^2(\pi \cdot T \cdot A \cdot \delta t). \tag{4.5}$$

A π-pulse is obtained when $P_{s\to p}(x)$ is zero for the first time, which is the case for $T \cdot A_{min} \cdot \delta t = 1/2$. Using he proportionality constant T given by the fit, we can calculate the amplitude at the first Rabi minimum A_{min}. We then use this amplitude to take another frequency sweep. These two steps are done until the resonance frequencies and amplitudes for a π-pulse do not change anymore. If the procedure does not converge, a 2D plot is made. With this method we can find the necessary amplitude for a π-pulse and the corresponding Stark shift in a few minutes instead of almost an hour for a detailed 2D sweep.

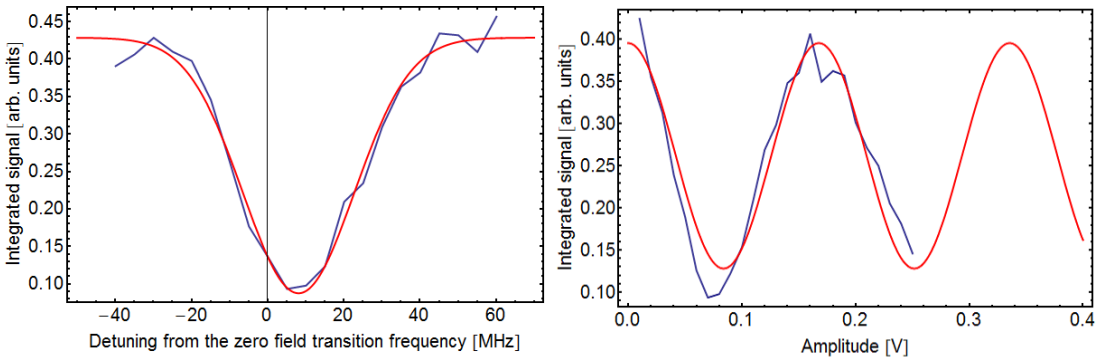

Figure 4.11.: *Finding the amplitude for a π-pulse and the corresponding detuning from ν_0. Data from the 20.06.2014 with a delay of 7.25 μs. The blue curves are the data obtained in the measurement. The red curves are fits. Left: Step 1: finding the frequency of the minimum. Right: Step 2: finding the amplitude of the first minimum.*

4.3.2. Results: Amplitude/powers for a π-pulse and its Stark shift

By repeating the two step iteration method for different delays, we can obtain the amplitude for a π-pulse and the corresponding detunings from the field free transition frequency as a function of the position of the atom packet in the cavity. The amplitude can be converted to power, which is used in the microwave generators (see section A.2).

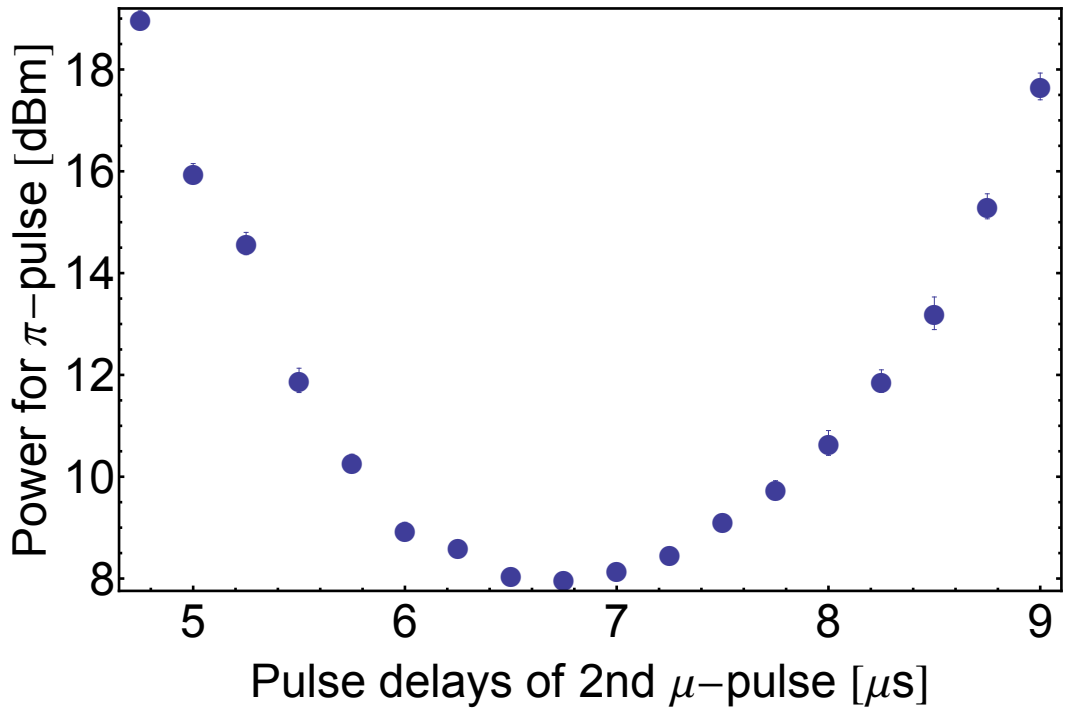

Figure 4.12.: *Rabi oscillation measurement: power for a π-pulse.*

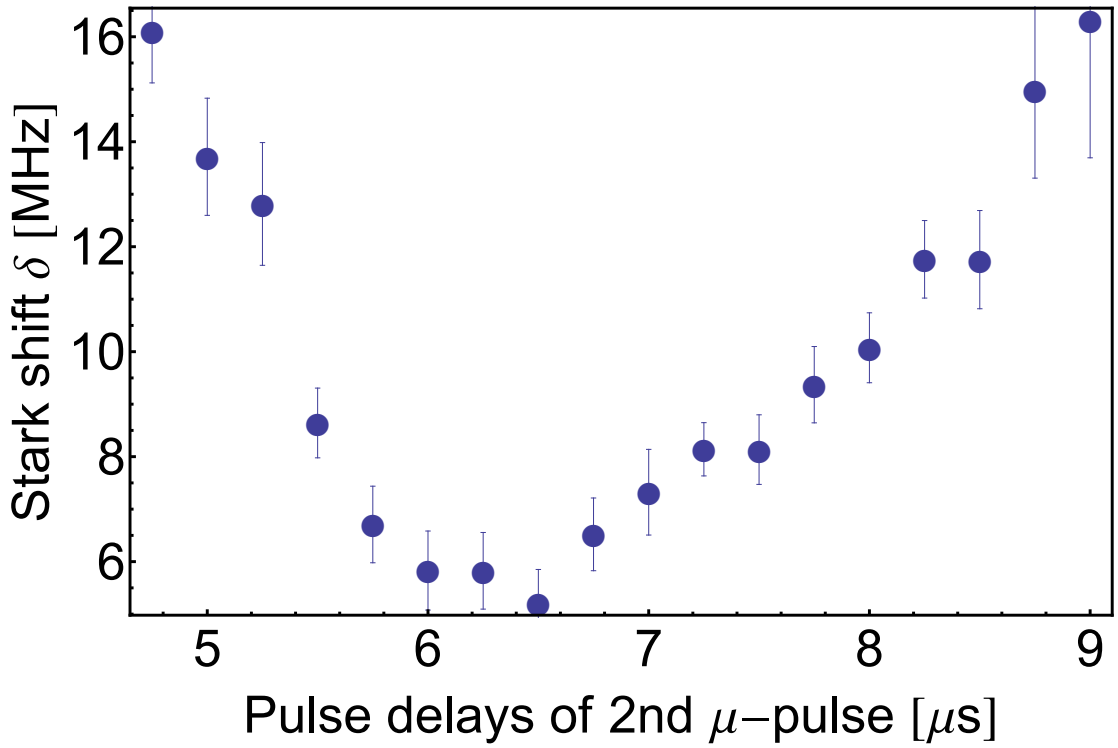

Figure 4.13.: *Rabi oscillation measurement: detuning from the zero field transition frequency.*

The result for the measurement done on the 20th of June is shown in Figure 4.12 for the power and Figure 4.13 for the detuning from the field free transition frequency (Stark shift).
Both the detuning and the power plot show a similar shape. At the sides of the cavity, the amplitude needed to drive a π-pulse is higher than in the center.. This leads us to the mode function, which will be discussed in the next section. The detuning is also higher on the sides of the cavity. This is due to stray fields in the proximity of the cavity walls and possibly in the beam hole. More conclusions can be made when comparing different measurements as is done in section 4.5. The error bars are calculated from the errors in the fit using Gaussian error propagation.

4.3.3. Results: Mode function

By finding the necessary amplitude for a π-pulse at different positions of the atom cloud in the cavity, we can map the microwave field of the cavity along the beam axis. The TE_{301} mode varies sinusoidally along the beam axis. At the sides the electric field is zero and maximal in the middle. The atoms need a certain electric field amplitude to be driven to the p state. Since the electric field of the mode is smaller at the sides than in the middle, a more powerful pulse has to be applied to achieve the same electric field at the sides. The normalized mode function can be obtained by calculating the inverse of the necessary amplitudes and then

normalizing the inverse values by the maximal inverse value:

$$\text{modefunction(delay)} = \frac{1/A}{Max\,[1/A]} \tag{4.6}$$

The modefunction is shown in Figure 4.14 and is characteristic for a cavity. We fit the function with a cosine. The offset to zero gives us the hypothetical center of the cavity.

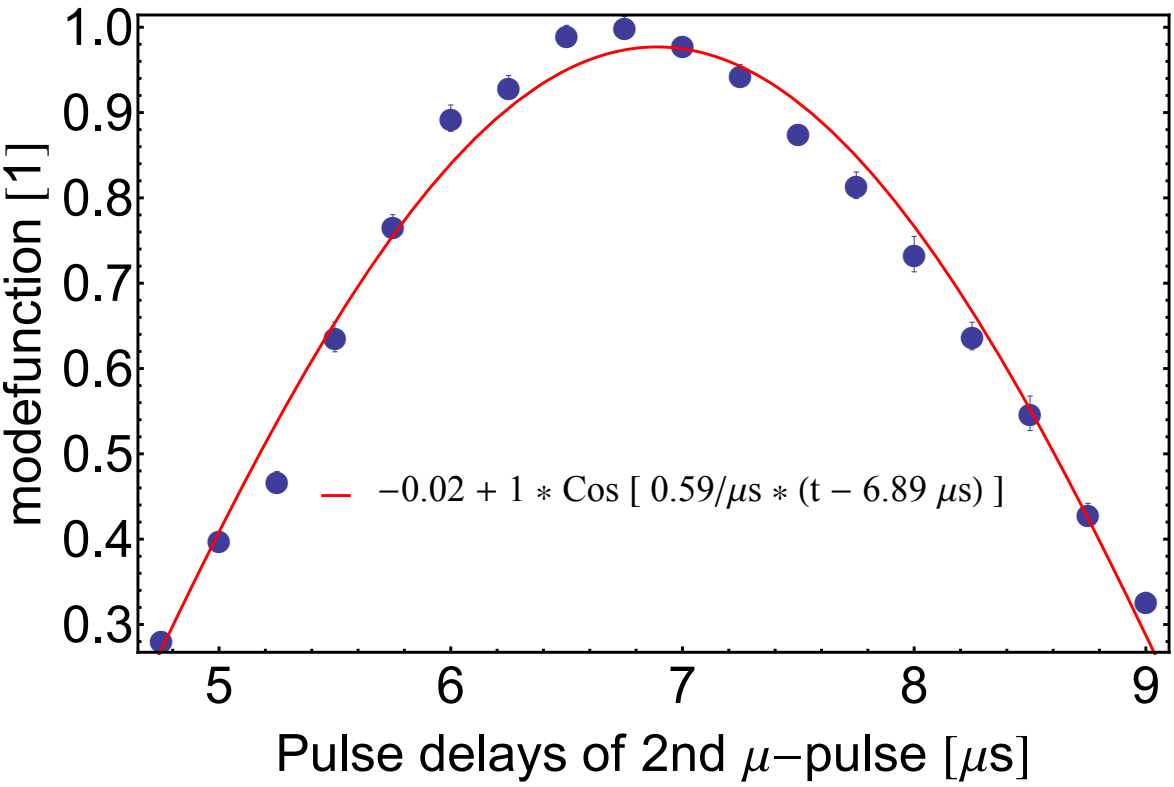

Figure 4.14.: *Rabi oscillation measurement: mode function with fit.*

4.4. Stark shift measurements

The second type of measurement characterizing the cavity determines the electric field generated by the electrodes. The electrodes were built into the cavity on the 29th of June and one measurement set with the electrodes was made. This measurement set is now presented.

The beginning of the Stark shift measurements is the same as in the Rabi oscillation measurements: a delay of the microwave pulse is chosen and the π-pulse amplitudes and the corresponding detuning are determined. These settings are used for the following microwave pulses. We then apply a potential anti-symmetrically to the electrodes, meaning that when the left electrode has voltage U, the right electrode has voltage -U, while the cavity body is at 0 V. This generates an electric field between the electrodes and the atom transition frequency is shifted due to the quadratic Stark effect as described in section 2.1.4. We can measure the shift in the transition frequency by applying a cavity pulse and fitting the resulting dip

with a Gaussian to obtain the new resonance frequency. The DC Stark shift $\Delta\nu_{Stark}$ is then defined as the difference of the resonance frequency to the zero-field transition frequency ν_0. We also obtain a small DC Stark shift for zero applied voltage due to stray fields. By applying different voltages U, we can see the quadratic dependance of the shift on the voltage. The function can be fitted with

$$\Delta\nu_{Stark} = A\,(U - U_0)^2 + B. \tag{4.7}$$

An example is given in Figure 4.15 for a delay of 6.5 μs , where we can shift the atomic transition frequency by up to 100 MHz. Being able to vary the detuning can be useful for measuring a dispersive shift.

The Stark shift measurement can be done for other delays as well. We usually determined the Stark shift for 7 different voltages distributed symmetrically around 0 V. This is enough to obtain reasonable fits.

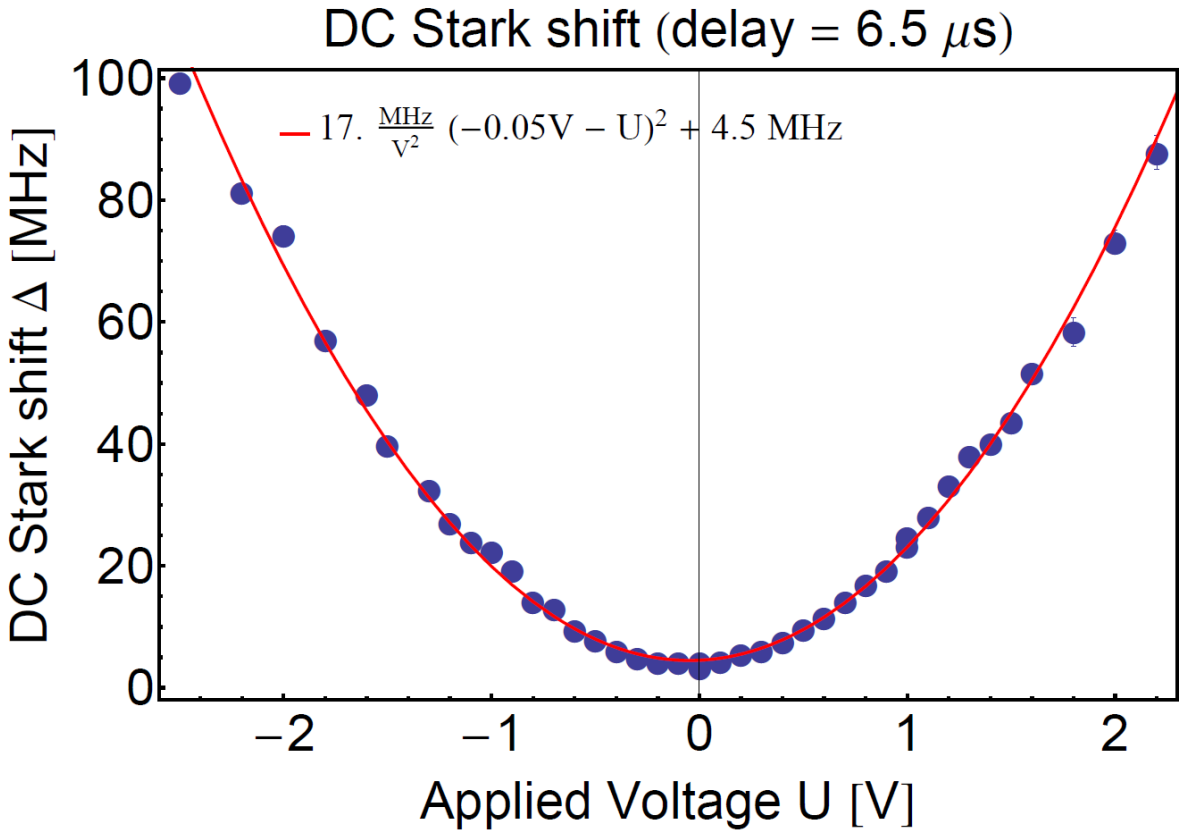

Figure 4.15.: *Stark shift for different applied voltages at a delay of 6.5 μs.*

4.4.1. Electric field from the electrodes

The electric field from the electrodes along the beam axis can be calculated from the fitting parameters A, U_0 and B for the different delays. A relationship between the parameters and the electric field can be found by looking at equation (2.29) linking the Stark shift with the

electric field:

$$\Delta\nu_{Stark} = \frac{1}{2}\Delta\alpha\vec{F}^2, \tag{4.8}$$

where $\Delta\alpha = 1948$ MHz $(V/cm)^{-2}$ for the $37p \leftrightarrow 37s$ transition.

The electric field the atom experiences is composed of the field created by the electrodes and the stray electric field inside the cavity. We know from simulation that the field from the electrodes mainly has a component in the direction of the straight line joining the two electrodes. We can then decompose $\vec{F}$ into a component $F_\parallel$ parallel and a component orthogonal $F_\perp$ to the applied field. The orthogonal component only depends on the stray field, while the parallel component also depends on the applied voltage U scaled by a factor c relating the potential difference U with the electric F of the electrodes. The amplitude squared of the electric field can hence be written as [28]

$$\vec{F}^2 = F_\perp^2 + F_\parallel^2 = F_{\perp stray}^2 + \left(F_{\parallel stray} - cV\right)^2. \tag{4.9}$$

We can plug this into the equation for the Stark shift and obtain

$$\Delta\nu_{Stark} = \frac{1}{2}\Delta\alpha F_{\perp stray}^2 + \frac{1}{2}\Delta\alpha\left(F_{\parallel stray} - cV\right)^2. \tag{4.10}$$

The first term corresponds to the offset B. The minimal shift occurs at voltage U_0 and is in this formula achieved for $F_\parallel = 0$ meaning that $F_{\parallel stray} = cU_0$. Plugging this into (4.10) gives us a relation for A. Rearranging the formulae results in:

$$c = \sqrt{\frac{2A}{\Delta\alpha}} \tag{4.11a}$$

$$F_{\parallel stray} = cU_0 = V_0\sqrt{\frac{2A}{\Delta\alpha}} \tag{4.11b}$$

$$F_{\perp stray} = \sqrt{\frac{2B}{\Delta\alpha}}. \tag{4.11c}$$

The electric field from the electrodes is given by multiplying the applied potential with the factor c. This is done in Figure 4.16 for a voltage of 1 V. The vertical blue lines give an error estimation, which is obtained from the errors of the fitting procedure of each parabola and Gaussian error propagation. The data is plotted with respect to the distance from the cavity center. The cavity center is obtained from the modefunction and the delays are converted to positions using the velocity of the atoms. This will be described in more detail in section 4.5.

We can also simulate the electric field from the electrodes in HFSS or Comsol. The electric field data around the beam axis can then be imported to Mathematica. Since the atom cloud is not just a point but spacious, 3 different beam paths are simulated and plotted in Figure 4.16. The blue curve corresponds to a beam passing through the center of the hole as we hope is the case for our beam. The green curve gives an upper boundary to the electric field

magnitude and corresponds to the field experienced by atoms passing through the cavity at the horizontal edge of the hole, which is closer to the electrodes. The red curves gives analogously the lower boundary. These three paths are discussed in more detail in chapter 5.
Figure 4.16 shows that the simulated field through the hole center and the measured one are quite similar. The measured field before the atoms arrive in the center is slightly lower than we would expect from simulations, after the center it is however slightly higher.

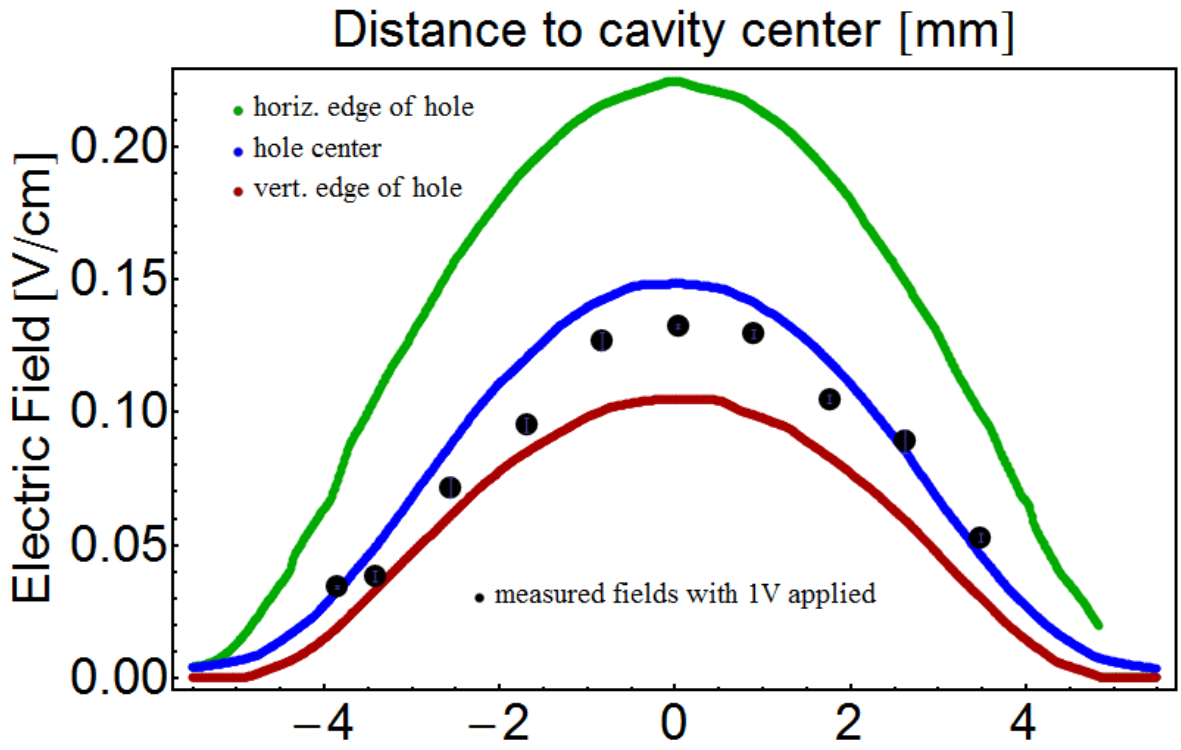

Figure 4.16.: *Electric field along the beam axis due to the electrodes. The black dots are measurements, while the blue, green and red curves are simulated fields along different beam paths.*

4.4.2. Stray fields along the beam axis

From the fit parameters we can not only get the electric field created by the electrodes but also the extent of the stray fields along the beam axis. Using equations 4.11 (a) and (b) results in the stray fields plotted in 4.17. Except at the cavity entrance, the stray fields are a lot higher perpendicular to the axis connecting the two electrodes than parallel to it. The stray fields $F_{\perp stray}$ along the beam axis are higher at the entrance than after the center of the cavity.

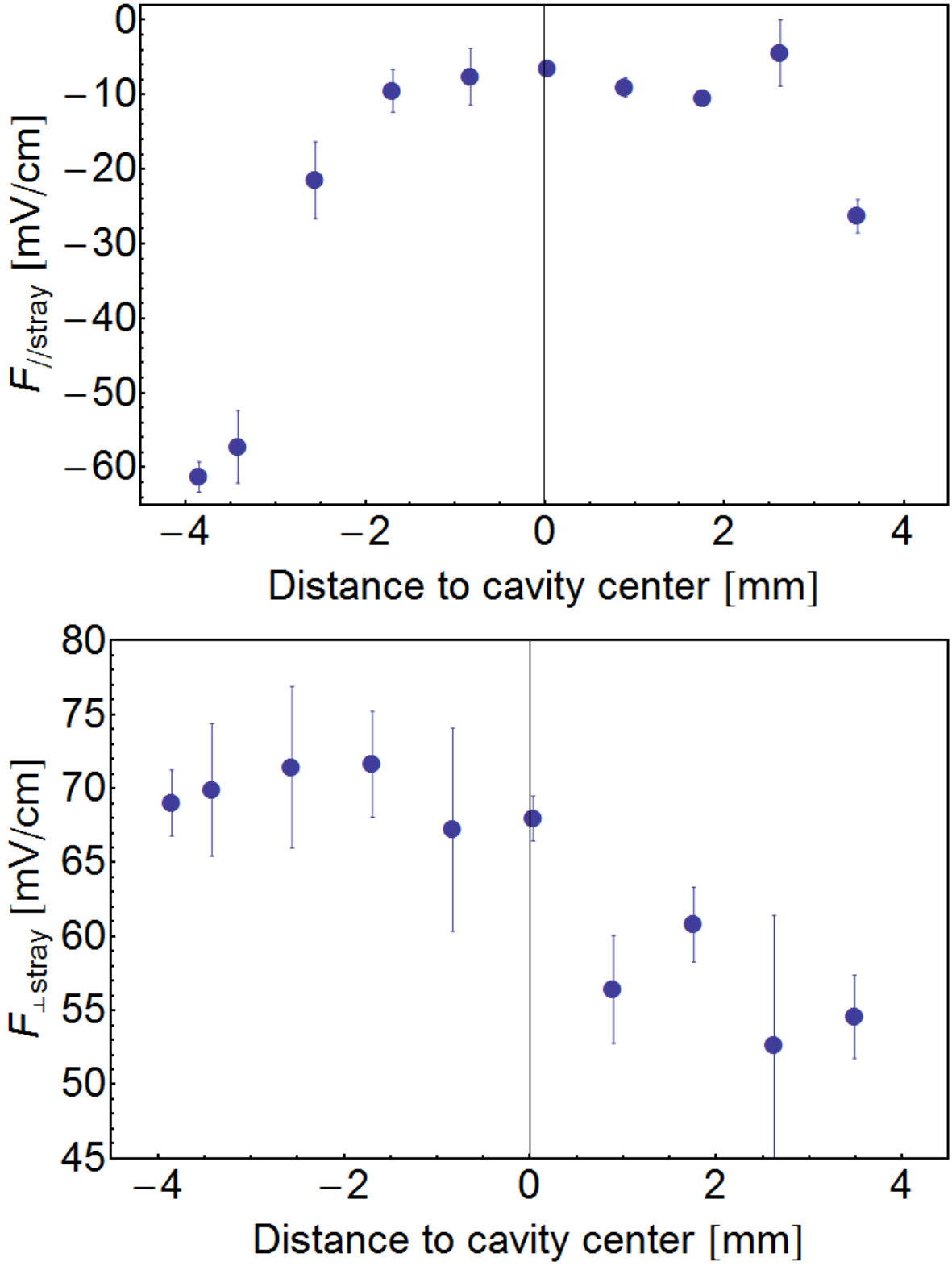

Figure 4.17.: *Stray fields along the beam axis due to the electrodes.*

4.5. Comparison of the measurements

In this section we compare four measurement sets taken with different cavity configurations. The first is from the first experiment measuring modefunctions, the second the measurement from the 20th June described earlier, the third the cold measurement and the fourth the measurement with the electrodes. As a common x-axis, the distance from the cavity center instead of the delay is chosen. The delay is converted into the distance by taking the maximum of the modefunction fit as the center of the cavity and then calculating the position using the velocities given in Table 4.3. For the first measurement the velocity was not measured and we therefore took a velocity in the middle of the measured ones: 1.75 mm/μs. The modefunctions of the three warm measurements are very similar as can be seen in Figure 4.18. The modefunction obtained in the cold measurement is narrower. This effect, however, can not be explained by the contraction of the cavity at low temperatures, which is only about 0.02 mm. The reason for the narrower modefunction is not fully understood, but may be due to wrong alignment and large stray fields resulting in an imprecise measurement.

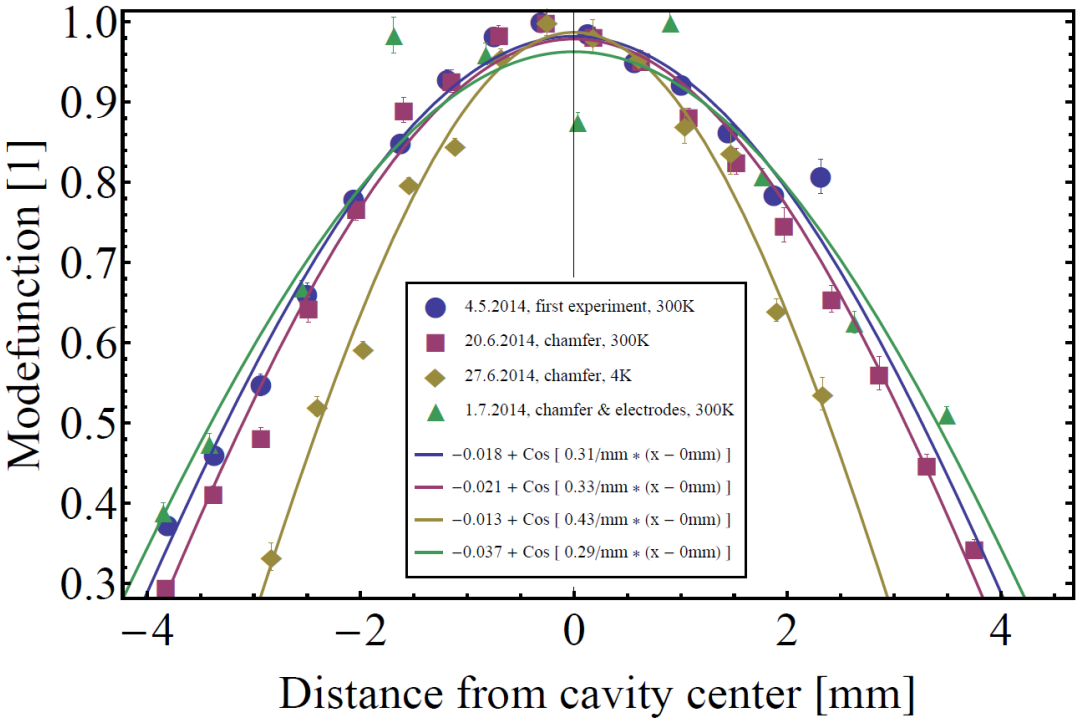

Figure 4.18.: *Comparison of the modefunctions obtained in 4 different measurement sets.*

For the power and detuning plots the x-axis determined for the modefunction is used. The lowest detunings are therefore not necessarily achieved in the hypothetical center of the cavity. Figure 4.19 summarizes the 4 measurements that determine the power for a π-pulse and Figure 4.20 the detuning. Since the length δt of a pulse influences the power needed to drive the atoms to the p state, the powers in the first two measurements are converted to the case of a 100 ns

pulse instead of a 20 ns pulse by subtracting 14 dB [1]. For the detunings the corresponding electric fields are calculated using the quadratic Stark shift. The necessary power varies between the different measurements and depends on the coupling and the alignment. From the detuning measurements we can say something about the stray fields. In the case of the electrode measurement the detuning is very low and does not vary as much with position as in the other cases. If this is due to the electrodes or the good alignment that was fond, is yet unclear. The stray fields at the cavity edges are higher than in the middle of the cavity. The minimum in the stray field is obtained before the cavity center defined by the mode function is reached. Rabi oscillations can be driven between -4 and 4 mm from the cavity center. This corresponds to the cavity length along the beam axis of 8 mm.

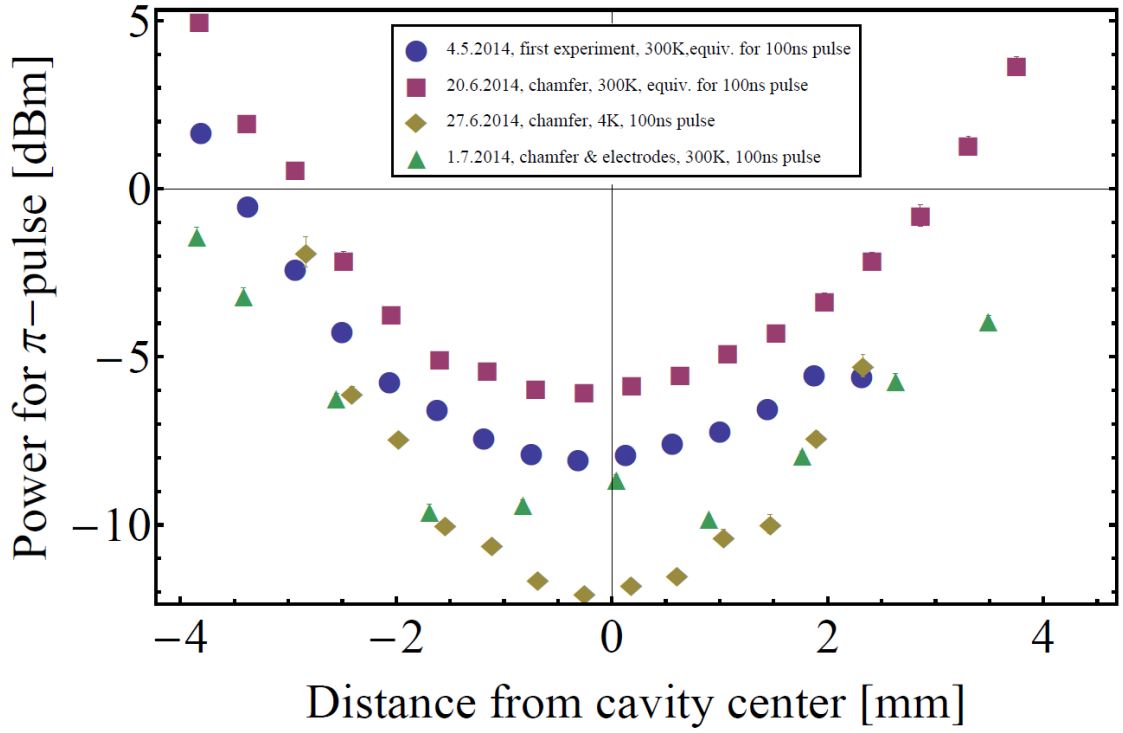

Figure 4.19.: *Comparison of the π-pulse powers obtained in 4 different measurement sets. In the first two power measurements, the power for a π-pulse is converted to the case of 100 ns.*

[1] A 5 times shorter pulse needs 5 times the amplitude to drive the atoms to the p state. $10 \log\left(5^2\right) = 14$

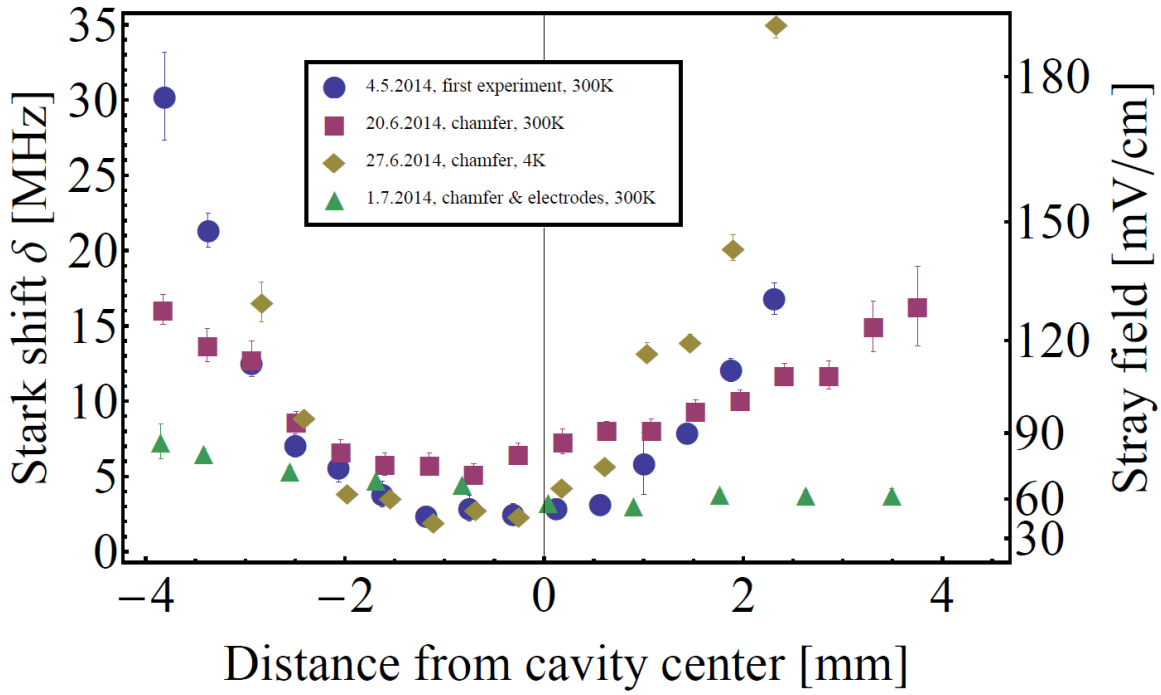

Figure 4.20.: *Comparison of the detunings from the zero field frequency in 4 different measurement sets. The scale on the right gives the corresponding electric field for the Stark shift.*

5. Design of a new cavity

In the Stark shift measurement we obtained the electric field along the beam axis produced by the electrodes (see section 4.4.1). In the future this field will be used in measurements of the dispersive shift to define the transition frequency of the atoms and with that the detuning Δ. If the electric field is not homogeneous inside the cavity (both along the beam axis and transversally), the measurable detuning will be broadened, since the ensemble of Rydberg atoms samples the beam path with a transversal extension of approximately the cavity hole diameter. As a consequence of the detuning not being well defined, the dispersive shift will be blurred. We therefore want a cavity whose electrode field is homogeneous and flat over a long distance. This should be achieved with cavity 5, the successor of cavity 4B. In this chapter the requirements, the design process and the final cavities are described.

5.1. Requirements

The idea is to build a new cavity based on cavity 4B and just change the dimensions. Since we want to create a DC electric field that is approximately constant over at least 8 mm along the beam axis (longer than the depth of cavity 4B), the depth d of the cavity has to be increased. Cavity 4B is 8 mm deep and cut out from a copper block of 11 mm thickness. In the setup the cavity is placed between electrode 2 and 3, which are 15 mm apart. If we want to place a bigger cavity there, we need to take electrode 3 out, which is possible since we still have electrodes 4 and 5 for the ionization. This gives us an additional length of 11 mm.
Increasing the depth d of the cavity leads to several other changes. The resonance frequency of the cavity depends on the dimensions a, b and d (see equation (2.34)). In order to be able to drive transitions from the s to the p state and for cavity QED experiments, a cavity mode needs to be close to one of the transition frequencies of the excited helium atoms. The transition frequencies in the range of the down conversion board are given in table 5.1.

Transition frequencies ns $\rightarrow$ np					
n	35	36	37	38	39
f_{res} [GHz]	25.563	23.430	21.528	19.826	18.299

Table 5.1.: *Transition frequencies between the ns and np states in the frequency range 18 to 26 GHz.*

We could of course take another mode than TE_{301}, but this mode has many advantages for our purposes. The first advantage is that it has a maximum where the atoms traverse the

cavity. The atoms can thus be transferred from the s to the p state and back and the coupling strength g is maximal. Second, the mode has two minima where we can place the electrodes. When the electrodes are in the minima, the cavity mode is barely disturbed. Third, the mode is one of the modes with the lowest resonance frequencies. In cavity 4B, mode TE_{301} is the third mode in the spectrum of resonance frequencies. Higher modes are generally closer in frequency, meaning that sometimes not just one mode is excited with a certain frequency. In cavity QED other resonances close to the transition (small Δ) add unwanted dispersive shifts, which we want to avoid. The new cavity should therefore again have mode TE_{301} as the mode of interest. This mode should be near one of the transitions stated earlier and the neighboring modes should be at least 1 GHz apart.
The cavity dimensions and the chosen mode also determine the mode volume of the cavity. The coupling g, which is one figure of merit for cavity QED experiments, depends on the mode volume via the rms zero-point electric field $\mathcal{E}_{rms}$ (see equations (2.50) and (2.52)). A smaller mode volume leads to a stronger coupling g and a greater dispersive shift $\chi = \frac{g^2}{\Delta}$. This means restricts the size of the cavity.
The requirements for cavity 5 can thus be summarized:

- Cavity 5 should fit in between electrode 2 and 4 with a clearance of at least 2 mm.
- The dimensions a, b and d should be such that mode TE_{301} is closely matched to one of the transition frequencies given in table 5.1.
- Other modes should be more than 1 GHz away from mode TE_{301}.
- The electrodes should be positioned in the minima of mode TE_{301}.
- The electric field produced by the electrodes should be flat over at least 8 mm along the beam axis.
- The electric field should be homogeneous over the size of the cavity entry hole at each position along the beam axis.
- The mode volume of the cavity should be small.

We can still vary a number of parameters, namely:

- The transition n.
- The cavity dimensions: width a, height b, depth d
- The atomic beam hole size defining how far from the hole center the atoms can pass through the cavity.

The separation of the electrodes depends on the cavity dimensions and is approximately given by one third of the width a. We can have two differently shaped electrodes - either cylindrical electrodes or plates are possible. Since there are more degrees of freedom than needed, we

reduce their number by fixing the depth d of the cavity to 16 mm, which is twice the length of cavity 4B and still allows the cavity to fit in between electrode 2 and 4. We will now look for values a, b and n that fulfill the requirements above. For this task the fields of the electrodes as well as the resonance frequency and minima of the mode have to be simulated.

5.2. Optimizing the field inhomogeneity and plateau length

We simulate the electric field in two programs: Comsol for the field of the electrodes and HFSS for the modes inside the cavity. In both programs we can import the CAD design of the cavity, define a mesh, materials and boundary conditions and then simulate the relevant field. All the changes to the cavity are done in the CAD program. In order to minimize the inhomogeneity and maximize the plateau length over which the electric field is approximately constant, we first have to explain what we mean by these quantities and define the measures of it. This will be done with the field configuration of cavity 4B. In a second step we will simulate the inhomogeneity for new cavity configurations.

Inhomogeneity of the electric field magnitude

The inhomogeneity and plateau length can be explained demonstratively with the example of cavity 4B. The electrodes produce the electric field shown in Figure 5.1 when 1 V is applied to the left electrode, -1 V to the right and 0 V to the cavity. Let us first examine the electric field along the beam axis (figure (a)). As we have measured in the experiments, the atoms encounter an increasing electric DC field magnitude along their path through the cavity until they reach the center, where the field starts to decrease again. The magnitude of the field changes more rapidly in the vicinity of the cavity walls than at the center. We call the flat part the plateau.

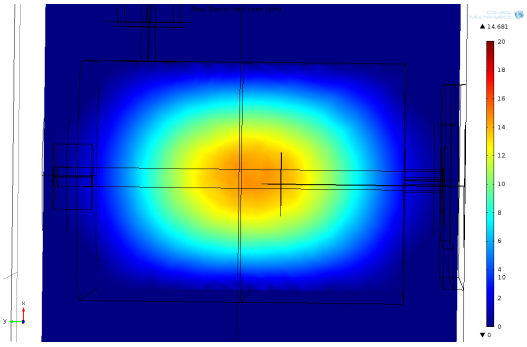

(a) *Side view. The atoms fly along the horizontal middle line of the shown slice. The field is strongest in the center of their path.*

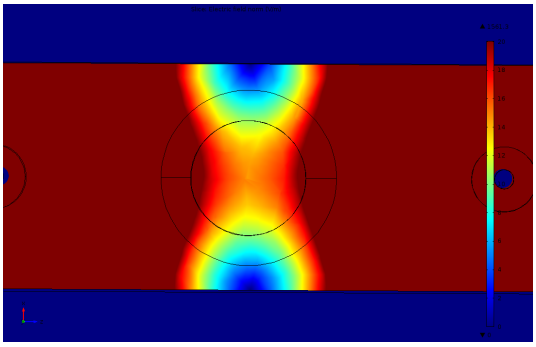

(b) *Front view. The atoms fly perpendicular to this slice through the hole in the center. The field is strongest to the horizontal sides of the hole and lowest at the vertical sides.*

Figure 5.1.: *Simulations of the electric field magnitude from the electrodes with 1 V applied to the left electrode and -1 V to the right. Blue corresponds to 0 electric field magnitude, red is 20 V/m and above.*

If we now look at the field from the front (i.e. perpendicular to the atomic beam axis, figure (b)), we can see that the electric field magnitude at the horizontal sides of the hole is higher than in the center, because these sides are closer to the electrodes. In contrast, the vertical sides of the hole have lower electric field magnitudes.
It is also useful to plot the electric field magnitude along these three atom paths (see Figure 5.2:

- Along the atomic beam axis through the center of the hole (blue curve).
- Parallel to the atomic beam axis through one of the horizontal sides of the hole (green curve). This results in the highest field magnitude.
- Parallel to the atomic beam axis through one of the vertical sides of the hole (red curve). This results in the lowest field magnitude.

Atoms passing through other parts of the hole encounter an electric field with a magnitude between the green and the red curve.

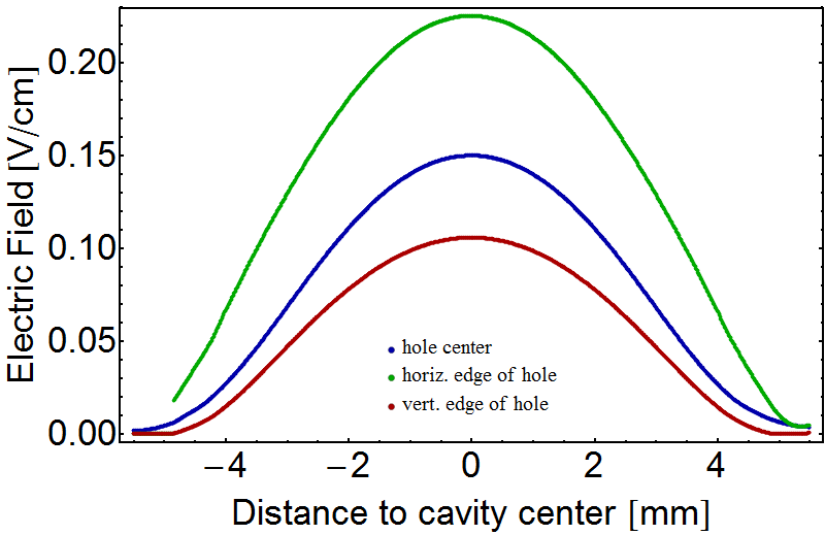

Figure 5.2.: *Electric field amplitude along 3 possible (extreme) atom beam paths for cavity 4B. The blue curve is along the atomic beam axis through the center of the hole, the green through the horizontal side of the hole and red through the vertical side.*

In the simulations we do not just evaluate the field along these three paths, but also simulate the field on a 3D grid with 0.1 mm spacing in all directions. This field data is obtained in a Comsol simulation and then exported to Mathematica. There we choose the paths which lay inside a radius of the size of the hole - in our case 2 or 3 mm. For each slice z perpendicular to the beam axis we calculate the mean electric field magnitude $E(z)$ and the standard deviation $\Delta E(z)$. The inhomogeneity β of each slice is than defined as

$$\beta(z) = \frac{\Delta E(z)}{E(z)}. \tag{5.1}$$

Since we want a plateau of at least 8 mm length, we decided to define the *8 mm plateau* as all the z values up to 4 mm from the cavity center. We can then calculate the minimal, the mean and the maximal inhomogeneity over this 8 mm plateau. With these three numbers we can characterize the inhomogeneity perpendicular to the beam axis.
The plateau length is characterized indirectly by monitoring the percentage the mean electric field magnitude $E(z)$ drops at z = 4 mm from the cavity center. We normalize the field amplitude to 1 and then obtain the loss of the electric field after 4 mm from the center by subtracting the normalized electric field at z = 4 mm from 1. This loss can be interpreted as the inhomogeneity of the electric field along the beam axis.
We now have a measure to access the inhomogeneity of a cavity configuration along and perpendicular to the beam axis.

Simulations of the inhomogeneity

In the simulations we will choose one specific cavity configuration and vary one parameter to see its affect on the inhomogeneity. The cavity configuration is obtained with the following chain of thought: a larger depth d = 16 mm results in a lower transition frequency, if we leave the other parameters constant. The lowest possible transition frequency belongs to n = 39 with 18.299 GHz. The resonance frequency of mode TE_{301} does not depend on the height b of the cavity, so we can obtain the width a from formula (2.34): 28.6 mm. We can take the height b as the first parameter we vary. For the distance of the electrodes we take 10 mm, which is slightly higher than one third of a. For the atomic beam hole we take a diameter of 2 mm as the inhomogeneity is smaller for a smaller hole. The obtained inhomogeneity for this setup is plotted with respect to the cavity height b in Figure 5.3 (a). We can conclude that for cylindrical electrodes a larger cavity height b is better for the inhomogeneity $\frac{\Delta E}{E}$, but worse for the plateau length.
In a second simulation we choose the same cavity configuration as above, but vary the distance between the electrodes disregarding the fact that the electrodes will not be at the nodes of the cavity field. The cavity height b is set to 6 mm, which corresponds to the value used for cavity 4B. The result is displayed in Figure 5.3 (b). The inhomogeneity $\frac{\Delta E}{E}$ varies by about 0.5 % for electrode distances between 7.5 and 10 mm and the distance of the electrodes is hence not relevant for the inhomogeneity. The loss in electric field however increases significantly with the electrode distance. It is therefore advantageous to place round electrodes as close together as possible. Simulations with plate electrodes show the same behavior: the electrodes should be as close as possible. The distance between the electrode also defines the width a of the cavity, as the electrodes are to be placed in the minima of the TE_{301} mode whose position is basically determined by the width a. We can summarize:

- A larger height is better for the plateau length, but worse for the homogeneity.
- A shorter distance between the electrodes is better for the plateau length and irrelevant for the inhomogeneity.

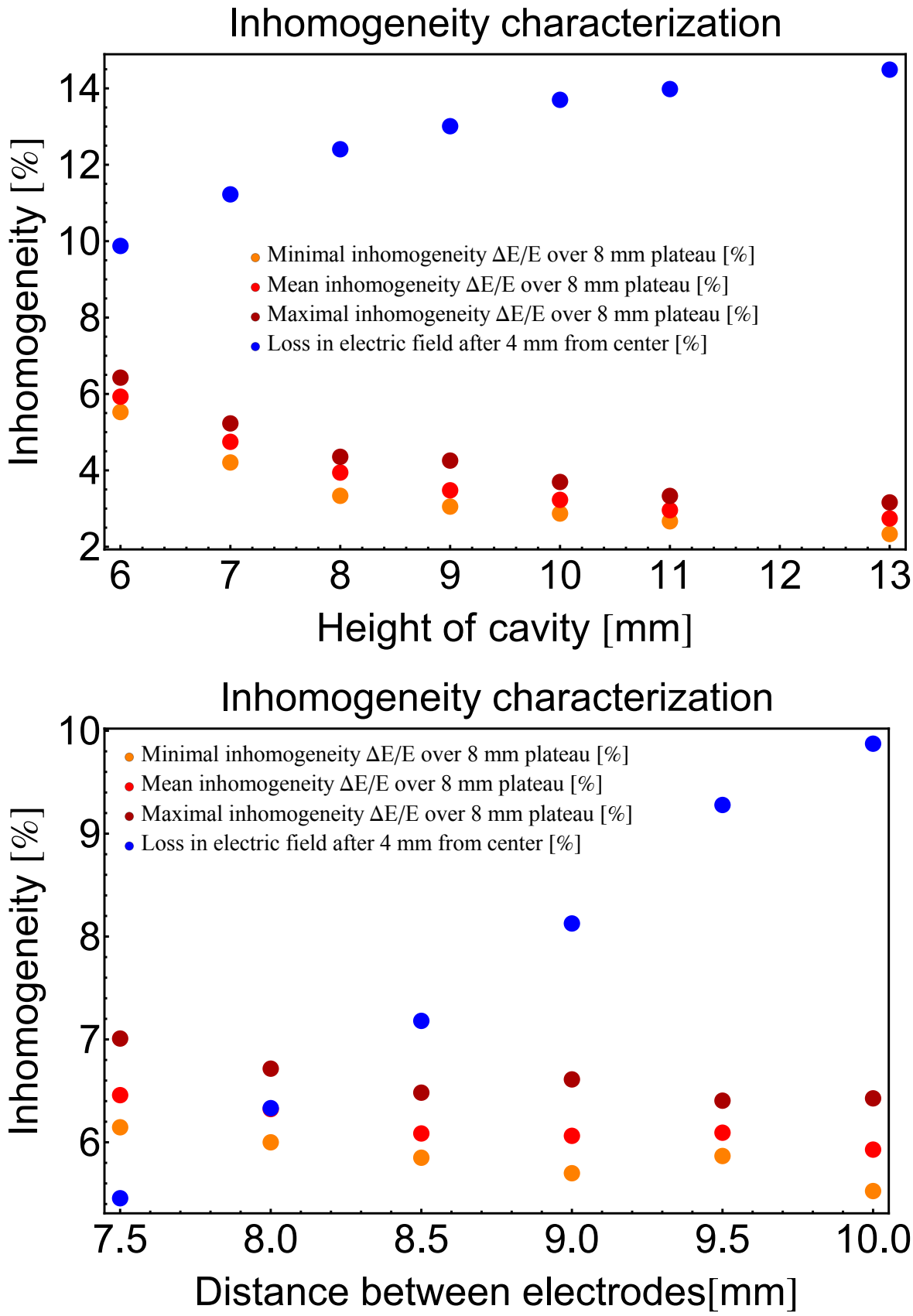

Figure 5.3.: *Inhomogeneity characterization of the electric field for different cavity heights and electrode distances. The simulated cavity has a length a = 28.6 mm, a depth d = 16 mm, a hole diameter of 2 mm and round electrodes. In (a) the distance of the electrodes is 10 mm. In (b) the cavity has a heigth b = 6 mm.*

5.3. Final cavities

The results of the simulations suggest to build a cavity with a short distance between the electrodes. The proximity of the electrodes is however limited by the fact that the atomic beam still has to pass in between the electrodes and atoms should not be disturbed by the proximity of the electrodes. Furthermore, the electrodes have to be fixed inside the cavity such that the dips holding the electrodes do not overlap with the atomic hole. The hole should again have a diameter of 3 mm, since stray fields occurring in the hole could also distract the atoms flying nearby. In order to study the effects of a smaller hole diameter, we intend to use 1 mm thick copper plates with 1 and 2 mm diameter holes that can be screwed in front of the cavity. The electrodes should therefore be at least 7 mm apart.

From the transition frequencies and the depth d = 16 mm, we can directly obtain the possible cavity widths a: 28.6 mm, 25.7 mm, 23.2 mm, 20.9 mm and 18.9 mm. The corresponding electrode distances are a bit lower than one third of the cavity width. A cavity with 23.2 mm width and transition n = 37 should have the electrodes a bit more than 7 mm apart. This will lead us to cavity 5A. Since the atoms could be negatively affected by stray fields created by the electrodes, we decided to build a second cavity with a larger distance between the electrodes. The so called cavity 5B with 28.6 mm width and transition n = 39 will have electrodes separated by around 9 mm. These numbers may still slightly change as the cavity is rounded and formula (2.34) only gives us accurate frequencies for a rectangular cavity.

Increasing the cavity height above 9 mm leads to a (l,1,0) mode getting close to the resonance, which we want to avoid. As higher cavities have lower inhomogeneity, we take b = 9 mm for both cavities. With these dimensions, the modes of the cavity can be simulated in HFSS. If the resulting frequency is too detuned from the atomic transition, the cavity width and the position of the electrodes are adjusted. The simulation is then repeated with the new dimensions until the desired frequency is obtained. The dimensions found in this procedure - and those of cavity 4B for comparison - are listed in Table 5.2.

Cavity dimensions

	4B	5A	5B
Width a [mm]	43	23.9	29
Height b [mm]	6	9	9
Depth d [mm]	8	16	16
Electrode distance [mm]	13.36	7.86	9.7
Diameter hole [mm]	3	3	3
Transition n	37	37	39

Table 5.2.: *Dimensions of cavity 4B, 5A and 5B.*

We can also simulate the electric field for these cavity configurations and calculate the inhomogeneities. The normalized electric fields for cavity 5A and 5B either with the round electrodes or the plate electrodes are displayed in Figure 5.4 along with the inhomogeneity characterization. The lowest inhomogeneities are achieved for cavity 5A with the plate

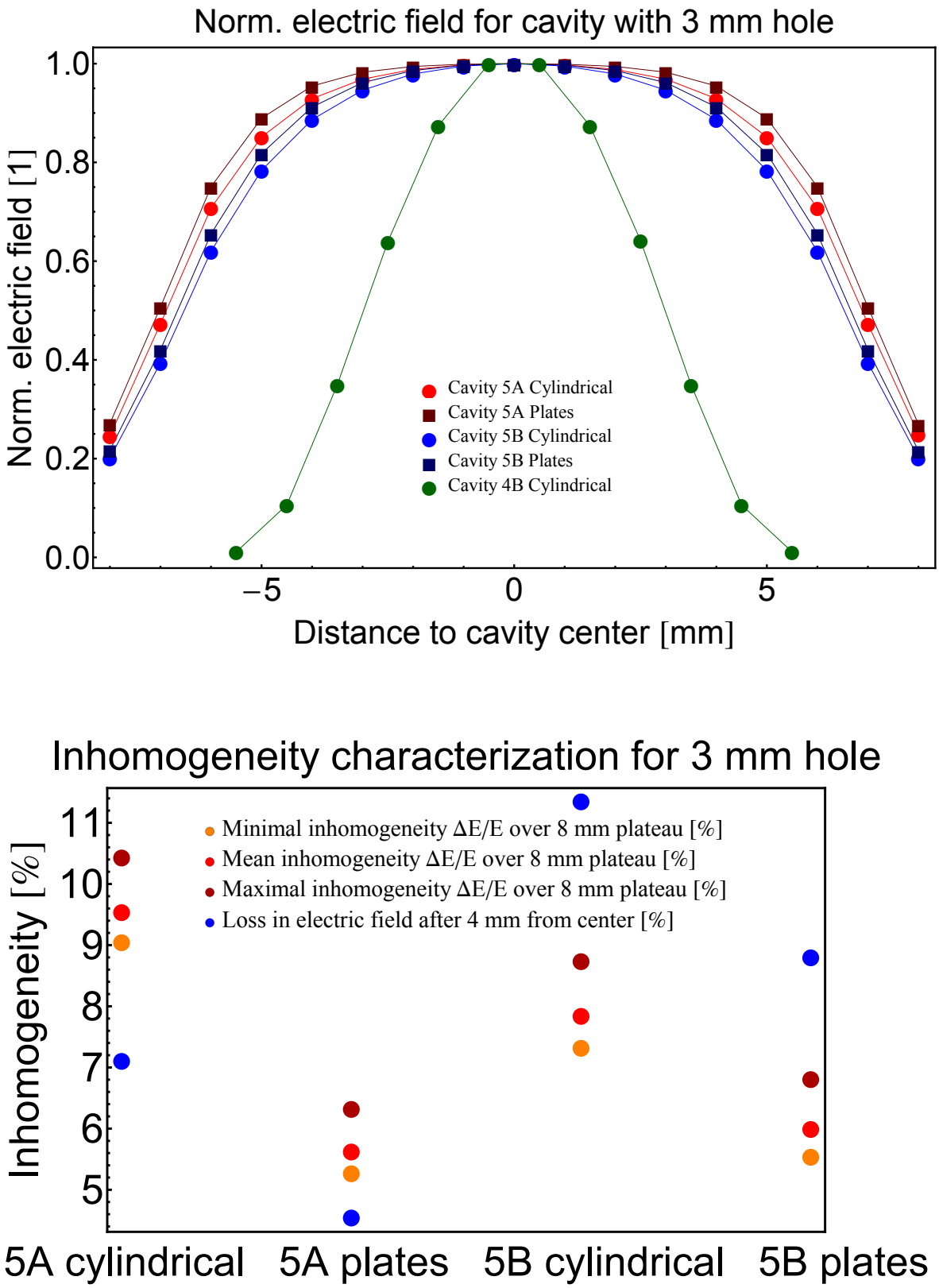

Figure 5.4.: *Electric field and inhomogeneity characterization for cavity 5A and 5B. The normalized electric field of cavity 4B is given for comparison.*

electrodes, where the loss in electric field over the 8 mm plateau is below 5% and $\beta \approx 6\%$. We can calculate the uncertainty in the Stark shift $\delta\Delta\nu_{Stark}$ caused by the inhomogeneity β in the electric field with:

$$\begin{aligned} \delta\Delta\nu_{Stark} &= \Delta\alpha \cdot E \cdot \delta E \\ &= \Delta\alpha \cdot E^2 \cdot \beta \\ &= 2\Delta\nu_{Stark} \cdot \beta. \end{aligned} \tag{5.2}$$

The line width $\gamma/2\pi$ of the atomic resonance is broadened by the uncertainty in the Stark shift $\delta\Delta\nu_{Stark}$ compared to the zero field case where $\gamma_0/2\pi$ is approximately 500 kHz for 37p state atoms and 10 kHz for 37s state atoms. The line width $\kappa/2\pi$ of a critically coupled cavity with an internal quality factor of 10'000 is 4 MHz, which is a lot bigger than the line width of the atomic resonance. For cavity 5A with $\beta = 6\%$ the uncertainty in the Stark shift $\delta\Delta\nu_{Stark}$ reaches 4 MHz, when a Stark shift $\Delta\nu_{Stark}$ of around 33 MHz is applied. We can therefore vary the detuning Δ by about 33 MHz with cavity 5A before the line width of the atomic transition $\gamma/2\pi$ gets bigger than the line width of the critically coupled cavity $\kappa/2\pi$.

6. Characterization of the amplification system

An excellent low noise amplification and detection system is needed to measure microwave signals at the few photon level with a power of around -140 dBm. Such signals arise, for example, in experiments measuring the dispersive shifts of the cavity frequency or vacuum Rabi oscillations. The necessary components for this task have already been assembled and will be described in section 6.1. In order to be able to detect the few photon signal coming from the resonator, the signal has to be amplified without adding to many noise photons. The signal-to-noise ratio (SNR) measures the quality of the amplification and detection process and can be used to calculate the measurement time needed for the observation of the dispersive shift [57]. Two quantities play a mayor role in measuring the quality of the amplification process: the gain of the amplifiers and their noise temperatures. We will start with the discussion of the gain measurements of the individual amplifiers in section 6.2 and continue with the gain measurement of the whole down conversion board (DCB) in section 6.3, where we will also present a first experiment using the DCB to characterize the resonances of cavity 4B. In the last section we will describe how we measured the noise temperature of the individual components and discuss the results.

6.1. Components

The goal of the amplification and detection setup is to measure the complex amplitude $S(t) = I(t) + iQ(t)$ of the emitted microwave radiation, where $I(t) \in \mathbb{R}$ is the in-phase and $Q(t) \in \mathbb{R}$ the quadrature component of $S(t)$. Commonly, $I(t)$ and $Q(t)$ are called the quadratures. The complex amplitude $S(t)$ is measured at discretized times t by demodulating the microwave signal from the carrier frequency to 0 Hz. This is done in a heterodyne detection scheme [58], which means that the demodulation is performed in two steps. In the first step, the signal is demodulated from the carrier frequency (18-26.5 GHz) to the intermediate frequency of 25 MHz. This is done by a microwave mixer on the down conversion board. In the second step, the down converted signal is digitized by an analog to digital converter, whose output is a waveform of digitized voltages $V(t)$ at discrete points in time. These voltages are then digitally down converted and filtered with a field programmable gate array (FPGA). The advantage of an FPGA is that it can run continuously and in real-time on every data point as it is massively parallelized. We can control the detection procedure and access the processed data with the LabView program CleanSweep. Further calculations with the quadratures $I(t)$

and $Q(t)$ are done in Mathematica.
The signal can not simply be down converted twice, but needs to be amplified and filtered in various steps. This is done inside the experiment on the 3 K stage and also outside at 300 K on the down conversion board. The FPGA performs digital filtering, but we will now focus on the analog components and characterize their performance. The analog amplification and detection system can be seen schematically in Figure 6.1. A list of the components used with their frequency range and maximal power input is given in Table 6.1.

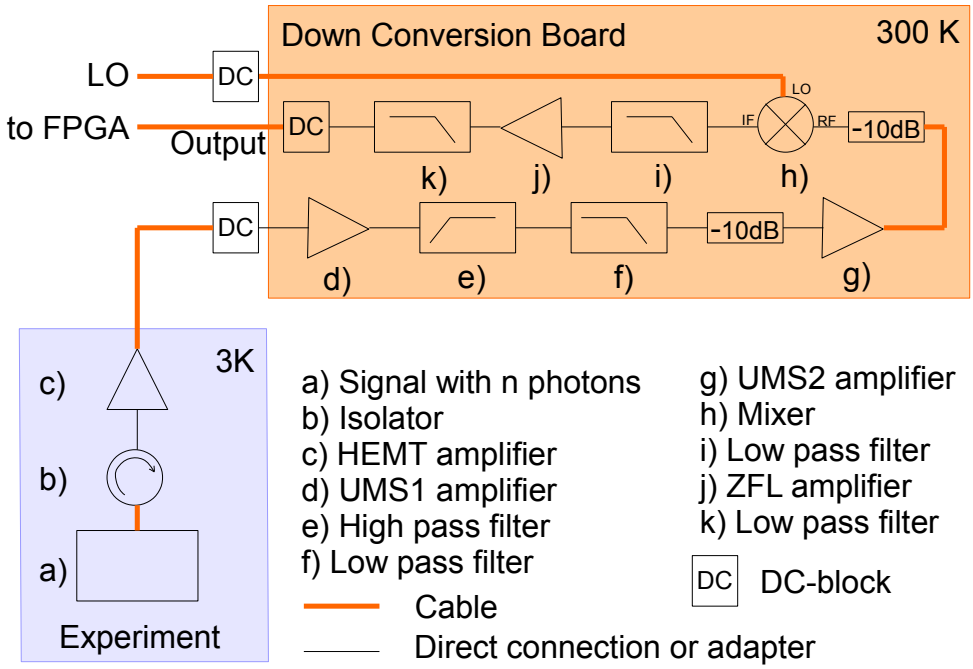

Figure 6.1.: *Schematic of the analog part of the amplification and detection system. The attenuators and adapters are not shown in the schematic. The signal is afterwards digitized and further processed on the FPGA.*

Inside the setup: 3K stage

The signal from the resonator first passes through an isolator that blocks the source signal from 300 K and 30 K blackbody radiation. The isolator attenuates the thermal radiation by about 19 dB, while the signal traveling upwards is attenuated by less then 0.5 dB. The signal is then linearly amplified by a low noise high electron mobility transistor (HEMT) amplifier. The gain and the noise temperature of the HEMT at cryogenic temperatures are crucial for the SNR and their measurements will be described in sections 6.2 and 6.4. For the HEMT and the isolator a heat shield was designed that can be placed on top of the 3 K stage. The HEMT and the isolator are also thermalized with the 3 K stage via the heat shield, whose CAD design can be seen in Figure 6.2. A copper-stainless-steel cable leaves the box through a small hole and guides the amplified signal out of the setup and to the down conversion board.

Components of the analog amplification and detection system

	Component	Producer: official name	Frequency range	Max. input power
b)	Isolator	Pamtech: PTH1827KI	18-26.5 GHz	?
c)	HEMT amplifier	Caltech: 40A108 or 40A116	11-26 GHz	?
d)	UMS1 amplifier	UMS: CHA3689-99F	12.5-30 GHz	14 dBm
e)	High pass filter	Marki: FH-1800	12.5-30 GHz	1 W
f)	Low pass filter	Marki: FLP-2650	DC - 26.5 GHz	1 W
g)	UMS2 amplifier	UMS: CHA3689-99F	12.5-30 GHz	14-15 dBm
h)	Mixer	Marki: M8-0326	3-26.5 GHz	2-8 dBm
i)	Low pass filter	Minicircuits: SLP - 50+	DC - 48 MHz	0.5 W
j)	ZFL amplifier	Minicircuits: ZFL-500LN+	0.1-500 MHz	5 dBm
k)	Low pass filter	Minicircuits: SLP - 50+	DC - 48 MHz	0.5 W

Table 6.1.: *Overview over the components in the amplification system. The numbers are obtained from the relevant data sheet. For the amplifiers the maximal input power specified is the 1 dB compression point, whereas it is directly specified for the filters. For the mixer the maximal input power depends on the LO power.*

Down conversion board

At the input of the down conversion board there is a DC-block to avoid disturbing the signal with the potentials applied to the amplifiers of the down conversion board. The signal is first amplified by the UMS1 amplifier, then high pass and low pass filtered by Marki filters to again be amplified by a amplifier of the same type as the first - the UMS2 amplifier. In order to damp standing waves, a 10 dB attenuator has been placed at the input of the UMS2 amplifier. The amplified signal passes through a copper cable at the back of the board via another 10 dB attenuator to the RF input of the mixer. The 10 dB attenuator cancels further standing waves and can be replaced by a 3 dB attenuator if a higher signal amplitude gets more important than the flatness of the spectrum.
The Mixer has three ports: RF, LO and IF. The incoming signal (RF) with frequency ν_{RF} is mixed with the local oscillator signal (LO) at a frequency $\nu_{LO} = \nu_{RF} + 25$ MHz. The output (IF) is made up of difference and sum frequencies of ν_{RF} and ν_{LO}, but mainly consists of the difference signal ν_{IF} at 25 MHz. The down converted signal is then low pass filtered, amplified and again low pass filtered. The SLP lowpass filters suppress leaking signals from the RF and LO ports. The amplification is done with a Minicircuits low noise ZFL 500 amplifier. The IF signal then leaves the down conversion board, passes through a DC-block and is then digitized and recorded for further analysis on the FPGA.
The down conversion board is assembled on a two level setup as depicted in Figure 6.3. DC-Blocks are used on all inputs to avoid influencing the signal outside of the DCB with the applied potentials. The two UMS amplifiers need a bias voltage of 4 V and 0 V. The 0 V output should also be connected to the earth of the current source as there is else wise a potential of 2 V (compared to ground) on the surface of the UMS amplifiers. The resulting supply current for both amplifiers connected is 220 mA. The ZFL amplifier needs 15 V and 0 V, resulting in a supply current of about 50 mA.

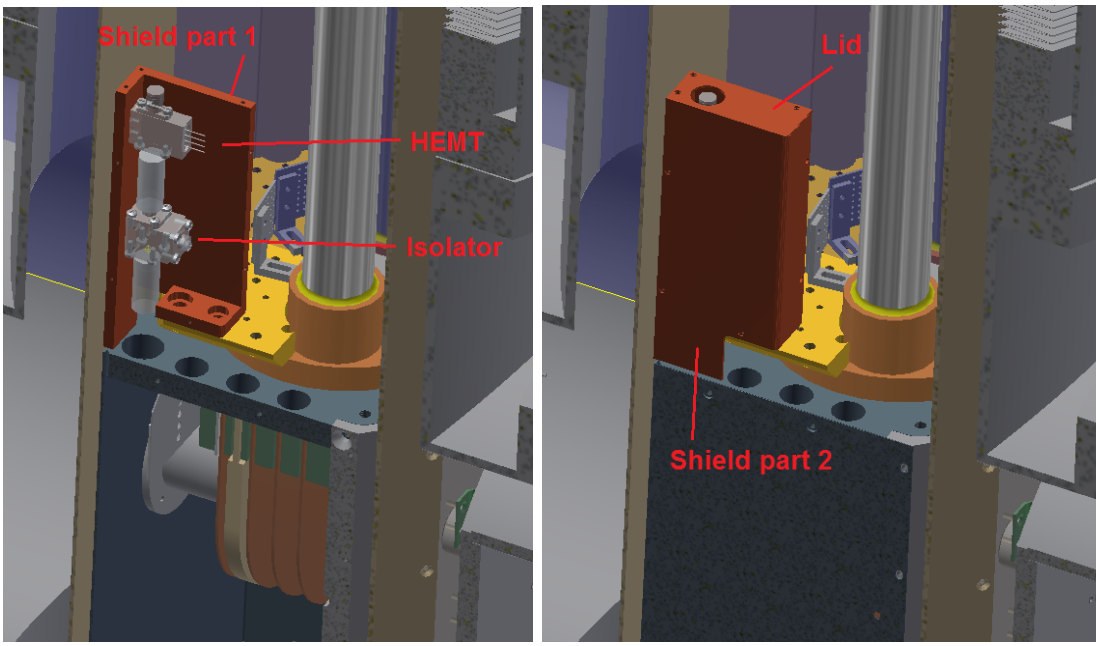

Figure 6.2.: *CAD model of the box for the isolator and the HEMT inside the setup. The box is mounted on top of the 3K stage (yellow). Left: The HEMT and the isolator fastened to the holder without the shielding and the lid. The electrodes can be seen below. Right: The box with shield and closed lid.*

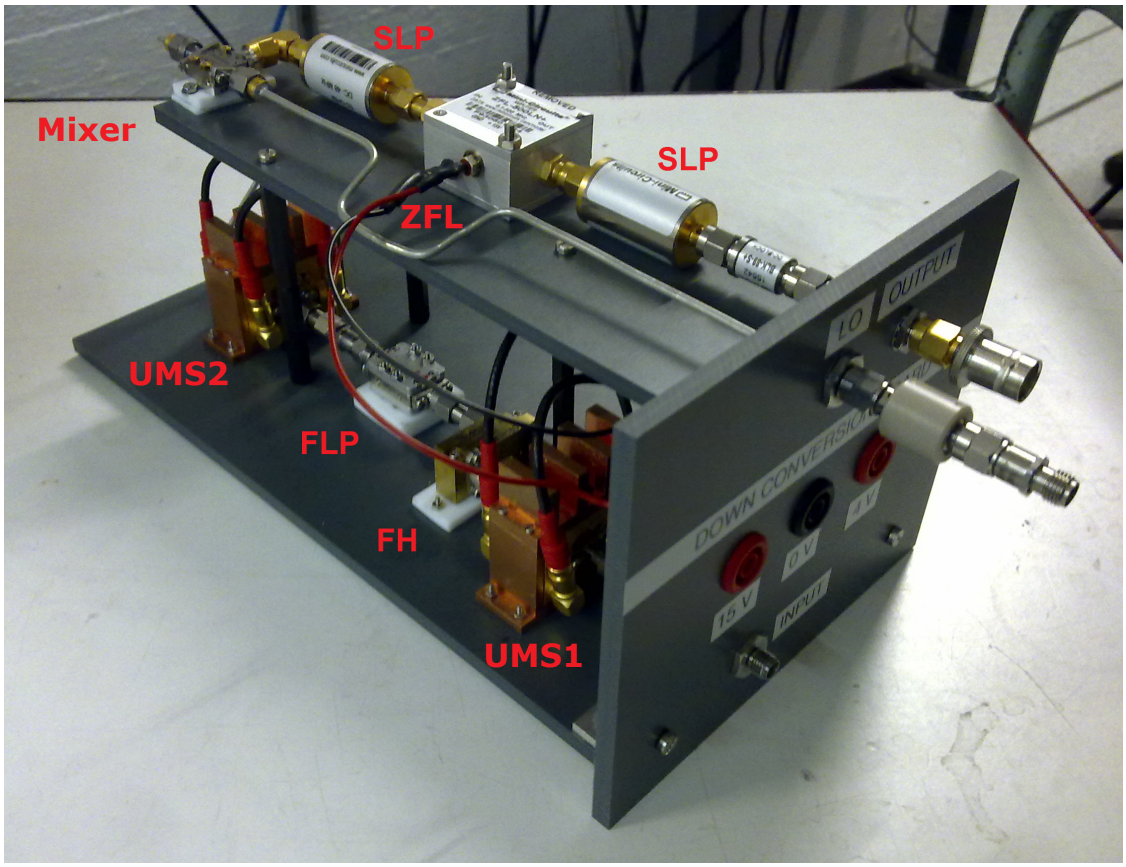

Figure 6.3.: *Photograph of the down conversion board.*

6.2. Gain of the amplifiers

6.2.1. Measurements at 300 K

The gain of the amplifiers at room temperature can be directly measured with the network analyzer. The amplifiers are connected via two cables (which are part of the calibration) to the network analyzer and the S21 parameter is recorded. For the frequency range we choose the range in which the amplifiers are operated in experiments. This is between 18 and 26 GHz for all amplifiers except the ZFL, which operates between 10 and 500 MHz. For the warm measurements of the two HEMT amplifiers, the default voltages are chosen: $V_{Gate1} = V_{Gate2} = V_{Gate} = 1.6$ V and $V_{Drain} = 1.2$ V. The VNA source power is -20 dBm, which is below the 1 dB compression point for all amplifiers except the two HEMTs. We hence put a 20 dB attenuator at the input of the HEMT amplifiers and later subtract its S21 curve from the measured S21 parameter of the combined system to obtain the gain of the HEMT. An overview of the gain measurements is given in Figure 6.4.
The HEMT amplifiers have a flat gain curve, varying by less then 1 dB. The gain of the HEMT116 is around 1.3 dB higher than that of the HEMT108 - for the same applied voltages. The gain curves of both UMS amplifiers show a strong frequency dependence and a steep drop at 22 GHz. This feature contributes some artefact to the the noise temperature measurements and is visible in the gain curve of the down conversion board. The gain of the ZFL fluctuates between 28.4 and 28.9 dB. All the gains are as specified in the data sheets.

6.2.2. Measurements at 14 K

The low noise HEMTs from Caltech are cryogenic low noise amplifiers and one of them will be mounted in a heat shield box on the 4 K stage. We are therefore interested in the gain at low temperatures and perform a dip stick measurement with liquid helium, in which the HEMT is kept in a stainless steel vacuum tube with an opening at the bottom where the HEMT can be fastened to a copper bar. On top of the copper bar is a temperature sensor. Two copper cables as well as the wires for the voltages lead from the top flange down through the dip stick to the amplifier. With everything connected, the opening can be closed, the dip stick evacuated and lowered slowly into the helium dewar. The temperature sensor tells us when the minimum temperature - 14 K for both HEMTs - is reached. We then measure the S21 parameter using the network analyzer. This time we insert 40 dB attenuation at the input to the dip stick. In order to obtain the gain of the amplifiers, we have to subtract the S21 parameter of the attenuators and the cables leading to and from the HEMT inside the dip stick. We measure this S21 parameter in a separate dip stick measurement (see Figure 6.5) and thus obtain the correct value at 14 K. We applied a potential of 1.9 V to the two gates and a potential of 0.8 V (HEMT108), respectively 1 V (HEMT116), to the drain, while the ground was connected to the ground of the current source. The gain of the amplifiers is specified for these settings on the data sheets. The gain we measured is plotted in Figure 6.5 and is a slightly higher than specified.

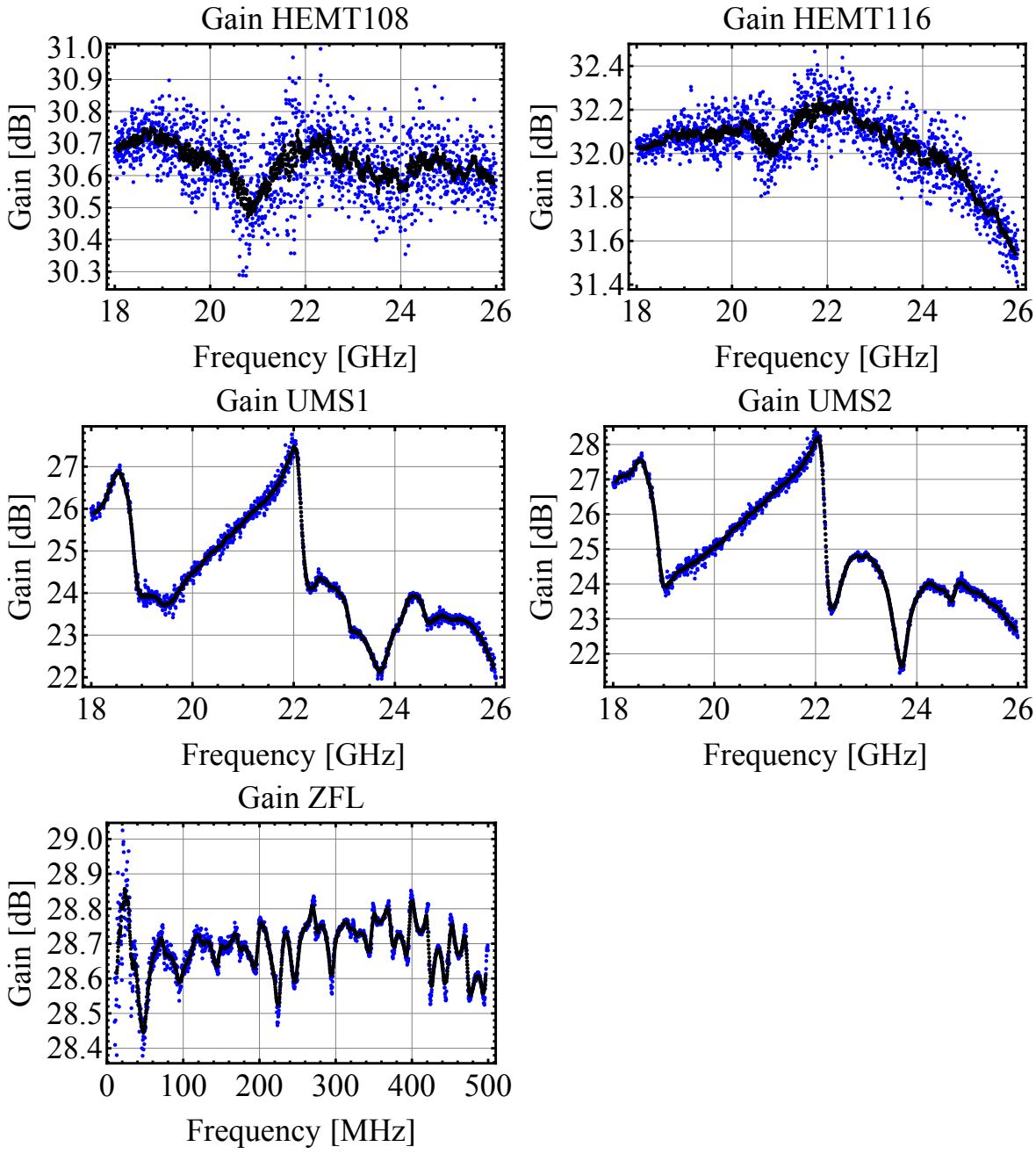

Figure 6.4.: *The gain of the different amplifiers measured at room temperature. The blue points are the values measured with the network analyzer. The black curve shows the moving average over 20 points. For the two HEMTs a 20 dB attenuator was used in order to be below the compression point. The gain of the HEMTs was calculated by subtracting the S21 parameter of the attenuator from the one of the HEMT for each frequency.*

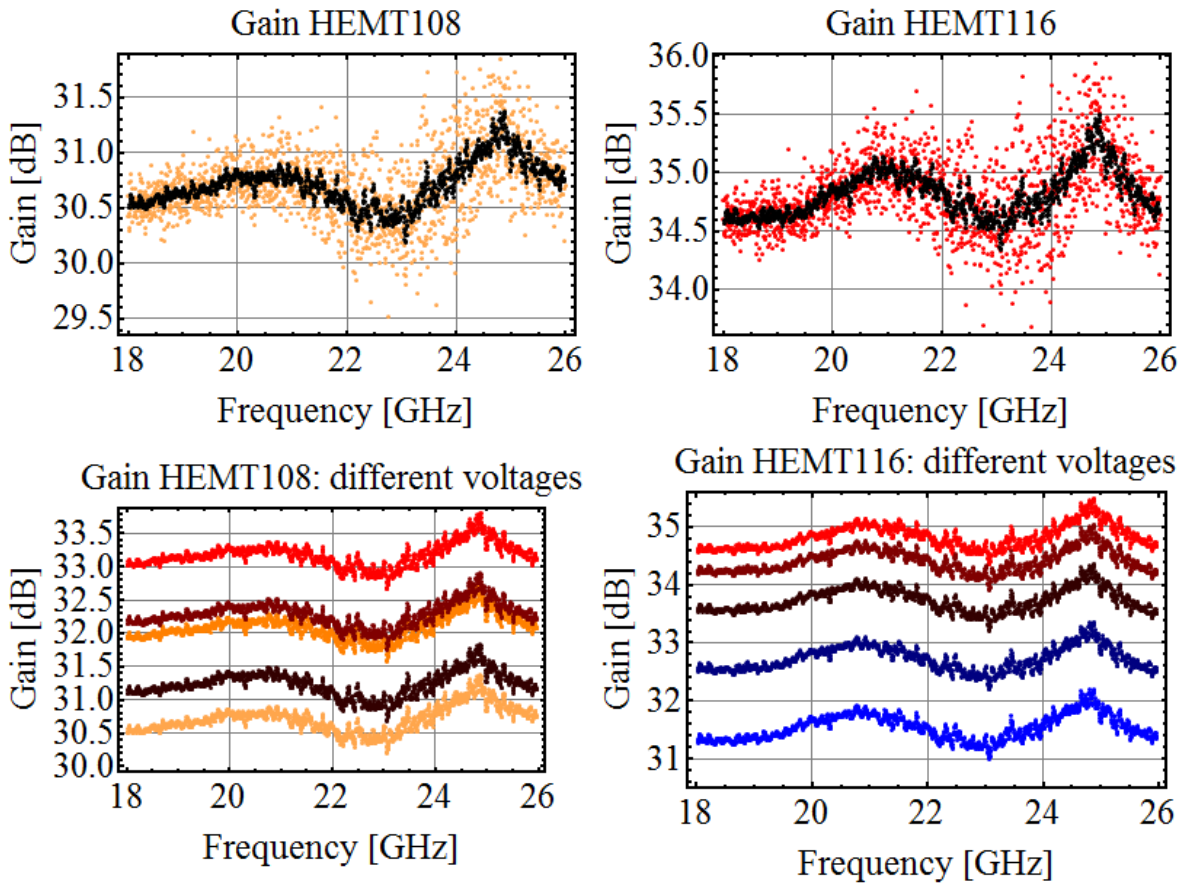

V_D \ V_G [V]	1.7	1.8	1.9
0.8	x		x
0.9	x		x
1.0	x	x	x

Figure 6.5.: *Gain of the HEMT amplifiers at 14 K. The color code for the different voltage combinations is given in the table at the bottom. Top: The colored points are the values measured with the network analyzer. The black curve shows the moving average over 20 points. Middle: Gain (moving average) of the HEMT amplifiers with different voltage settings.*

6.2.3. Influence of the applied gate and drain voltages

The gain of the amplifiers depends on the applied potentials. We therefore varied the default voltages around the values given on the respective data sheet in steps of 0.1 V and measured the gain of the amplifier for each configuration. The frequency dependence of the curve does not change; the curve merely shifts vertically. This can be seen nicely in Figure 6.5 for the 14 K measurement, where the different voltage combinations are given with a color code. We can now also see that even for the same voltage combinations, the HEMT116 has a higher gain than the HEMT108. In the warm measurements we have done the same in the frequency range between 10 and 26 GHz. The gain was then averaged over this range and plotted in Figure 6.6 as a function of the gate voltage. We see that the gain varies approximately linearly with the gate voltage. A higher gate or drain voltage leads to a higher gain.

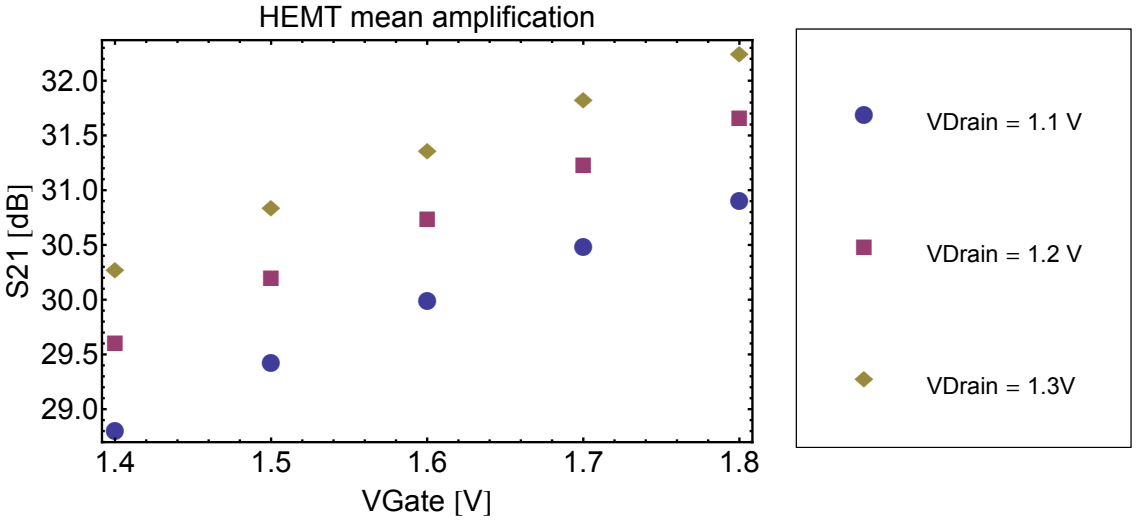

Figure 6.6.: *Mean gain of the HEMT108 amplifier for different drain and gate voltages at room temperature. The mean is taken over the frequency range 10 to 26 GHz.*

6.3. Spectrum of the down conversion board

The gain curve of the down conversion board can not be obtained from a two-port measurement with the network analyzer as the mixer has three ports: the local oscillator (LO), the RF input and the IF output. We can however measure the spectrum using two microwave generators (one for the LO and one for the RF input signal) as well as the digital down conversion and the FPGA to process the IF output. We can control and display the measurement in the LabView program CleanSweep.

In order to measure the gain curve, we need to know the power at the RF input P_{in} and the power at the output P_{out} of the down conversion board. To know P_{in} we simply need to subtract the microwave cable losses from the nominal power set at the microwave generator. For P_{out} we can neglect cable losses at 25 MHz frequency, but we need to take the analog-to-digital conversion (ADC) and the filters on the FPGA into account. We do this with a

calibration using an arbitrary waveform generator (AWG) and generate a sin curve with a frequency of 25 MHz. The output signal of the AWG can be measured with an oscilloscope and has a peak to peak voltage of 149 mV. The same signal is displayed with a voltage of 30.36 mV in CleanSweep. Using these numbers values, we can translate the measured signal amplitude in CleanSweep V_{CS} back to the output power P_{out} at the exit of the DCB:

$$P_{out} = \frac{1}{2 \cdot 50\Omega} \left(V_{CS} \frac{149mV/2}{30mV} \right)^2 . \tag{6.1}$$

After the calibration we connect the down conversion board LO and RF input to the two microwave generators and the IF output to the cable leading to the FPGA. In order to be below the compression points of the amplifiers and in the optimal range of the ADC and the FPGA, we insert 90 dB attenuation at the input of the DCB. We then take a spectrum by sweeping the RF input frequency ν_{RF} from 15 GHz to 30 GHz. The LO frequency is swept at the same time at a frequency $\nu_{LO} = \nu_{RF} - 25$ MHz. For the LO a power of 13 to 16 dBm at the input of the mixer is used. The input power P_{in} at the down conversion board can be obtained by subtracting the S21 parameters of the cable and the attenuators from the input power of 16 dBm specified at the microwave generator. The S21 parameter of the down conversion board can now be received by subtracting the the input power P_{in} in dBm from the output power P_{out} in dBm.

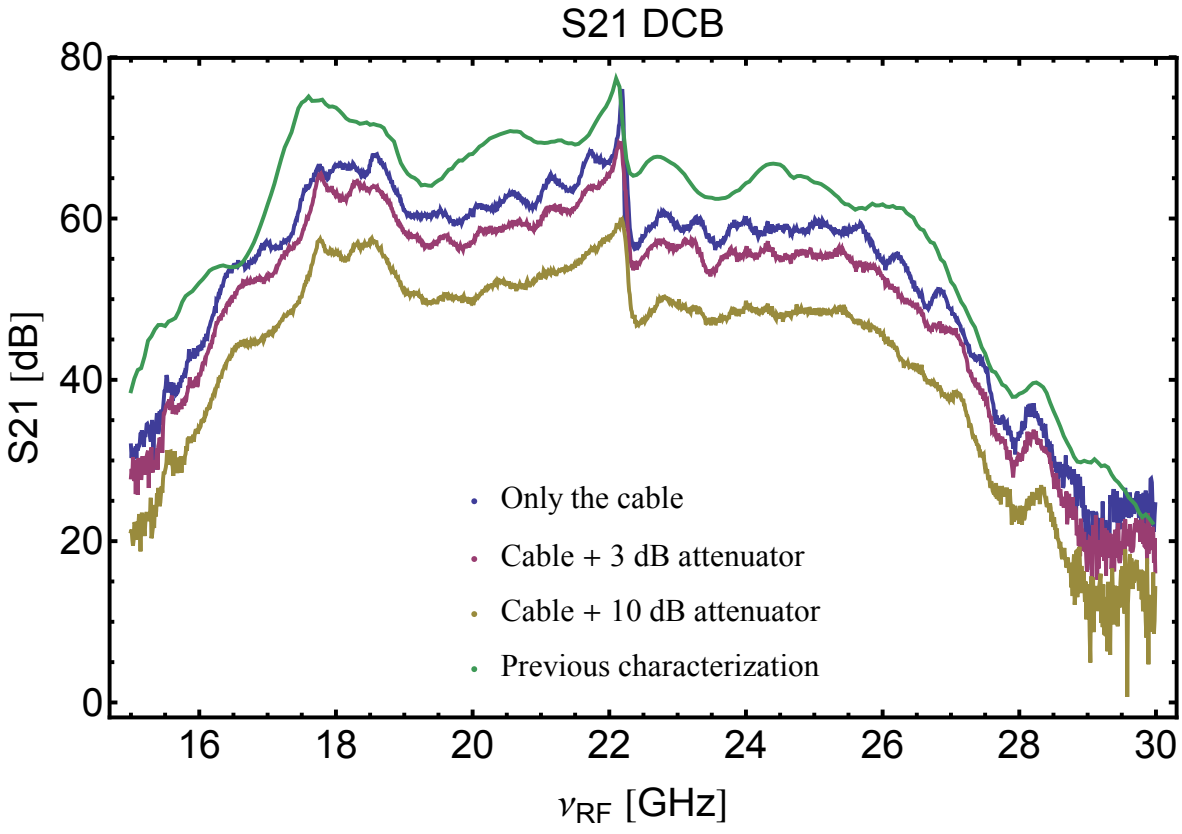

Figure 6.7.: *Spectrum of the down conversion board for 3 different configurations and a previous characterization for comparison.*

In this way we measure 3 different configurations of the down conversion board and the results are plotted in Figure 6.7. The configurations differ in the attenuator attached to the RF input of the mixer. In the first configuration there is only the cable connecting the mixer and the UMS2 output. We find standing waves in the spectrum (see the blue curve of Figure 6.7), especially just before the dip at 22 dB caused by the UMS amplifiers. If we insert a 3 dB attenuator, the standing waves get damped (purple curve). For an even higher attenuation of 10 dB, the standing waves disappear, but the gain of the DCB is also, as expected, 7 dB lower (yellow curve) as for the purple curve. As a comparison, we also show a curve measured for the previous configuration of the down conversion board, where it was on one level with no cable or attenuator at the back and two 3 dB attenuators in between the UMS amplifiers instead of the 10 dB attenuator. The cable at the back has an attenuation of 1 to 2 dB, meaning that the gain of the DCB in the blue configuration is 5 to 6 dB lower than in the previous configuration (green). Depending on the necessary amplification, it can make sense to choose a lower attenuation in exchange for a less flat gain curve with standing waves.

Measuring the cavity modes with the DCB

With its spectrum being recorded, we can use the down conversion board to measure the S21 transmission curve of a 3D cavity. Cavity 4B is placed in between the microwave generator and the attenuators at the input of the DCB. It is necessary to place some of the attenuators in front of the cavity, as this prevents standing waves between the microwave generator output and the cavity input. The spectrum of the cavity with the DCB is taken in the same way and with the same settings as for the DCB. The power at the output of the DCB is again calculated using formula (6.1). Since we are using the same input power, we simply subtract the output power of the DCB measurement from the output power of the measurement with the cavity. This results in the cavity spectrum, which is then analyzed in the same way as described in section 4.1 for the network analyzer measurements. The S21 curve of the coupling cable is subtracted from the data, which is then fitted with a Lorentzian to obtain the resonance frequency ν, the width $\delta\nu$ and the quality factors. The first four modes (blue) with their fits (red) are plotted in Figure 6.8 along with the data measured with the network analyzer (purple) for comparison. We can see that the two curves match well for all the modes except the first one. Also the fit parameters are very similar. The curve for the first mode has its peak above zero, which means that we overestimate the transmission of the cavity and thus get a negative internal quality factor. This problem may arise due to standing waves or the drop in the spectrum of the down conversion board between 18.5 and 19 GHz and needs to be investigated further. The down conversion board can be successfully used to obtain the resonance frequency ν, the width $\delta\nu$ and the quality factor Q.

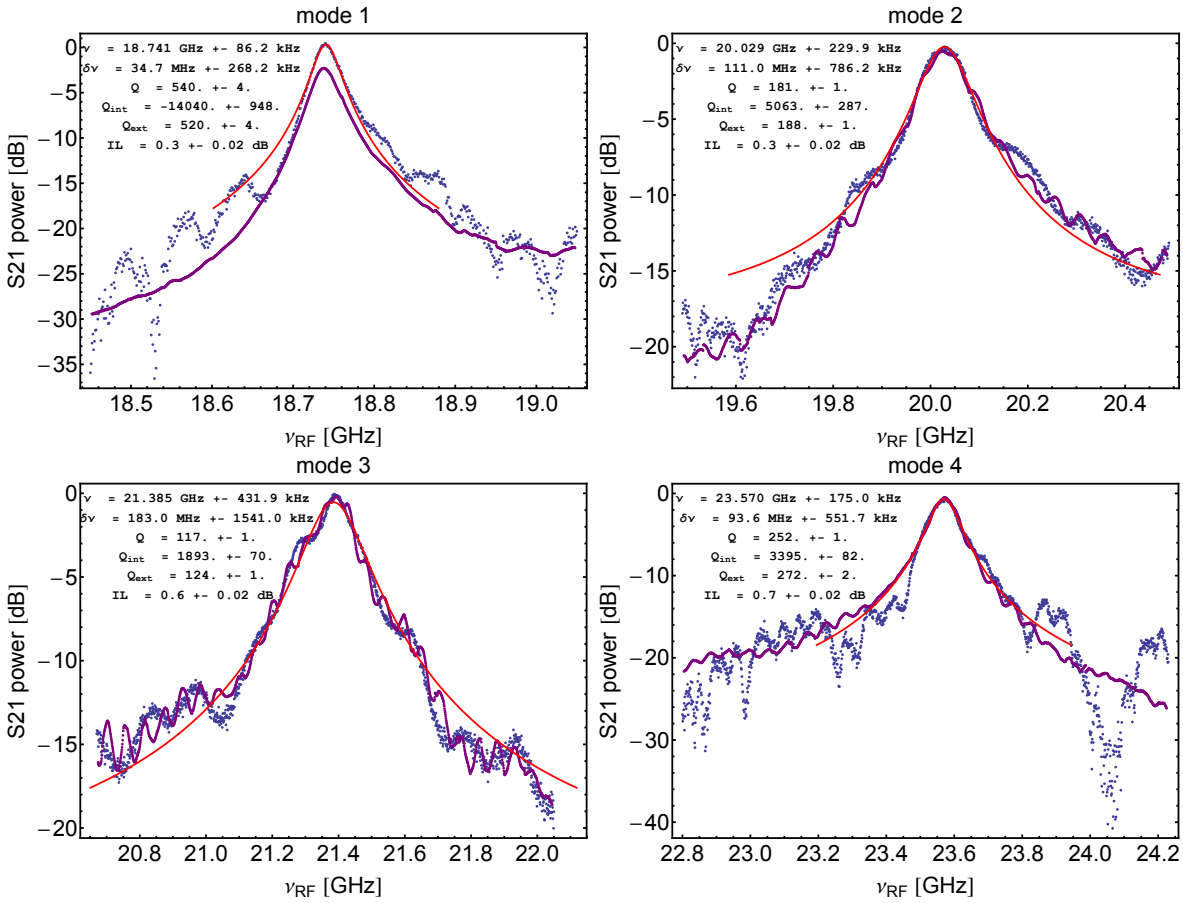

Figure 6.8.: *The first four cavity modes measured with the DCB (blue) and the VNA (purple). The modes of the DCB measurement are fitted with a lorentzian function (red) and resonance frequency and quality factors are determined.*

6.4. Noise temperatures of the amplifiers

In this section we describe the Y-factor method, which is used to determine the noise temperature of the UMS1, the UMS2, the ZFL and the two HEMT amplifiers. We will then describe the actual experimental setup and the measurement results. The noise temperatures of the UMS1, UMS2 and the ZFL amplifiers are measured at room temperature while the HEMT amplifiers are measured in a dip stick experiment in liquid helium. This corresponds to the temperatures the amplifiers will later be used at. We will look at the warm and the cold measurements separately as their experimental setups differ. At the end of the section we discuss possible error sources and describe an improved noise temperature measurement for the HEMT at around 10 K.

Y-factor method

The Y-factor method allows us to determine the equivalent noise temperature T_e of an amplifier with gain G. For the measurement we connect a matched load to the input of the amplifier and then measure the noise power at the output with a spectrum analyzer. This is done for two different temperatures T_H and T_C of the load and results in the noise powers N_H and N_C. The measured noise powers can be described using formula (2.70):

$$N_H = Gk_BB\left(T_H + T_e\right) \tag{6.2}$$

$$N_C = Gk_BB\left(T_C + T_e\right), \tag{6.3}$$

where B is the bandwidth of the spectrum analyzer and k_B the Boltzmann constant. We can now define the ratio of the two noise powers as Y:

$$Y = \frac{N_H}{N_C} = \frac{T_H + T_e}{T_C + T_e} > 1 \tag{6.4}$$

and rearrange the equation for T_e to get

$$T_e = \frac{T_H - YT_C}{Y - 1}. \tag{6.5}$$

In order to obtain an accurate result, the two temperatures T_H and T_C should be far apart.

6.4.1. Room temperature measurement: UMS1 and UMS2

We will first look at the room temperature measurements of the similar amplifiers UMS1 and UMS2 which will be measured in exactly the same way.

Measurement setup

For the warm measurements the Y-factor method is implemented using room temperature for T_H and liquid nitrogen temperature for T_C. We use a 50 Ohm termination (4800-7001-02-Cryo)

as a matched load and connect it via a copper-steel cable to the input of the UMS amplifier we want to measure. The UMS amplifier is then connected to the measurement system which consists of another amplifier and a spectrum analyzer. The second amplifier increases the noise signal we want to measure. We will refer to the UMS amplifier whose noise temperature we want to measure as the "UMS" amplifier, while the second amplifier "Amp" does not get the UMS tag and belongs to the measurement system. For the cold measurement the load is dipped into liquid nitrogen ($T_C = 77$ K), while it is simply kept in air for $T_H = 300$ K For the measurement of N_H the liquid nitrogen is simply left away. The setup is schematically shown in Figure 6.9.

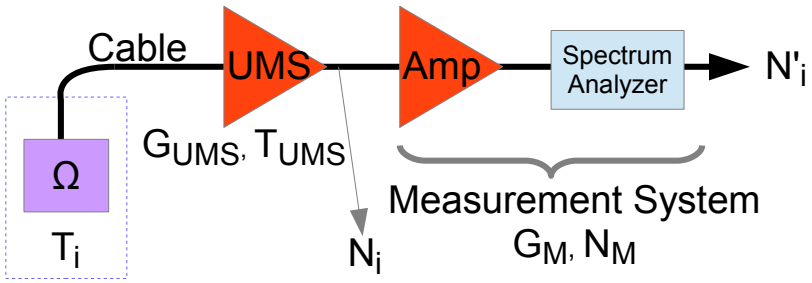

Figure 6.9.: *Schematic of the noise temperature measurement of an amplifier with gain G_{UMS} at room temperature using a load, which is also at room temperature for $T_i = T_H$ and cooled in liquid nitrogen for $T_i = T_C$. The measurement system contains the spectrum analyzer and another amplifier "Amp" to increase the signal.*

Spectrum analyzer settings

The noise temperature is frequency dependent and we therefore measure the noise power over the useful frequency range of the down conversion board (18-26 GHZ). We take 8001 sample points in equidistant steps of 1 MHz and also use 1 MHz for the resolution and the video bandwidth. The bandwidth B in the measurement is thus 1 MHz. The spectrum analyzer performs a continuous sweep and averages over 20 sweeps. Using a GPIB connection, the data is read out with the labview program "E4407B Spec Analyzer Get Trace.vi".

Noise of the measurement system

We can not measure the noise N_C of the UMS amplifier with the cold load directly after the amplifier, but have to take the noise of the measurement system into account. The same is true for the noise N_H with the hot load connected. The noise N' we measure with the spectrum analyzer is the sum of the noise N we want to measure and the noise of the measurement system N_M. Both N and N_M are amplified by G_M:

$$N_i' = G_M\,(N_i + N_M) \quad \Rightarrow \quad N_i = \frac{N_i' - N_M}{G_M}, \tag{6.6}$$

where N and N' get the suffix C or H depending on the temperature of the load. Since we want the ratio Y of the noise power with the hot load and the noise power with the cold load, the gain G_M does not need to be measured:

$$Y = \frac{N_H}{N_C} = \frac{N'_H - N_M}{N'_C - N_M}. \tag{6.7}$$

Taking a closer look at the origin of the measurement system noise, we see that the spectrum analyzer creates a lot of noise. It has a noise temperature between 50'000 K and 140'000 K (see Figure 6.10 on the left). This result can be easily obtained by measuring the noise power of the spectrum analyzer with the 50 Ohm termination connected and using equation (2.69) to convert it into the equivalent noise temperature. The small amount of additional noise from the load at 290 K can be neglected. If we now connect the second amplifier as shown in the schematic in Figure 6.11, the measurement system consisting of the second amplifier and the spectrum analyzer can be described with an effective noise temperature T_M. This noise temperature is reduced compared to the one of the spectrum analyzer alone, since we divide by the gain G_M of the measurement system to get the noise temperature:

$$T_M = \frac{N_M}{k_B \cdot B \cdot G_M}. \tag{6.8}$$

We arrive at an effective noise temperature of the measurement system between 400 K and 1000 K as can be seen in the Figure 6.10 on the right). Using this measurement setup, the measurement noise power N_M we subtract from N'_i amounts to less then 10% of the measured noise signal. For low frequencies up to 22 GHz the noise of the measurement system would be neglectable.

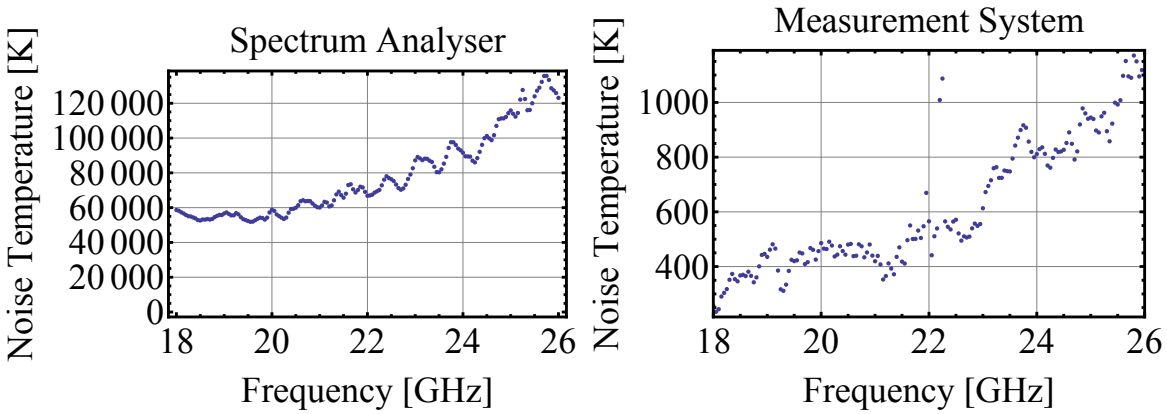

Figure 6.10.: *Noise temperature of the spectrum analyzer and the measurement system.*

The effect of the lossy cable

Another important issue is the cable between the load and the UMS amplifier we want to measure. The cable is necessary to keep the UMS amplifier at room temperature while the load is immerged into liquid nitrogen. The transition through the lossy cable affects the

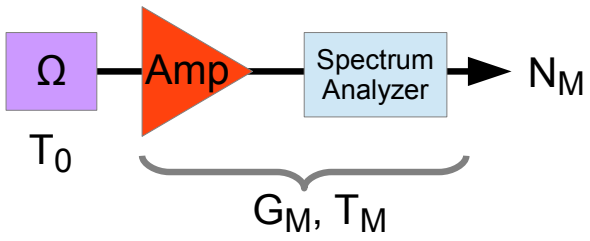

Figure 6.11.: *Schematic for the determination of the measurement system noise.*

temperature. We can calculate the temperature T_{in} at the input of the amplifier after passing through a cable at temperature T_W with:

$$T_{in} = \eta\left(T_W\right) \cdot T_\Omega + \left(1 - \eta\left(T_W\right)\right) \cdot T_W, \tag{6.9}$$

where $\eta\left(T_W\right) = \left|S_{21}\left(T_W\right)\right|^2$. In the case of the hot load, all components (load, cable and amplifier) are at room temperature, meaning that $T_W = T_\Omega = T_H = T_{in}$. In the case of the cold load, there is a temperature gradient over the cable. The load is at $T_\Omega = T_C = 77K$, as is half of the cable, which is immerged into liquid nitrogen. The other half of the cable is outside. We assume a linear temperature dependance over that part of the cable and assign the whole cable an average temperature of

$$T_W = \frac{1}{2} \cdot 77K + \frac{1}{2} \cdot \frac{T_H - 77K}{2}. \tag{6.10}$$

We then apply formula (6.9) as if the whole cable was at temperature T_W with the corresponding $\eta\left(T_W\right)$. The S_{21} parameter of the cable can be conveniently measured at room temperature and at 77 K - the corresponding η is plotted in Figure 6.12. For the temperatures in between we use a linear interpolation of $\eta\left(T_W\right)$. These assumptions do not have to reflect the reality and we therefore choose to put a generous error bar of ±30 K on the temperature of the cable.

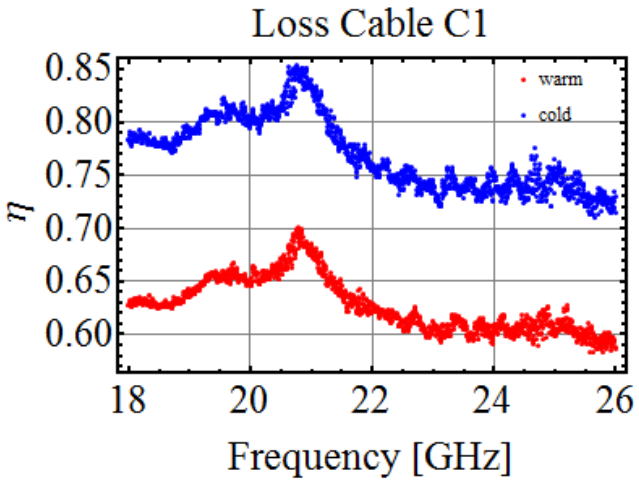

Figure 6.12.: *Loss of the cable between the load and the HEMT. The red curve is measured at room temperature, while the blue curve is obtained by dipping the cable into liquid nitrogen.*

Results

The noise temperatures of the UMS1 and the UMS2 amplifiers obtained with the described method can be seen in Figure 6.13. It is around 200 K, which corresponds to the values specified.

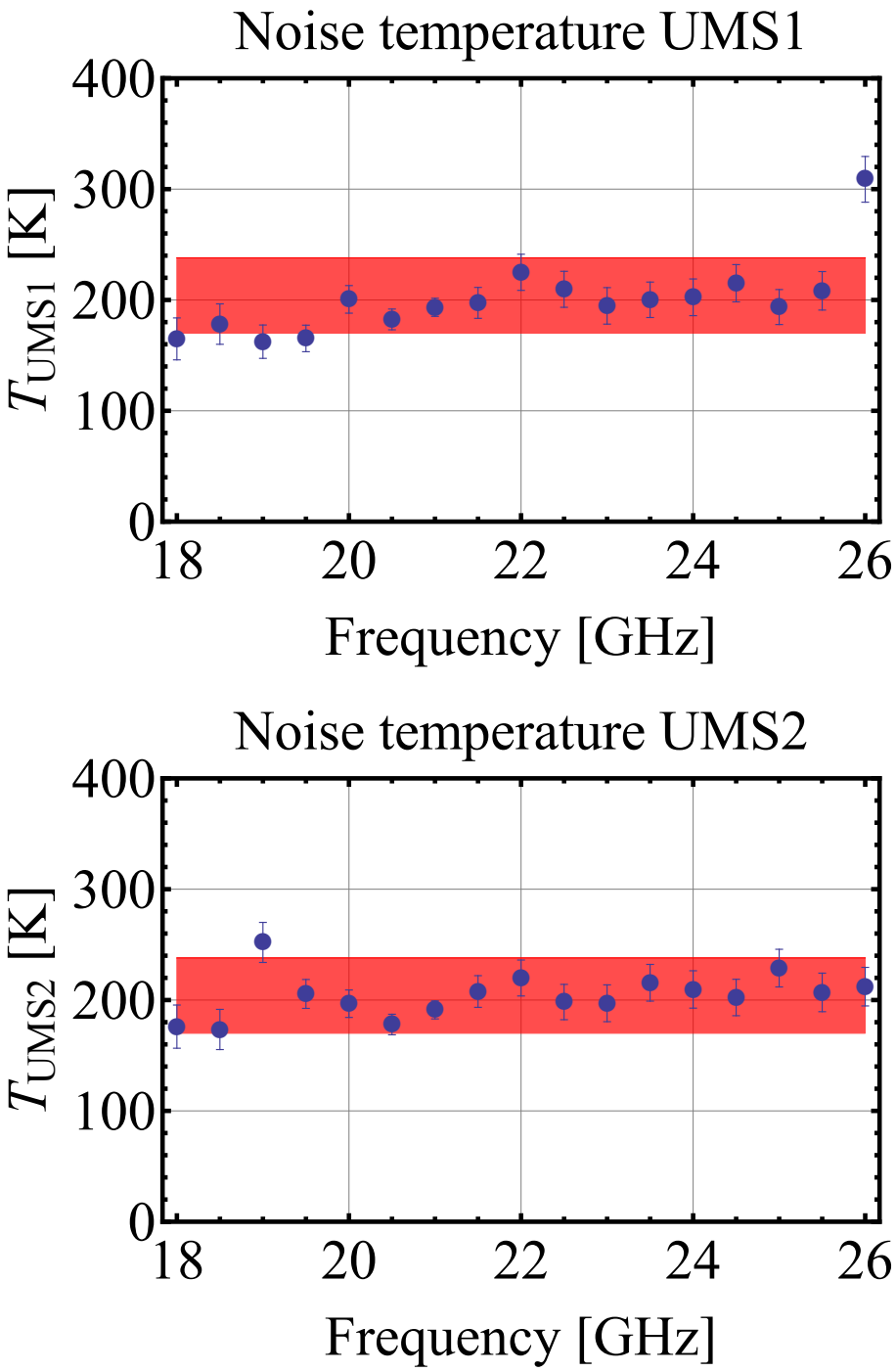

Figure 6.13.: *Noise temperature of the UMS amplifiers. The blue dots were obtained in the measurement. The red bar indicates the noise temperature range specified on the data sheet.*

6.4.2. Room temperature measurement: ZFL

The noise measurement of the ZFL amplifier can be done in the same way as for the UMS amplifiers. There are however two main differences. First the frequency range of the ZFL amplifier is different, meaning that other settings have to be used on the spectrum analyzer. Second, no other amplifier is placed between the amplifier we want to measure and the spectrum analyzer. The gain of the measurement system does not influence the formulae used and we can thus obtain the noise temperature of the ZFL amplifier in exactly the same way. The impact of the measurement system is however bigger: the noise power of the measurement system N_M contributes with up to 25% of N' instead of less than 10% with an additional amplifier. This results in higher error bars for the noise temperature of the ZFL amplifier.

Spectrum analyzer settings

The frequency range is set to 10 MHZ to 500 MHz using 4901 sample points results in 10 kHz steps. We take these 10 kHz also as the resolution bandwidth and as the video bandwidth meaning that we have a bandwidth B of 10 kHz. The rest of the settings are the same as for the UMS amplifiers.

Results

The noise temperature we obtain with this procedure is very similar to the one of the UMS amplifiers and can be seen in Figure 6.14. The noise temperature specified on the data sheet is however higher: 275K to 290 K.

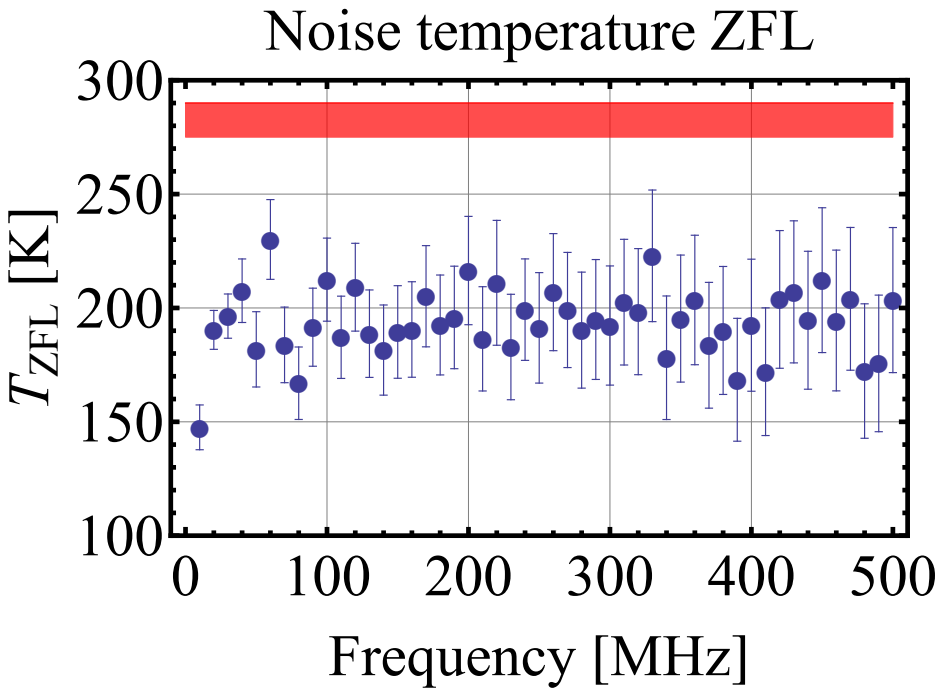

Figure 6.14.: *Noise temperature of the ZFL amplifier. The blue dots were obtained in the measurement. The red bar indicates the noise temperature range specified on the data sheet.*

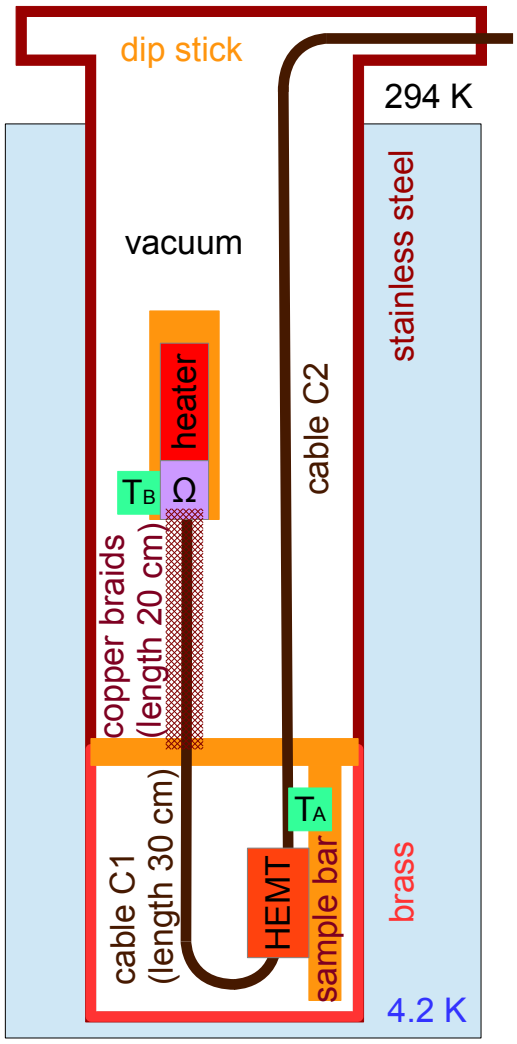

Figure 6.15: *Schematic of the dip stick noise temperature measurement. The load Ω is pressed into a copper block screwed to the same copper plate as the heater. A temperature sensor measures the temperature T_B of the load, whose temperature can be regulated with the heater. In order to cool the load down to low temperatures, a weak thermal link consisting of 4 copper braids is installed. The copper braids are fastened at one end to the load and the other to the dip stick base (see also Figure 6.16). The noise from the load passes through the copper-steel cable C1 to the HEMT. The HEMT itself is thermalized with the sample bar, which is fastened to the base of the dip stick. Here the temperature T_A of the HEMT can be measured. The copper cable C2 leads from the HEMT to the output of the dip stick. The dip stick itself is evactuated and immerged into liquid helium.*

6.4.3. Dip stick measurement: HEMT108 and HEMT116

In order to obtain the noise temperature of the two HEMT amplifiers at low temperatures, we perform a dip stick measurement in liquid helium. Same as for the warm measurements, the noise level is measured for two different load temperatures. The load inside the evacuated dipstick cools down slower than the HEMT, which is thermalized with a copper bar to the cold dip stick wall. This means that we can measure the noise power N_H at different temperatures T_H during the cool down, while the HEMT is already at around 10 K. When the temperature of the load stabilizes, the noise power N_C for the temperature T_C can be measured. The load can also be heated with the heater resulting in a second measurement set for comparison. The measurement setup inside the dip stick can best be understood in the schematic in Figure 6.15 and the photos in Figure 6.16. The measurement principle and also the formulae are the same as for the UMS measurements.

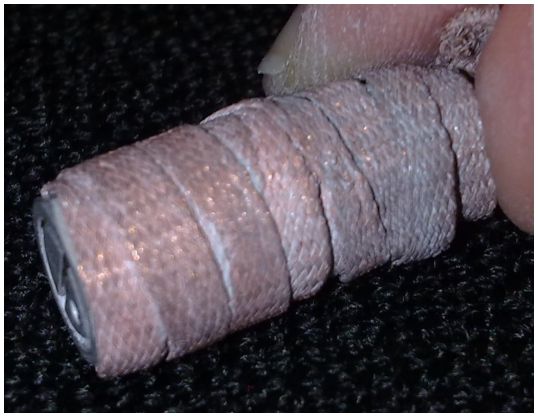

(a) *First the 50 Ohm termination is covered in white heat conduction paste and a flat copper braid is wrapped tightly around it.*

(b) *Next the whole construction is pressed into a copper block for thermalization. The end of the copper braid is screwed to the top to prevent the braid from unwrapping itself again.*

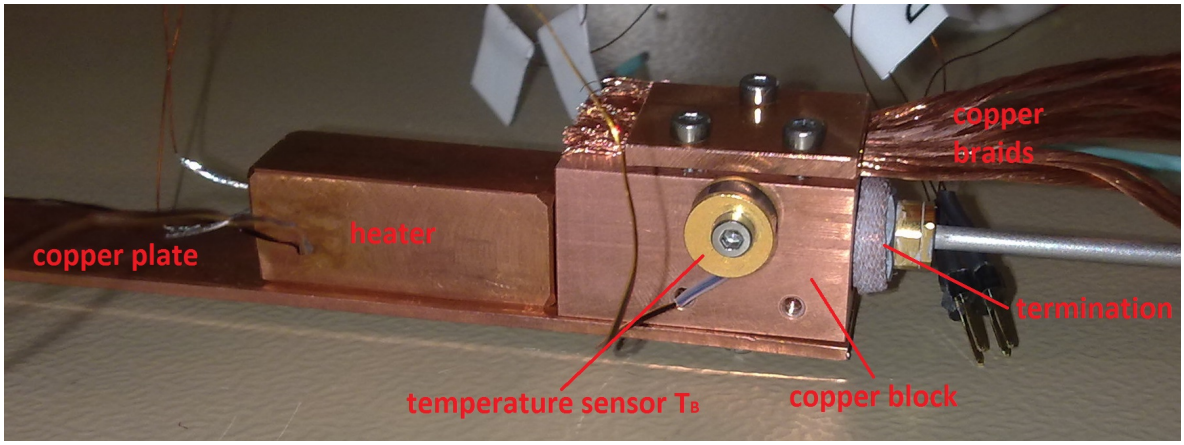

(c) *The copper block is then screwed to a copper plate. The heater, which was pressed into another copper block before, is also screwed to the copper plate. The temperature sensor measures temperature T_B. For additional thermalization of the load, 4 copper braids of 2 mm diameter are taken. The 8 ends are pressed against the copper block using a small copper plate.*

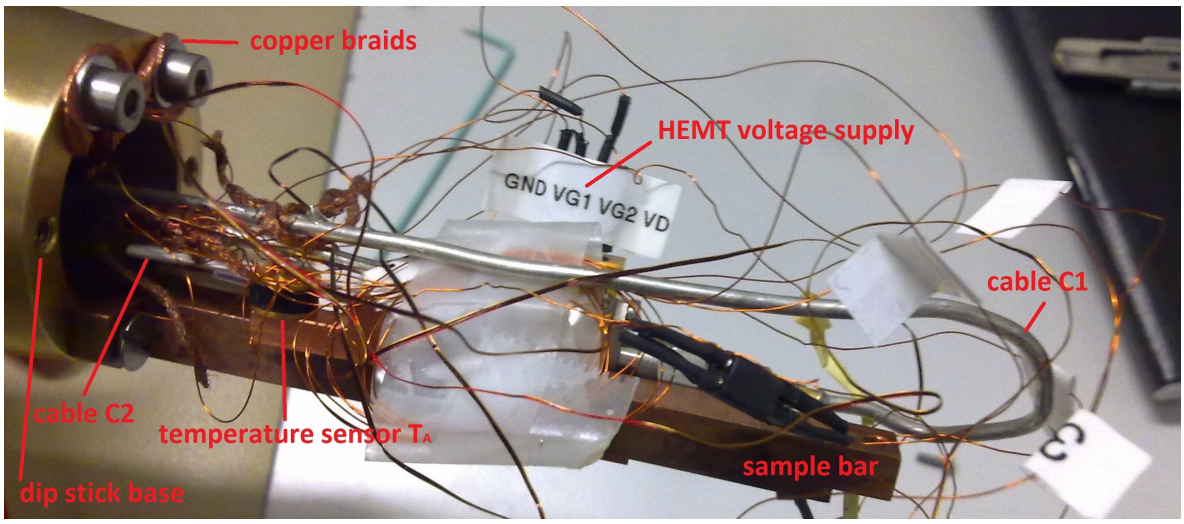

(d) *The whole construction from (c) is then inserted into the dip stick. The copper braids are fastened to the dip stick base with screws. The HEMT is screwed to the sample bar for good stabilization and thermalization. The temperature sensor on the sample bar measures the temperature T_A. The cables are connected to the HEMT.*

Figure 6.16.: *Photos of the thermalization and the setup.*

Temperature and thermalization

Two temperatures are important for our measurement. First, we need to know the temperature T_A of the HEMT, because we want to know at which temperature we determine the noise temperature of the HEMT. Second and most important, we need to know the temperature of the load T_B, since it is directly used in the formula to calculate the noise temperature.
The load is covered in heat conduction paste, wrapped tightly in flat copper braids and pressed into a copper block (see Figure 6.16). In this way we can accomplish good thermalization of the load. The temperature sensor measuring T_B is screwed directly on to the copper block. The heat from the heater flows via the copper plate to the copper block. The temperature sensor is roughly as far away from the copper plate as the load and we can assume that the temperature sensor measures the temperature of the load accurately enough.
The second temperature sensor is mounted on the sample bar, which also thermalizes the HEMT. Two processes can increase the temperature of the HEMT. First, heat can be transferred from the load via cable C1 to the HEMT. Second, heat can come from the outside of the dip stick through cable C2 to the HEMT. We assume that the brass base of the dip stick is at the lowest temperature as it is in direct contact with the liquid helium. The heat transfer $\dot{Q}$ can be described with the following formula [59]:

$$\dot{Q} = \bar{\kappa} \cdot \frac{A}{L} \cdot \Delta T = C \cdot \Delta T, \tag{6.11}$$

where $\bar{\kappa}$ is the average thermal conductivity, A the area the heat can flow through, L the length over which it is transferred and ΔT the temperature difference between the two opposite ends. The thermal conductance C is the inverse of the thermal resistance in analogy to electrical conductance. Table 6.2 summarizes the relevant parameters for the heat flow through the two cables, the 8 copper braids and from the HEMT to the base.

Part	Material	$\bar{\kappa}$ [$\frac{\mathrm{W}}{\mathrm{m \cdot K}}$] with range	A [mm^2]	L [m]	C [W/K]
Cable C1					
inner conductor	OFHC	681 (300 K to 3 K)	0.205	0.3	$4.65 \cdot 10^{-4}$
outer conductor	SS	10.2 (300 K to 3 K)	0.158	0.3	$5.37 \cdot 10^{-5}$
total					$\underline{5.19 \cdot 10^{-4}}$
Cable C2					
inner conductor	OFHC	681 (300 K to 3 K)	0.205	1.25	$1.12 \cdot 10^{-4}$
outer conductor	OFHC	681 (300 K to 3 K)	0.158	1.25	$8.61 \cdot 10^{-4}$
total					$\underline{9.72 \cdot 10^{-4}}$
8 Braids	Cu	437 (300 K to 3 K)	3.14	0.2	$\underline{5.49 \cdot 10^{-2}}$
Therm. HEMT					
Sample bar	OFHC	1955 (32 K to 3 K)	64	0.052	2.41
Plate	OFHC	1955 (32 K to 3 K)	42	0.014	5.87
total					$\underline{1.71}$

Table 6.2.: *Heat transfer estimations for the noise temperature measurement.*

We will first look at the heat coming from the load. It can flow through cable C1 via the

HEMT to the base of the dip stick or directly through the copper braids to the base. The conductance of the copper braids is more than 100 times higher than the one of cable C1. This means that almost all heat will go directly to the base via the breads and not through the cable. The base is heated which also leads to a higher temperature in the HEMT. The temperature sensor is screwed to the sample bar in between the HEMT and the base of the dip stick meaning that we can track how the HEMT is heated by the load. The HEMT is strongly thermalized with the base of the dipstick.

Now we will investigate how much cable C2 increases the temperature of the HEMT. Heat from outside flows through cable C2 directly to the HEMT, which is thermalized with the base. At equilibrium, the heat transfer from outside to the HEMT (with conductance C_{C2}) is the same as from the HEMT to the base (with conductance C_{th}):

$$C_{C2} \cdot (294K - T_{eq}) \stackrel{!}{=} C_{th} \cdot (T_{eq} - T_{base}) \,. \tag{6.12}$$

This can be rearranged for T_{eq} and simplified:

$$\begin{aligned} T_{eq} &= \frac{C_{C2} \cdot 294\ K + C_{th} \cdot T_{base}}{C_{C2} + C_{th}} \\ &\overset{C_{C2} \ll C_{th}}{\approx} \frac{C_{C2}}{C_{th}} \cdot 294\ K + T_{base}. \end{aligned} \tag{6.13}$$

In our case this means that the HEMT is 0.2 K warmer than the base because of the influence of cable C2. This does not affect the measurement.

Measurement system

In the cold experiment the measurement system consists of the two UMS amplifiers, a cable and the spectrum analyzer as shown in the schematic in Figure 6.17. The two amplifiers are again used to decrease the noise temperature of the measurement system compared to that of the spectrum analyzer. The UMS amplifiers are connected to the microwave cable C2 via the dipstick microwave port. A cable (C3) connects the amplifiers with the spectrum analyzer. All the parts outside of the dipstick form the measurement system. The noise power N_M of the measurement system is measured by replacing the dip stick in Figure 6.17 with the 50 Ohm termination. The calculation of the noise temperature from the two noise levels N_C and N_H is done with the same formulae as for the UMS amplifiers. Same as for the UMS measurements, the measurement system is considered as one single measurement device with the noise level N_M. Furthermore, the settings for the spectrum analyzer are exactly the same as for the UMS measurement, meaning that the frequency range is 18 to 26 GHz and the bandwidth B = 1 MHz.

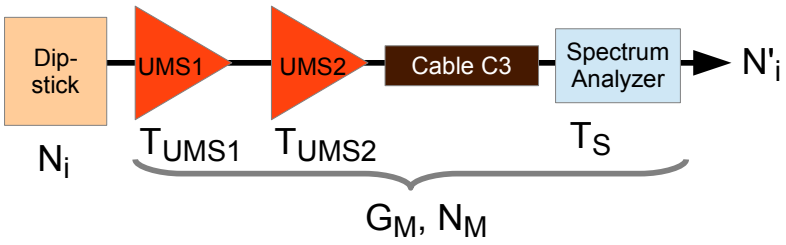

Figure 6.17.: *Schematic of the measurement system for the noise temperature measurements of the HEMT.*

The gain of the measurement system influences the shape of the noise power measured in the spectrum analyzer. The gain curve is therefore shown in Figure 6.18 even though the gain of the measurement system does not show up in the formula used to calculate the noise temperature. The peak slightly above 22 GHz and the drop between 18.5 and 19 GHz are features that also show up in the noise temperature curve of the HEMT amplifier. They are solely due to the measurement system and not a feature of the HEMT.

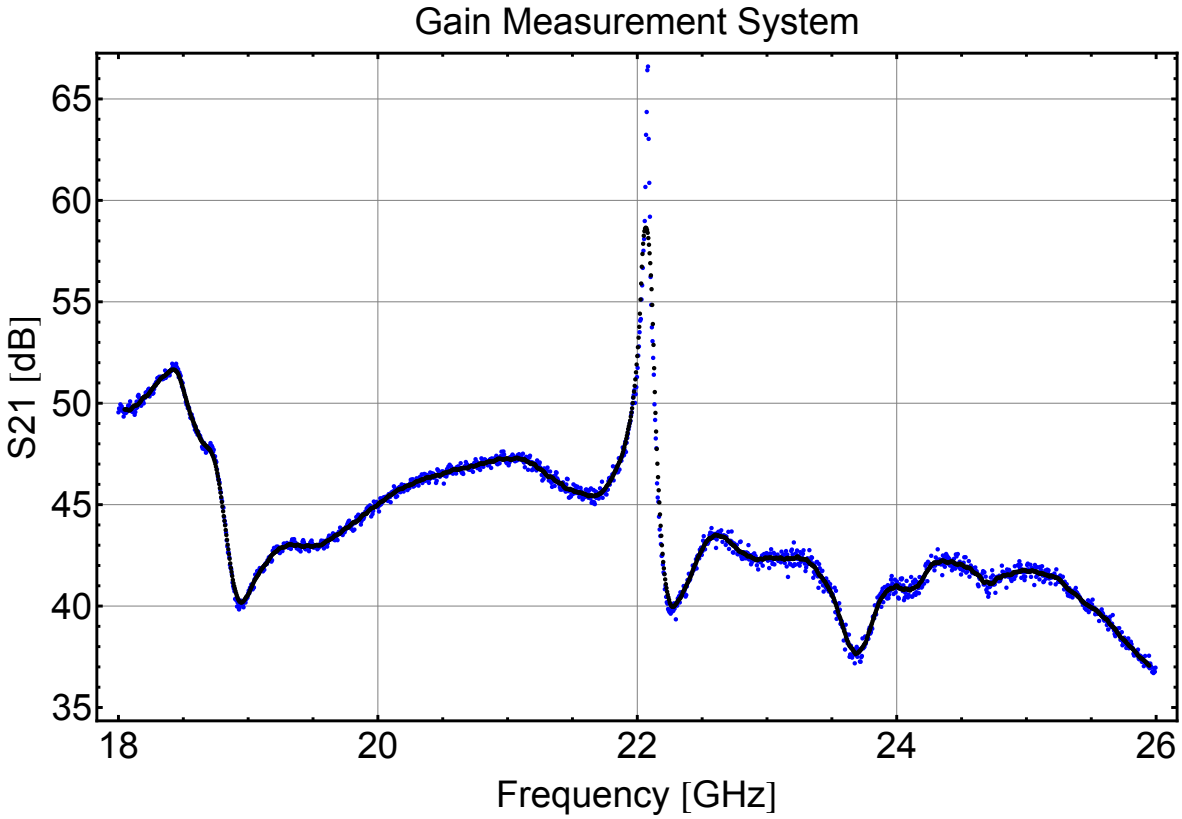

Figure 6.18.: *Gain G_M of the measurement system. The blue points are the values measured with the network analyzer. The black curve shows the moving average over 20 points.*

Noise power for different temperatures

The noise power N'_H is measured for different temperatures of the load during the cool down. In Figure 6.19 you can nicely observe how the noise level sinks for lower temperatures of the load.

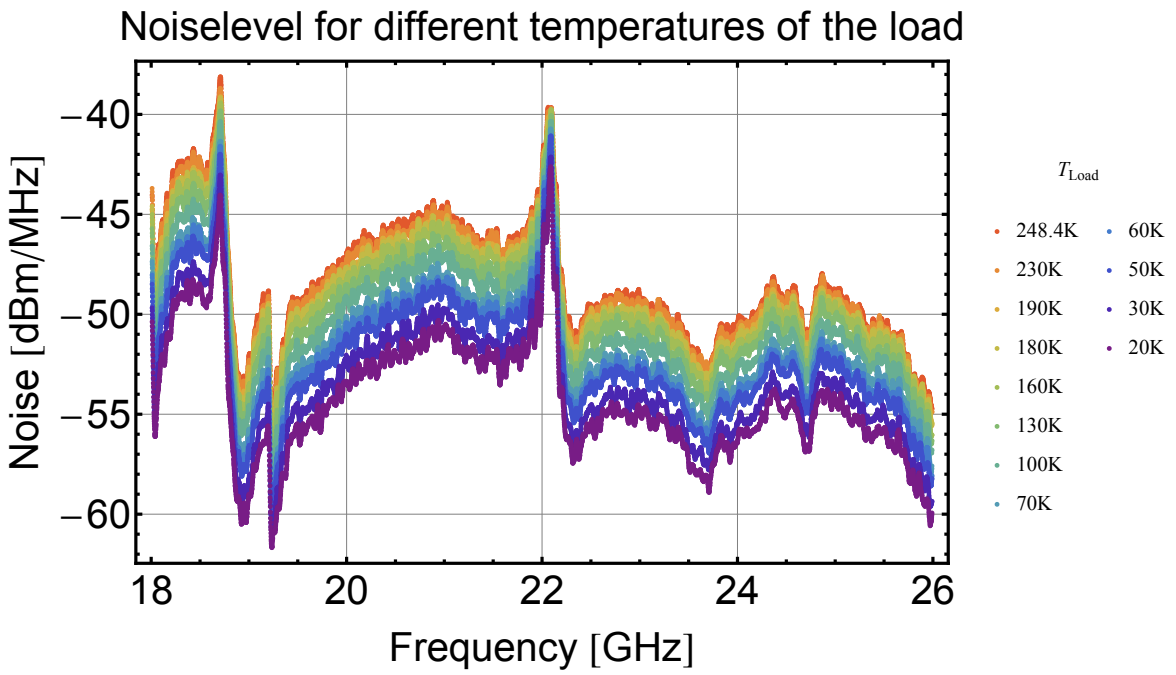

Figure 6.19.: *Noiselevel for different temperatures of the load measured with 1 MHz bandwidth.*

Effect of the cable

Same as for the UMS measurement, cable C1 between the load and the amplifier has to be treated specially. In contrast to cable C2, it is on different temperature levels for the cold and the hot measurement and its effect will thus not disappear when calculating the ratio Y. We will again use formula (6.9) to include the loss of the cable and additional noise. This time both for the cold and the hot load, the cable is not at the same temperature on both sides, as the HEMT is always at a lower temperature then the coldest one achieved with the load. We therefore choose to take the mean temperature between the HEMT and the load as the temperature of the cable:

$$T_W = \frac{T_{HEMT} + T_\Omega}{2}. \tag{6.14}$$

For the cold load the difference in temperature is small. For the hot load the difference can be up to 240 K and therefore the uncertainty of the cable temperature with the hot load is again set to ±30 K.

Results

The resulting noise temperatures for the HEMT 108 and the HEMT 116 obtained during the cool down can be seen in Figure 6.21. The HEMT 108 has a noise temperature between 20 K and 45 K, while the HEMT 116 has a noise temperature between 20 K and 65 K. The noise temperatures are higher than given in the specifications (plotted as a red bar in the figure). Also the noise temperatures we obtain from the different hot load temperatures T_H differ. Higher T_H generally lead to higher noise temperatures. It is also interesting that the noise temperature obtained from the measurement done with the heater (see Figure 6.20) is higher than the one obtained during the cooldown. Maybe this is due to the higher noise level in the dip stick at higher temperatures, which could also lead to additional noise in cable C2. This cable connects the HEMT and the output of the dip stick and passes by the load and the heater.

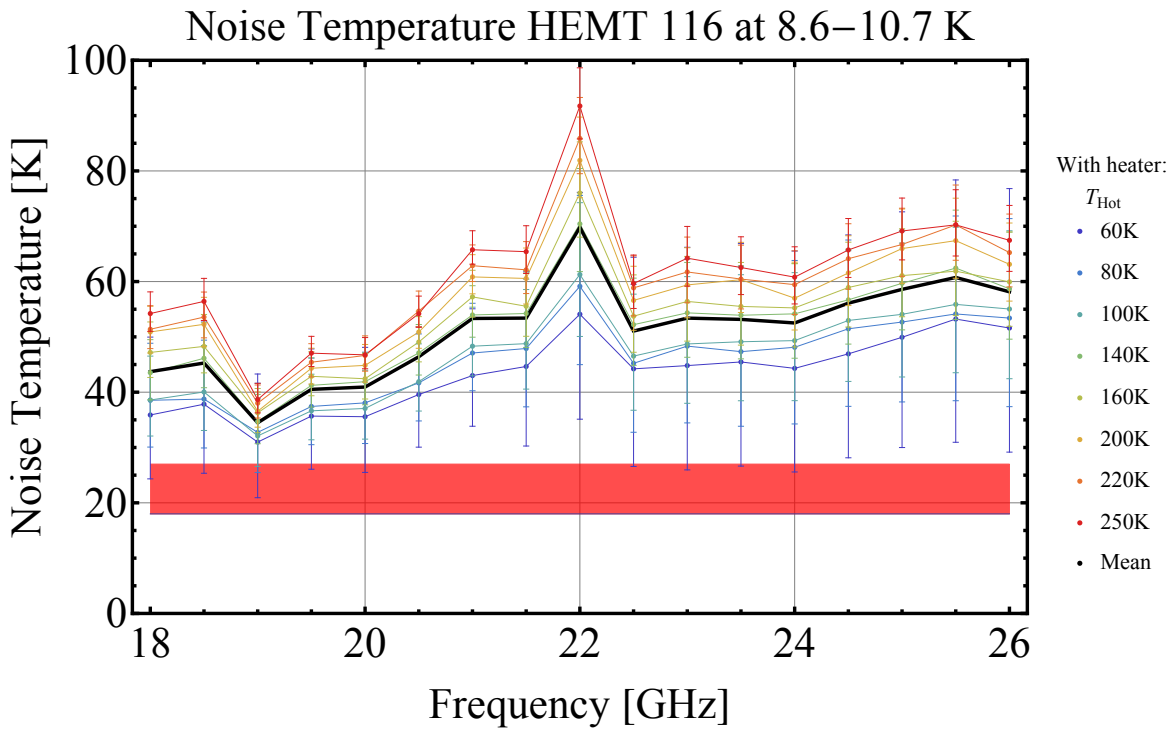

Figure 6.20.: *Noise temperature of the HEMT 116 amplifier obtained with the heater.*

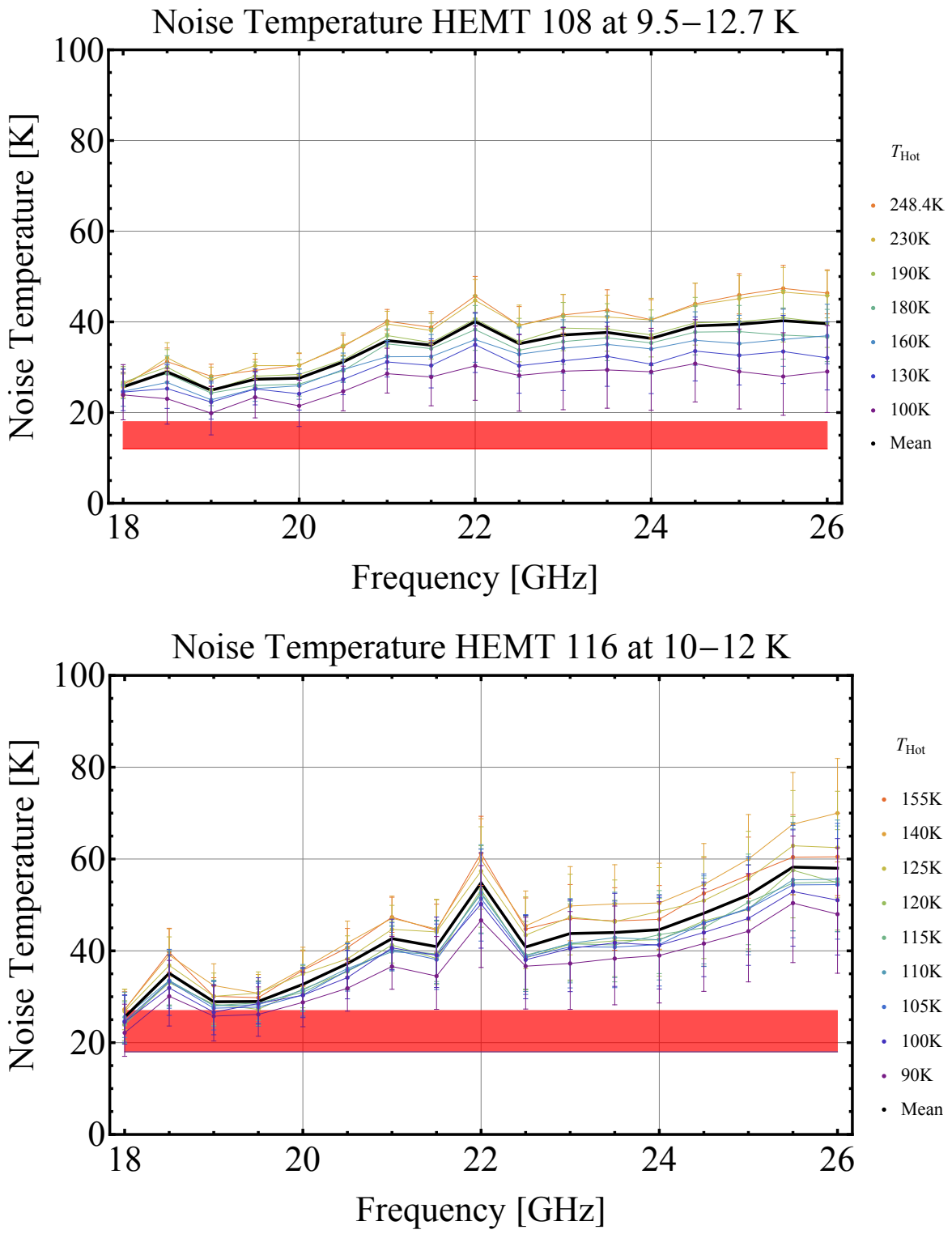

Figure 6.21.: *Noise temperature of the HEMT 108 and the HEMT 116 obtained during the cool down.*

6.4.4. Error sources

- The effect of cable C1 might not be estimated in the correct way by choosing a constant cable temperature T_W in formula (6.9). Also the chosen cable temperature might deviate from a more fitting value. This is taken into account by a conservative choice ($\pm$ 30 K) of error bars on T_W.

- The noise level of the measurement system might not be taken into account correctly as the load contributes to the noise level when the noise of the measurement system is determined. This means that the noise of the measurement system is smaller than the one measured and we subtract too much noise. For the UMS measurements, the noise power of the measurement system N_M we subtract from the measured signal N' amounts to less than 10% of N' (see section 6.4.1). For lower frequencies it is even less. This is due to low effective noise temperature of the measurement system thanks to the additional amplifier. In the ZFL measurement we did not have an extra amplifier in the measurement system and there the noise power of the measurement system N_M contributes with up to 25% of N'. For the HEMT measurements it is below 5% thanks to the two additional amplifiers.

- The load should be matched to allow for maximal noise transmission. We chose a 50 Ohm termination. The one used for the measurement with the HEMT was not specified down to the used temperature range. The impedance can be determined by measuring the S_{11} parameter and calculating the impedance Z_{11} with the formula

$$Z_{11} = \frac{S_{11} + 1}{S_{11} - 1} \cdot 50\Omega. \tag{6.15}$$

  We obtained a impedance differing by maximally 2% from 50 Ω. An experiment in which the termination was held into liquid nitrogen showed that the impedance at 77 K is the same as at room temperature. Since most thermal contraction takes place between 300 K and 77 K, we assume that the 50 Ohm termination is also reasonably well matched at even lower temperatures.

6.4.5. DC-block measurement

As the effect of the lossy cable between the load and the input of the HEMT is not fully understood, we decided to alter the experiment by replacing the cable with a DC-block of type INMET 8143A. The cable (C1) between the load and the HEMT can be left away, because the DC-block thermally isolates the HEMT from the load. The DC-block has less loss - with η between 0.89 and 0.91 at room temperatures - than cable C1, which has η between 0.55 and 0.7. We still use the same formula to include the effect of the lossy transmission (equation (6.9)), but the big advantage of the DC-Block is that the temperature of the load is not altered as much as with the cable. The error in the temperature estimation of the cable, respectively the DC-block, is less relevant when the loss in the element is low.

Layout

The DC-block measurement is carried out for the HEMT 108 inside the dip stick at liquid helium temperature without the heater. The load is directly connected to the DC-block, which is connected to the HEMT as can be seen in Figure 6.22 (a). The HEMT is thermalized with the copper bar like in the previous measurements (see Figure 6.22 (b)). The copper block containing the load is isolated from the copper bar by a layer of teflon and isolation tape. Since we want the load to slowly cool down to almost liquid helium temperature, the copper block has to be weakly thermalized with the copper bar. This is done with one strand of copper (see Figure 6.22 (c)).

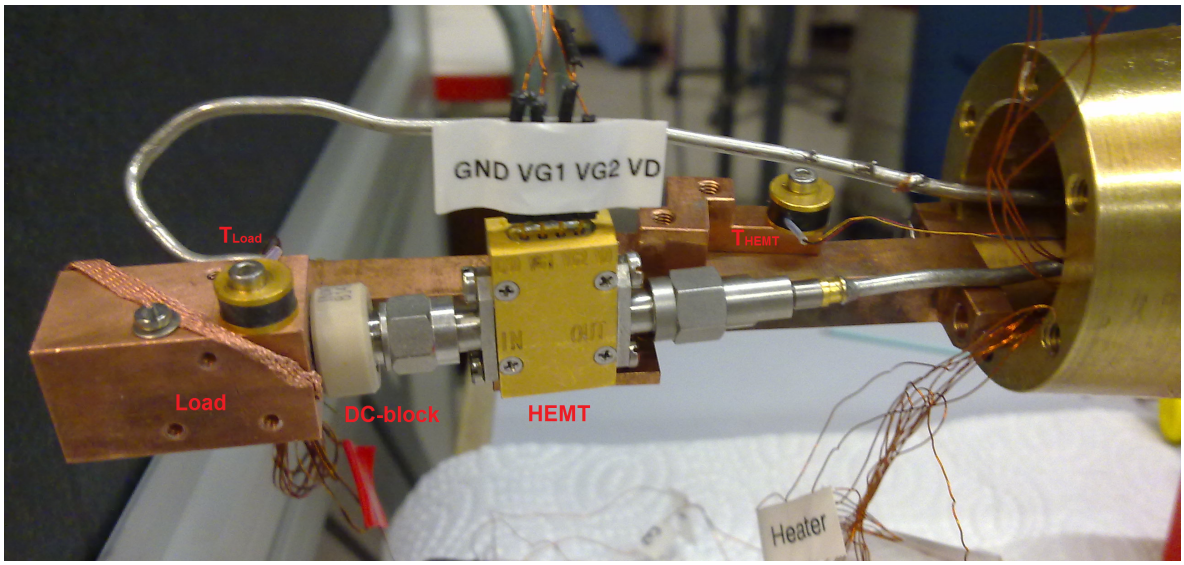

(a) *The layout of the DC-block measurement. The load in the copper block is directly connected to the DC-block which itself is directly connected to the HEMT. There is a temperature sensor (T_{Load}) on top of the load and one on the copper bar holding the HEMT (T_{HEMT}).*

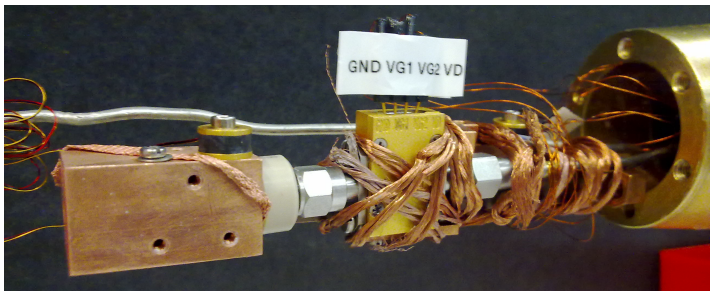

(b) *The HEMT and cable C2 are additionally thermalized with copper braids.*

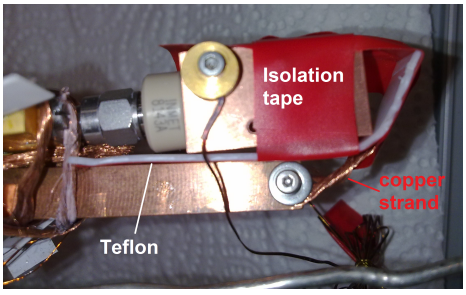

(c) *The copper block is isolated from the copper bar with a layer of teflon (white) and isolation tape (red). Heat can flow from the copper block via one strand of copper to the copper bar. It is fastened to the copper bar with a screw.*

Figure 6.22.: *Photographs of the DC-block measurement of the HEMT 108: layout and thermalization.*

Cool down rate

Same as in the other dip stick measurements, the opening is closed, the dip stick evacuated and placed inside the liquid helium dewar. The temperature of the load and the HEMT can be monitored with two temperature sensors. One is placed on top of the load (T_{Load}) and one on the copper bar holding the HEMT (T_{HEMT}). The noise power is measured at different temperatures of the load during the cool down and will be used as the noise power for the hot load T_H. The lowest temperature reached is 11 K and corresponds to T_C. This time we not only record the temperature corresponding to the data set, but also at what time the data is taken. This information is plotted in Figure 6.23 and labeled with "first cool down". The zero point in time corresponds to $T_{HEMT} = 26$ K. The HEMT (blue curve) cools down a lot faster than the load (red curve). In order to see how well the DC-block thermally isolates the HEMT from the load, we cut through the copper strand that thermalized the copper block of the load in the first run and carry out a second cool down. Again we record the temperature of the HEMT and the load at different times. This results in the light blue and orange cool down curve displayed in Figure 6.23. We can see that the load needs a lot longer to reach low temperatures than with the thermalization. We can thus conclude that most of the heat in the first cool down is conducted through the additional thermalization while the DC-block can maintain the temperature gradient.

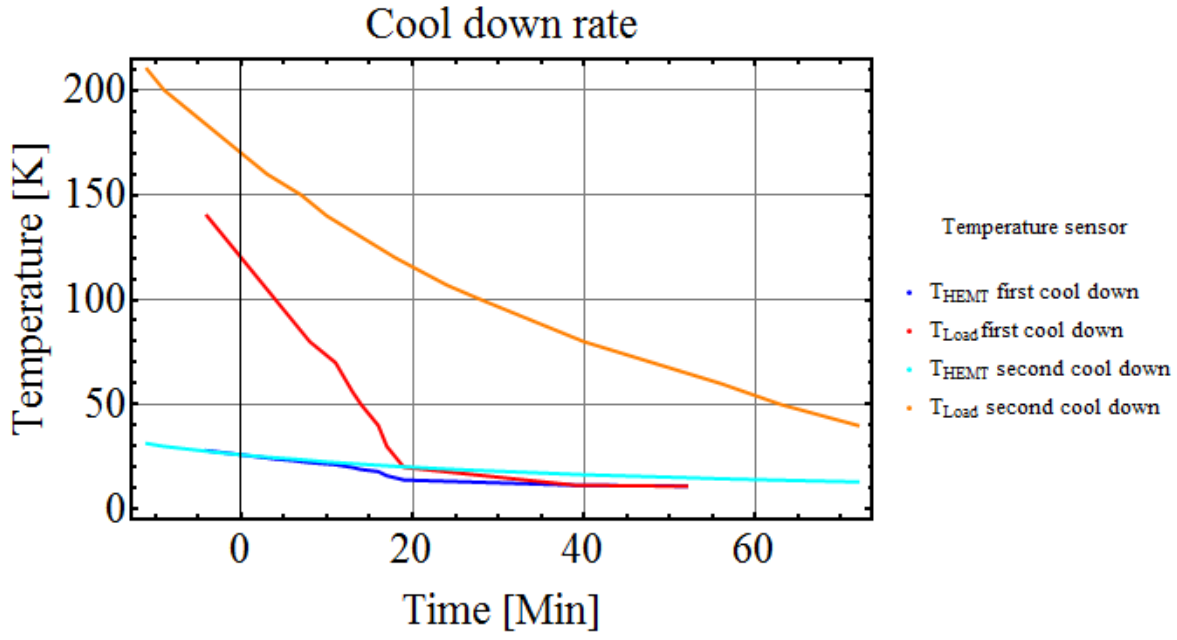

Figure 6.23.: *Comparison of the cool down rate for the 2 DC-Block measurements.*

Result

With the exception that η of cable C1 is replaced by η of the DC-block at room temperature, the analysis of the data is done in exactly the same way as for the cold measurements with

cable C1. The noise temperature for the HEMT 108 amplifier with the DC-block measurement method is shown in Figure 6.24. It is lower than in the previous measurements and lays in between 10 and 30 K, but still varies depending on which data set is used for the hot measurement.

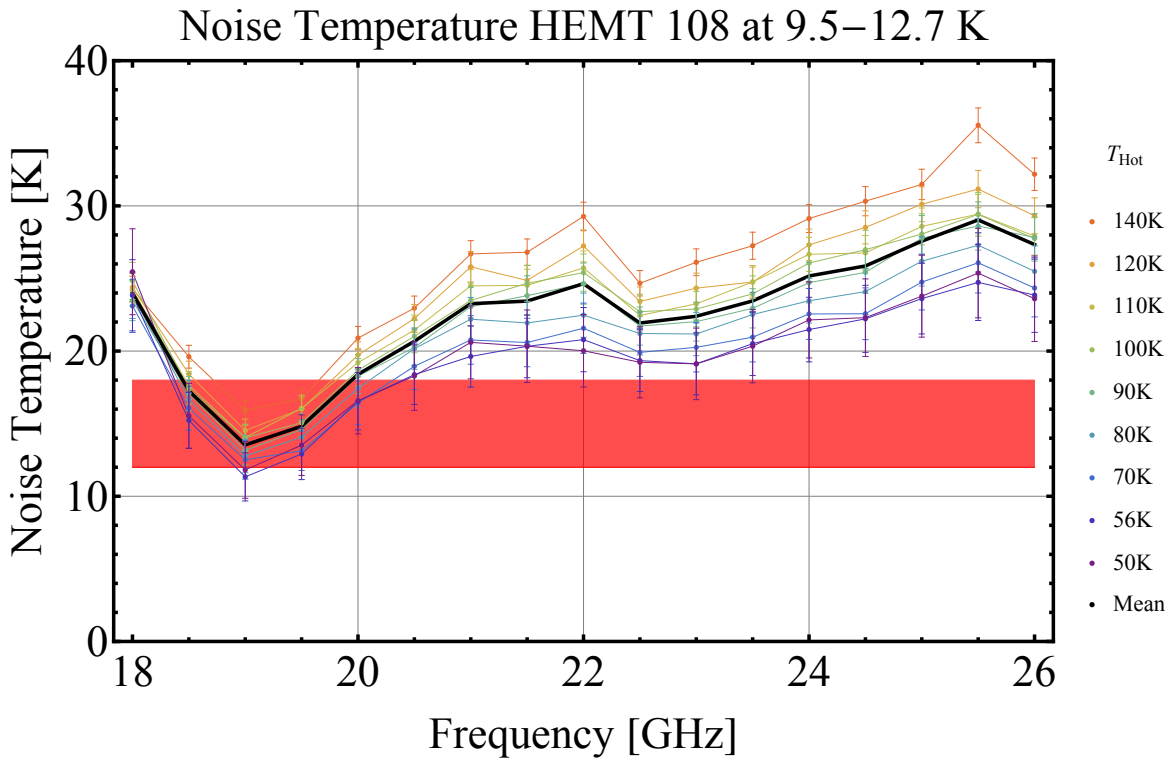

Figure 6.24.: *Noise temperature of the HEMT 108 amplifier obtained in the DC-block measurement.*

7. Conclusion and Outlook

Conclusion

This theses has two main experimental parts. In the first part, we observe the interaction between Rydberg atoms and the 3D microwave cavity. We develop a method to measure the AC and DC electric fields inside the cavity along the beam axis using Rydberg atoms. In the second part, we characterize the amplification system necessary for measuring a dispersive shift and determine the gain and noise temperature of the amplifiers.

The theoretical part of this theses starts with a brief motivation for hybrid quantum systems in the context of quantum computation and introduces some basic properties of Rydberg atoms and 3D microwave cavities. The two systems are then combined and the basic principles of cavity QED are reviewed. The theoretical part is concluded with a summary on noise in amplifiers.

The experimental part begins with a description of the experimental setup. The resonance spectrum of the cavity is determined and the alignment and pulse optimization procedure necessary for the main experiments is explained. We then measure the Rydberg spectrum and the velocity of the Rydberg atoms, which has a value between 1720 and 1790 m/s.

We show that we can drive Rabi oscillations with the cavity over the whole cavity length of 8 mm and develop a method with which we can find the minimal amplitude necessary to drive a π-pulse and the corresponding detuning from the field free transition frequency. This method is faster than measuring Rabi oscillations in two dimensions. From the measured π-pulse amplitudes we can obtain the modefunction along the beam axis. This means that we can characterize the AC electric field inside the cavity with Rydberg atoms. In the last measurement set we were able to reduce stray fields below 90 mV/cm corresponding to Stark shifts below 8 MHz.

We then demonstrate that it is possible to induce DC Stark shifts with the electrodes inside the cavity. We measure the quadratic dependance of the frequency shift on the applied voltage for different positions of the atoms inside the cavity. From that information we can find the electric field of the electrodes along the beam axis. The measured field profile corresponds well to the one obtained in simulations. From the measurements we can also get the strength of the stray fields present in the 3D cavity.

In a next step we design a new cavity that is suitable for measuring dispersive shifts. The design goal for the new cavity is that the electric field created by the electrodes is approximately constant over a 8 mm plateau along the beam axis and has a high transversal homogeneity.

Simulations show that shorter distances between the electrodes result in longer plateaus. We use this result to design two new cavities, cavity 5A and 5B. For cavity 5A with plate electrodes the electric field should drop by less then 5% over an 8 mm plateau and the inhomogeneity should be around 6%, which means that we can shift the atomic resonance frequency by 33 MHz with the Stark effect before the line width of the atomic resonance gets bigger than the line width of the critically coupled cavity.
In the next chapter we write about the characterization of the amplification system. After a description of the different components, the gain of the amplifiers is measured and the results are well in agreement with the specifications. For the down conversion board a support framework is built and the transmission is measured. Standing waves can be diminished by inserting attenuators with the trade-off of lower amplification. We verified the functioning of the DCB by measuring the resonance spectrum of the cavity.
A large experimental part involves the noise temperature measurements. We measure the warm amplifiers at room temperature and obtain noise temperatures of around 200 K. The cryogenic HEMT amplifiers are measured in a dip stick measurement inside liquid helium. The resulting noise temperatures are higher than specified, which is why an improved version of the experiment with a DC-block is made. This leads to a noise temperature between 10 and 35 K for the HEMT108 amplifier, which is only slightly higher then specified. We also discuss possible error sources.

Outlook

In this thesis we have investigated the AC und DC electric fields inside the cavity by observing the signal from the Rydberg atoms. The amplification system allows us to measure small microwave signals at the few photon level with low added noise, meaning that it should now also be possible to do the reverse: measure the state of the Rydberg atoms with the cavity. This is for example done in a dispersive shift measurement.
In order to realize such a measurement, the signal to noise ratio obtainable with the amplification system and the experimental parameters $\frac{g}{2\pi}$, $\frac{\kappa}{2\pi}$ and $\frac{\gamma}{2\pi}$ has to be calculated. For these calculations the characterization measurements done in this thesis are very helpful, as the noise temperature and the gain of the amplifiers are the main parameters needed to calculate the noise level at the end of the amplification procedure.
The necessary measurement time can be calculated using the signal to noise ratio [57], which also depends on the repetition rate of the experiment, the coupling factor and the quality factor. The repetition rate is 25 Hz. At the moment a new atom beam source is built with the aim to increase the repetition rate to 1 kHz.
The single atom coupling factor g_1 is easily calculated, but due to collective $\sqrt{N}$ enhancement of the coupling strength $g_N = g_1\sqrt{N}$, we rely on estimates for the number of Rydberg atoms N. The collective coupling strength could also be measured in an AC-Stark shift experiment, which is planned for the near future.
We also plan to enhance the quality factor of the cavity by coating the cavity with a supercon-

ducting material like lead. A higher quality factor will increase the contrast in future cavity QED measurements and will therefore also increase the SNR.
Another important ingredient for the dispersive shift measurements is cavity 5, which was designed to have a flat plateau in the electric field created by the electrodes and a low field inhomogeneity. One task will be to characterize cavities 5A and 5B as we have done for cavity 4B. In order to insert the newly designed cavities into the setup, electrode 4 has to be removed from the electrode stack inside the setup.
With these requirements fulfilled, a dispersive shift measurement should be possible in the near future.

The ultimate goal of the project is to be able to store quantum information processed with superconducting qubits in long-lived atomic Rydberg states. The interaction between the atoms and the superconducting qubits will be mediated by cavity photons at microwave frequencies. The implementation of superconducting Transmon type qubits into rectangular 3D cavities is very standard and is successfully done in our group on a regular basis. The challenge though will be to get superconducting Transmon qubits to work at frequencies of around 20 GHz, since the normal transition frequency is around 7 to 10 GHz. Once working, they can be placed at one of the free antinodes of the TE_{301} mode in our current 3D cavity (e.g. cavity 5B).
Another or the main challenge for this hybrid cavity QED system to be implemented is the required working temperature for superconducting qubits. The longterm goal is to build a new experimental setup based on a dilution refrigerator that achieves a base temperature of around 200 to 300 mK and provides access for the atomic Rydberg beam.

Acknowledgments

First of all I would like to thank Prof. Dr. Andreas Wallraff for providing the possibility to conduct my Master's thesis in his laboratory, the Quantum Device Lab at ETH Zürich. His suggestion to continue studying 3D microwave cavities as in my semester thesis, but in the context of the Rydberg Project, led to a very rewarding time for me in this research group.

I would like to express my greatest gratitude to my supervisor Mathias Stammeier, who gave me the opportunity to work with him on this fascinating and diverse project. He allowed me to participate in all aspects of his project and never hesitated to explain the details to me. I have learned a lot from him, not just on the theoretical, but also on the practical level. I would like to thank him for the great teamwork, the fruitful discussions and sharing his snacks with me.

My thanks also goes to Tobias Thiele, who built up the whole experimental setup and knows every detail about it. I am grateful for his initial introduction and inspiring me with his enthusiasm for Rydberg atoms. He was always glad to share his vast knowledge about the experiment and setup with me.

I would like to thank Prof. Dr. Frédéric Merkt from the Laboratory of Physical Chemistry at ETH Zürich and his group for their interest, critical questions and suggestions during the 'Rydberg-meetings'.

I really enjoyed the nice and welcoming atmosphere in this group. There was always somebody in the group around if I needed a helping hand or some advice. I was happy that many share my enthusiasm for volleyball - a pity that the sun was not shining more. It was a pleasure to work in such a motivated and talented group.

Last but not least, I would like to thank my family, my boyfriend Jonathan Jansson and all my friends - especially Florian Lüthi and Tim Holzherr - who accompanied me during my undergraduate studies in Zürich and in Stockholm. I am grateful for the continuous support and the great and successful time we had.

Bibliography

[1] Michael A. Nielsen and Isaac L. Chuang. *Quantum Computation and Quantum Information*. Cambridge University Press, 2000.

[2] T. H. Maiman. Stimulated optical radiation in ruby. *Nature*, 187(4736):493–494, Aug 1960.

[3] L. Essen and J. V. L. Parry. An atomic standard of frequency and time interval: A cæsium resonator. *Nature*, 176:280–282, Aug 1955.

[4] Moore. Cramming more components onto integrated circuits. *Electronics*, 38(8), April 1965.

[5] R. P. Feynman. Simulating physics with computers. *Int. J. Theor. Phys.*, 21(6):467–488, June 1982.

[6] D. Deutsch. Quantum theory, the Church-Turing principle and the universal quantum computer. *Proceedings of the Royal Society of London. Series A, Mathematical and Physical Sciences*, 400(1818):97–117, July 1985.

[7] David Deutsch and Richard Jozsa. Rapid solution of problems by quantum computation. *Proceedings: Mathematical and Physical Sciences*, 439(1907):553–558, December 1992.

[8] Lov K. Grover. A fast quantum mechanical algorithm for database search. In *Proceedings of the twenty-eighth annual ACM symposium on Theory of computing*, pages 212–219, Philadelphia, Pennsylvania, United States, 1996. ACM.

[9] P. W. Shor. Algorithms for quantum computation: Discrete logarithms and factoring. In *Proceedings, 35th Annual Symposium on Foundations of Computer Science, Santa Fe*, page 124. IEEE Computer Society Press, 1994.

[10] R. L. Rivest, A Shamir, and L Adleman. A method for obtaining digital signatures and public-key cryptosystems. *Commun. ACM*, 21(2):120–126, 1978.

[11] Artur K. Ekert. Quantum cryptography based on bell's theorem. *Phys. Rev. Lett.*, 67(6):661–663, Aug 1991.

[12] D. P. DiVincenzo. The physical implementation of quantum computation. *Fortschritte der Physik*, 48(9-11):771–783, 2000.

[13] Pieter Kok, W. J. Munro, Kae Nemoto, T. C. Ralph, Jonathan P. Dowling, and G. J. Milburn. Linear optical quantum computing with photonic qubits. *Rev. Mod. Phys.*, 79(1):135–174, Jan 2007.

[14] Rainer Blatt and David Wineland. Entangled states of trapped atomic ions. *Nature*, 453(7198):1008–1015, June 2008.

[15] M. Devoret and R J Schoelkopf. Superconducting circuits for quantum information: An outlook. *Science*, 339:1169–1174, 2013.

[16] Ronald Hanson and David D. Awschalom. Coherent manipulation of single spins in semiconductors. *Nature*, 453(7198):1043–1049, June 2008.

[17] N. Gershenfeld and I. Chuang. Bulk spin resonance quantum computation. *Science*, 275:350–356, 1997.

[18] Marcus W. Doherty, Neil B. Manson, Paul Delaney, Fedor Jelezko, Jörg Wrachtrup, and Lloyd C.L. Hollenberg. The nitrogen-vacancy colour centre in diamond. *Physics Reports*, 528(1):1–45, July 2013.

[19] Lieven M. K. Vandersypen, Matthias Steffen, Gregory Breyta, Costantino S. Yannoni, Mark H. Sherwood, and Isaac L. Chuang. Experimental realization of Shor's quantum factoring algorithm using nuclear magnetic resonance. *Nature*, 414:883, 2001.

[20] Stephan Gulde, Mark Riebe, Gavin P. T. Lancaster, Christoph Becher, Jürgen Eschner, Hartmut Häffner, Ferdinand Schmidt-Kaler, Isaac L. Chuang, and Rainer Blatt. Implementation of the deutsch-jozsa algorithm on an ion-trap quantum computer. *Nature*, 421(6918):48–50, January 2003.

[21] David Beckman, Amalavoyal N. Chari, Srikrishna Devabhaktuni, and John Preskill. Efficient networks for quantum factoring. *Phys. Rev. A*, 54:1034–1063, Aug 1996.

[22] Thomas Monz, Philipp Schindler, Julio T. Barreiro, Michael Chwalla, Daniel Nigg, William A. Coish, Maximilian Harlander, Wolfgang Hänsel, Markus Hennrich, and Rainer Blatt. 14-qubit entanglement: Creation and coherence. *Phys. Rev. Lett.*, 106:130506, Mar 2011.

[23] Anders S. Sørensen, Caspar H. van der Wal, Lilian I. Childress, and Mikhail D. Lukin. Capacitive coupling of atomic systems to mesoscopic conductors. *Phys. Rev. Lett.*, 92(6):063601, Feb 2004.

[24] P. Rabl, D. DeMille, J. M. Doyle, M. D. Lukin, R. J. Schoelkopf, and P. Zoller. Hybrid quantum processors: Molecular ensembles as quantum memory for solid state circuits. *Phys. Rev. Lett.*, 97(3):033003, July 2006.

[25] Serge Haroche and Jean-Michel Raimond. *Exploring the Quantum: Atoms, Cavities, and Photons*. Oxford University Press, New York, USA, 2006.

[26] Chad Rigetti, Jay M. Gambetta, Stefano Poletto, B. L. T. Plourde, Jerry M. Chow, A. D. Córcoles, John A. Smolin, Seth T. Merkel, J. R. Rozen, George A. Keefe, Mary B. Rothwell, Mark B. Ketchen, and M. Steffen. Superconducting qubit in a waveguide cavity with a coherence time approaching 0.1 ms. *Phys. Rev. B*, 86(10):100506, September 2012.

[27] S. D. Hogan, J. A. Agner, F. Merkt, T. Thiele, S. Filipp, and A. Wallraff. Driving Rydberg-Rydberg transitions from a coplanar microwave waveguide. *Phys. Rev. Lett.*, 108:063004, Feb 2012.

[28] T. Thiele, S. Filipp, J. A. Agner, H. Schmutz, J. Deiglmayr, M. Stammeier, P. Allmendinger, F. Merkt, and A. Wallraff. Manipulating rydberg atoms close to surfaces at cryogenic temperatures. *Phys. Rev. A*, 90:013414, 2014.

[29] Thomas F. Gallagher. *Rydberg Atoms*. Cambridge University Press, 1994.

[30] Hans A. Bethe and Edwin E. Salpeter. *Quantum mechanics of one- and two- electron atoms*. Plenum/Rosetta, 1977.

[31] G. W. F. Drake. High precision theory of atomic helium. *Phys. Scr.*, 83, 1999.

[32] Hermann Haken and Hans Christoph Wolf. *Atom- und Quantenphysik*. Springer, 8 edition, 2004.

[33] F. Merkt. Molecules in high rydberg states. *Annu. Rev. Phys. Chem.*, 48:675–709, 1997.

[34] S. D. Hogan and F. Merkt. Demonstration of three-dimensional electrostatic trapping of state-selected rydberg atoms. *Phys. Rev. Lett.*, 100(4):043001, 2008.

[35] Gordon Drake, editor. *Springer Handbook of Atomic, Molecular, and Optical Physics*. Springer, 2006.

[36] David M. Pozar. *Microwave engineering*. John Wiley & Sons, Inc., 4th ed. edition, 2011.

[37] M. Göppl, A. Fragner, M. Baur, R. Bianchetti, S. Filipp, J. M. Fink, P. J. Leek, G. Puebla, L. Steffen, and A. Wallraff. Coplanar waveguide resonators for circuit quantum electrodynamics. *J. Appl. Phys.*, 104(6):113904, Dec 2008.

[38] Silvia Ruffieux. Simulation and characterization of waveguides and the coupling to 3d microwave cavities. Master's thesis, ETHZ, 04 2014.

[39] E.T. Jaynes and F.W. Cummings. Comparison of quantum and semiclassical radiation theories with application to the beam maser. *Proceedings of the IEEE*, 51(1):89–109, 1963.

[40] A. Wallraff, D. I. Schuster, A. Blais, L. Frunzio, R.-S. Huang, J. Majer, S. Kumar, S. M. Girvin, and R. J. Schoelkopf. Strong coupling of a single photon to a superconducting qubit using circuit quantum electrodynamics. *Nature*, 431:162–167, 2004.

[41] A. Blais, R.-S. Huang, A. Wallraff, S. M. Girvin, and R. J. Schoelkopf. Cavity quantum electrodynamics for superconducting electrical circuits: An architecture for quantum computation. *Phys. Rev. A*, 69(6):062320–14, June 2004.

[42] Pierre Thoumany. *Optical Spectroscopy And Cavity QED Experiments With Rydberg Atoms*. PhD thesis, LMU, 2011.

[43] R. J. Thompson, G. Rempe, and H. J. Kimble. Observation of normal-mode splitting for an atom in an optical cavity. *Phys. Rev. Lett.*, 68(8):1132–1135, Feb 1992.

[44] J. M. Fink, M. Göppl, M. Baur, R. Bianchetti, P. J. Leek, A. Blais, and A. Wallraff. Climbing the Jaynes-Cummings ladder and observing its nonlinearity in a cavity QED system. *Nature*, 454(7202):315–318, July 2008.

[45] Rodney Loudon. *The Quantum Theory of Light*. Oxford U, 2000.

[46] F. Markert, P. Würtz, A. Koglbauer, T. Gericke, A. Vogler, and H. Ott. ac-stark shift and photoionization of rydberg atoms in an optical dipole trap. *New Journal of Physics*, 12(11):113003, November 2010.

[47] D. I. Schuster, A. Wallraff, A. Blais, L. Frunzio, R.-S. Huang, J. Majer, S. M. Girvin, and R. J. Schoelkopf. AC Stark shift and dephasing of a superconducting qubit strongly coupled to a cavity field. *Phys. Rev. Lett.*, 94(12):123602, April 2005.

[48] W. E. Lamb and R.C. Retherford. Fine structure of the hydrogen atom by a microwave method. *Phys. Rev.*, 72:241, 1947.

[49] M. Brune, P. Nussenzveig, F. Schmidt-Kaler, F. Bernardot, A. Maali, J. M. Raimond, and S. Haroche. From lamb shift to light shifts: Vacuum and subphoton cavity fields measured by atomic phase sensitive detection. *Phys. Rev. Lett.*, 72(21):3339–, May 1994.

[50] A. Fragner, M. Göppl, J. M. Fink, M. Baur, R. Bianchetti, P. J. Leek, A. Blais, and A. Wallraff. Resolving vacuum fluctuations in an electrical circuit by measuring the Lamb shift. *Science*, 322(5906):1357–1360, 2008.

[51] J. B. Johnson. Thermal agitation of electricity in conductors. *Phys. Rev.*, 32:97–109, Jul 1928.

[52] H. Nyquist. Thermal agitation of electric charge in conductors. *Phys. Rev.*, 32:110–113, Jul 1928.

[53] Herbert B. Callen and Theodore A. Welton. Irreversibility and generalized noise. *Phys. Rev.*, 83:34–40, Jul 1951.

[54] Ray Radebaugh. Development of the pulse tube refrigerator as an efficient and reliable cryocooler. *Proc. Institute of Refrigeration (London)*, 1999/2000.

[55] J. D. Carter and J. D. D. Martin. Energy shifts of rydberg atoms due to patch fields near metal surfaces. *Phys. Rev. A*, 83(3):032902–, March 2011.

[56] ed. J. M. Lafferty. *Foundations of vacuum science and technology.* John Wiley & Sons, New York, 1998.

[57] M. Stammeier. Bimonthly report: May/june 2013. Technical report, Quantum Device Lab, ETHZ, 2013.

[58] C. Lang, D. Bozyigit, Y. Salathe, C. Eichler, and A. Wallraff. Quantum signal analyzer for itinerant microwave radiation. *In Preparation*, 2013.

[59] Guy Kendall White and Philip J Meeson. *Experimental Techniques in Low-Temperature Physics; 4th ed.* Monographs on the Physics and Chemistry of Materials. Oxford Univ. Press, Oxford, 2002.

List of Figures

List of Tables

A. Units and conversions

A.1. Atomic units

Quantity	Atomic unit	Definition
Mass	Electron mass m_e	$9.109 \cdot 10^{-31}$ kg
Charge	Electron charge e	$1.602 \cdot 10^{-19}$ C
Action	Reduced Planck constant $\hbar$	$1.054 \cdot 10^{-34}$ Js
Length	Radius of the first Bohr orbit a_0	$0.529 \cdot 10^{-10}$ m
Energy	Twice the ionization potential of H: $E_h = \hbar^2/a_0^2 m_e$	$4.360 \cdot 10^{-18}$ J
Velocity	Velocity of the first Bohr orbit: $a_0 E_h/\hbar$	$2.188 \cdot 10^6$ $\frac{m}{s}$
Time	$\hbar/E_h$	$2.419 \cdot 10^{-17}$ s
Force	E_h/a_0	$8.239 \cdot 10^{-8}$ N
Electric potential	E_h/e	27.21 V
Electric field strength	$E_h/a_0 e$	$5.142 \cdot 10^{11}$ $\frac{V}{m}$

Table A.1.: *Atomic units [29, 30]*

A.2. Conversion: power and voltages

Power: decibel and dBm

Power ratios $P_R = \frac{P}{P_0}$ are generally given in decibel (dB):

$$P_R\,(\mathrm{dB}) = 10 \cdot \log_{10}(P_R)\,. \tag{A.1}$$

A 3dB increase corresponds approximately to doubling the power. The following formula gives the conversion back to a ratio:

$$P_R = 10^{P_R(\mathrm{dB})/10}. \tag{A.2}$$

A useful way to display small powers P is in dBm, which is the power ratio measured in decibels referenced to $P_0 = 1$ mW. Power P in mW can thus be converted to dBm with

$$\mathrm{P(dBm)} = 10 \log\left(\frac{\mathrm{P(mW)}}{1\ \mathrm{mW}}\right). \tag{A.3}$$

Network analyzer: S21

The network analyzer can either display the S21 parameter linearly or in decibel. When S21 is displayed linearly, S21 corresponds to the voltage ratio as defined in the book by Pozar [36].

When the parameter is however displayed in decibels, the displayed S21(dB) is defined as a power ratio, which would correspond to $|\mathrm{S21}|^2$ according to Pozar's definition. The displayed S21(dB) is thus given by

$$\mathrm{S21(dB)} = 20 \log |\mathrm{S21}| = 10 \log |\mathrm{S21}|^2 . \tag{A.4}$$

For cable loss and mode spectra measurements we use S21(dB) as displayed on the network analyzer. For the noise temperature measurements we are interested in the cable loss η, which is the S21 parameter given by the power ratio. We find

$$\eta = \mathrm{S21}^2 = 10^{\mathrm{S21(dB)}/10}. \tag{A.5}$$

HybridSweep: mV and dBm

In the LabView program HybridSweep we can conduct amplitude sweeps. The amplitudes are converted to powers and displayed as such on the microwave source. Normally the units mV and dBm are used. Voltages in mV are converted to powers in dBm with

$$\mathrm{P(dBm)} = 10 \log_{10} \left[1000 \cdot \left(\frac{\mathrm{V(mV)}}{1000} \right)^2 \right] \tag{A.6}$$

and powers in dBm to voltages in mV with

$$\mathrm{V(mV)} = 1000 \cdot \sqrt{\frac{10^{\mathrm{P(dBm)}/10}}{1000}}. \tag{A.7}$$

A.3. Conversion: noise figures and noise temperatures

Manufacturers usually specify the noise amplifiers exhibit with the noise figure F, whereas we generally use the noise temperature T_E. The noise temperature in K can be calculated from the noise figure F directly or in dB with [36]:

$$T_E\,(K) = 290 \cdot (F - 1) = 290 \cdot \left(10^{F(dB)/10} - 1 \right) \tag{A.8}$$

For the reverse direction, the formula

$$F = 1 + \frac{T_E\,(K)}{290\mathrm{K}} \tag{A.9}$$

can be used, where the noise figure can be converted to dB with equation (A.1).
The table below gives the conversions for values in the range relevant for our amplifiers.

Conversion between noise figure F in dB and noise temperature T_E in K

F(dB)	T_E [K]	F(dB)	T_E [K]	F(dB)	T_E [K]	F(dB)	T_E [K]
0.1	7	1.1	84	2.1	180	3.1	302
0.2	14	1.2	92	2.2	191	3.2	316
0.3	21	1.3	101	2.3	202	3.3	330
0.4	28	1.4	110	2.4	214	3.4	344
0.5	35	1.5	120	2.5	226	3.5	359
0.6	43	1.6	129	2.6	238	3.6	374
0.7	51	1.7	139	2.7	250	3.7	390
0.8	59	1.8	149	2.8	263	3.8	406
0.9	67	1.9	159	2.9	275	3.9	422
1	75	2	170	**3**	**289**	4	438

Table A.2.: *Conversion between noise figure F in dB and noise temperature T_E in K*

ETH

Eidgenössische Technische Hochschule Zürich
Swiss Federal Institute of Technology Zurich

Declaration of originality

The signed declaration of originality is a component of every semester paper, Bachelor's thesis, Master's thesis and any other degree paper undertaken during the course of studies, including the respective electronic versions.

Lecturers may also require a declaration of originality for other written papers compiled for their courses.

I hereby confirm that I am the sole author of the written work here enclosed and that I have compiled it in my own words. Parts excepted are corrections of form and content by the supervisor.

Title of work (in block letters):

Towards cavity QED experiments with Rydberg atoms coupled to a 3D microwave cavity

Authored by (in block letters):

For papers written by groups the names of all authors are required.

Name(s):	**First name(s):**
Ruffieux	Silvia

With my signature I confirm that

- I have committed none of the forms of plagiarism described in the 'Citation etiquette' information sheet.
- I have documented all methods, data and processes truthfully.
- I have not manipulated any data.
- I have mentioned all persons who were significant facilitators of the work.

I am aware that the work may be screened electronically for plagiarism.

Place, date	**Signature(s)**
Zürich, 1.10.2014	S. Ruffieux

For papers written by groups the names of all authors are required. Their signatures collectively guarantee the entire content of the written paper.